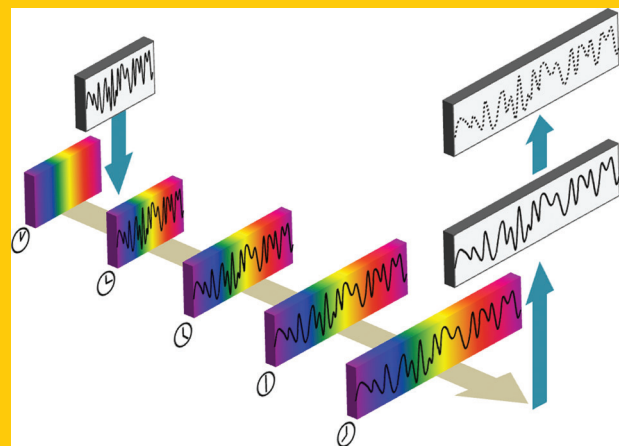


www.lpr-journal.org

LASER & PHOTONICS REVIEWS

Citation: A. M. Fard, S. Gupta, and B. Jalali,
Laser Photonics Rev. 7, No. 2, 207–263 (2013),
DOI 10.1002/lpor.201200015

Abstract Real-time wideband digitizers are the key building block in many systems including oscilloscopes, signal intelligence, electronic warfare, and medical diagnostics systems. Continually extending the bandwidth of digitizers has hence become a central challenge in electronics. Fortunately, it has been shown that photonic pre-processing of wideband signals can boost the performance of electronic digitizers. In this article, the underlying principle of the time-stretch analog-to-digital converter (TSADC) that addresses the demands on resolution, bandwidth, and spectral efficiency is reviewed. In the TSADC, amplified dispersive Fourier transform is used to slow down the analog signal in time and hence to compress its bandwidth. Simultaneous signal amplification during the time-stretch process compensates for parasitic losses leading to high signal-to-noise ratio. This powerful concept transforms the analog signal's time scale such that it matches the slower time scale of the digitizer. A summary of time-stretch technology's extension to high-throughput single-shot spectroscopy, a technique that led to the discovery of optical rogue waves, is also presented. Moreover, its application in high-throughput imaging, which has recently



led to identification of rogue cancer cells in blood with record sensitivity, is discussed.

Photonic time-stretch digitizer and its extension to real-time spectroscopy and imaging

Ali M. Fard^{1,*}, Shalabh Gupta², and Bahram Jalali^{3–6}

1. Introduction

Continued advances in complementary metal–oxide–semiconductor (CMOS) technology over the past few decades have created digital signal processors with astonishingly high and ever increasing data processing capability. In addition, massive amounts of digital data can conveniently be stored in non-volatile electronic, magnetic or optical memories whose storage density has been improving at a similarly rapid pace. Combined with advances in optical communication, these advantages have brought about the so-called “digital revolution” by enabling easy and economical storage, processing, and transmission of massive amounts of information. However, most physical-world signals are analog in nature and analog-to-digital converters (ADCs) are required to translate them to their digital representations. ADCs, therefore, are the crucial components for many electronic building blocks of the digital world. It is, hence, natural that there is un-diminishing demand for higher performance ADCs.

In particular, there are extremely important applications that demand ADCs with a very wide bandwidth and modest power dissipation. For instance, to satisfy the constantly growing demand for internet backbone networks and data centers, high-capacity optical networks employing advanced multi-level modulation formats (i.e., modulation formats with high spectral efficiency) are actively being pursued and are expected to be deployed [1–3]. Data demodulation and equalization at the receivers of such networks require ADCs with high bandwidth near the line data rate, which is currently between 10 Gbps to 100 Gbps. Such ADCs are also required for radar and signal intelligence (SIGINT) systems [4] as well as biomedical instruments [5].

1.1. Resolution of an analog-to-digital converter

An analog-to-digital converter (ADC) samples a continuous analog signal at regular intervals of time and quantizes it to the nearest digital values. Based on the architecture, the

¹ Wellman Center for Photomedicine, Harvard Medical School and Massachusetts General Hospital, Boston, MA 02114, USA

² Department of Electrical Engineering, Indian Institute of Technology Bombay, Mumbai 400076, India

³ Department of Electrical Engineering, University of California Los Angeles, CA 90095, USA

⁴ California NanoSystems Institute, University of California Los Angeles, CA 90095, USA

⁵ Department of Bioengineering, University of California Los Angeles, CA 90095, USA

⁶ Department of Surgery, David Geffen School of Medicine, University of California Los Angeles, CA 90095, USA

*Corresponding author(s): e-mail: mfard.ali@mgh.harvard.edu

electronic ADC can have several sample-and-hold (S&H) blocks and quantizers, extensive clock generation circuitry providing clocks' signals with different phases, duty cycles, and reference voltage buffers.

Approximating an analog quantity with a fixed number of discrete levels creates an inherent ambiguity known as quantization noise. For an ideal N -bit ADC, which quantizes the signal's full scale magnitude into 2^N discrete levels, the quantization places an upper limit to the signal-to-noise ratio (SNR). This limit is described by the following relation between SNR and the resolution, N ,

$$\text{SNR} = \frac{3}{2} \times 2^{2N} \equiv 6.02 \times N + 1.76 \text{ dB} \quad (1.1)$$

In addition to quantization noise, there are other noise sources in electronic ADCs including thermal and shot noises from electronic devices and noise introduced due to jitter in the sampling clock (called the aperture jitter noise). Also, several effects such as the nonlinear behavior of switches and amplifiers distort the signal and mismatches in transistor characteristics and non-uniform temperature distribution across the chip area further deteriorate the dynamic range. An important metric for the ADC resolution that includes both noise and distortion is the signal-to-noise-and-distortion-ratio (SNDR). The SNDR can also be used to calculate the effective-number-of-bits (ENOB) of the ADC, defined as the number of bits that an ideal ADC would have to produce the signal-to-quantization-noise-ratio [see (1.1)] equal to the SNDR in the given ADC.

$$\text{SNDR}_{dB} = 10 \times \log \left(\frac{\text{Signal}}{\text{Noise} + \text{Distortion}} \right) \quad (1.2)$$

$$\text{ENOB} = (\text{SNDR}_{dB} - 1.76)/6.02 \quad (1.3)$$

The ENOB in conjunction with the bandwidth over which it is measured are the most important performance metrics for an ADC. Most electronic ADCs available today are based on CMOS technology. While advances in CMOS technology due to device scaling have made a significant impact on improved speed, reduced power consumption and high complexity in digital circuits, the ADC performance has not kept pace. This is mostly because as the transistor channel length is reduced, so will its output impedance and hence its gain. This affects analog and mixed mode circuits (such as ADCs) more than digital logic circuits. Hence, device scaling does not directly improve the performance of CMOS analog-to-digital converters. Nevertheless, architectural improvements and availability of faster digital circuits and extensive amounts of digital post processing and calibration is resulting in improved ADC performance. In addition, certain fundamental issues associated with the use of electronics such as aperture (clock) jitter and comparator ambiguity (finite rise-fall time of comparators) [6] limit the speeds of high-resolution electronic ADCs. Therefore, it becomes imperative to explore other technologies such as

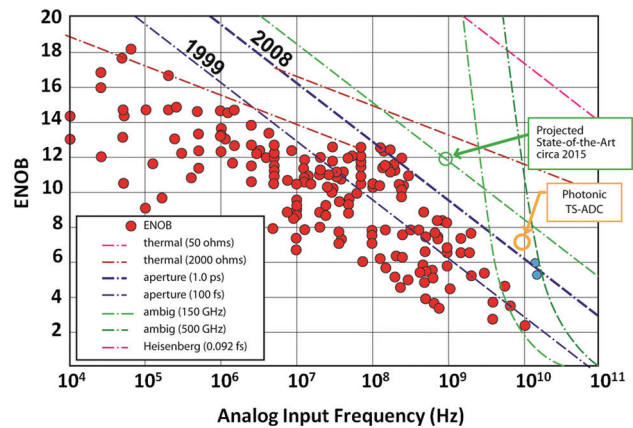


Figure 1 (online color at: www.lpr-journal.org) Resolution of state-of-the-art electronic ADCs versus input bandwidth. Blue data points include the 16-GHz Tektronix digitizer and Fujitsu's 15-GHz bandwidth ADC. The data point representing 7.2-ENOB time-stretch ADC (TSADC) over 10-GHz bandwidth [9] clearly shows that photonics can help in overcoming the current limitations of electronics.

photonics to enhance and boost performance of electronic ADCs.

A modified survey of state-of-the-art electronic ADCs created originally by Walden [7] is shown in Fig. 1. The figure depicts ENOB resolution versus input bandwidth for state-of-the-art electronic ADCs. Different traces in the figure show the limitations posed by electronics in achieving high resolution with large input bandwidths. Two new data points have been added to the figure to include Tektronix's 16-GHz digital oscilloscope and Fujitsu's 15-GHz ADC [8]. Another data point has been added to show the results obtained using the photonic time-stretch ADC (TSADC) that achieved 7.2-ENOB resolution over 10-GHz bandwidth [9], which is clearly beyond the capability of today's electronic ADCs. As discussed later in this article, a photonic time-stretch pre-processor improves the bandwidth of electronic ADCs and also offers a path to lower power consumption at very high speeds.

1.2. Photonic analog-to-digital converters

Many attributes of photonics can complement electronic ADCs to improve their performance. For example, mode-locked lasers achieve at least an order of magnitude smaller timing jitter values compared to electronic clocks, which is advantageous in sampling ultrafast signals with high precision [10, 11]. Wide optical bandwidths and low-loss optical dispersive media also provide large delay capabilities. Photonic systems are also more resilient to channel-to-channel crosstalk and electromagnetic interference. These advantages have led to the development of a vast number of techniques over the past few decades that use photonics to achieve analog-to-digital conversion of wideband electrical signals. A comprehensive discussion about most of these

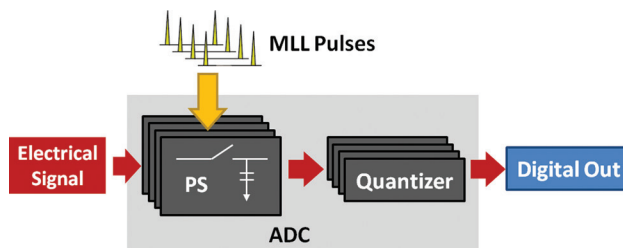


Figure 2 (online color at: www.lpr-journal.org) Time-interleaved ADC with optical clocking. The hybrid photonic ADC consists of an optically-clocked switch, which samples the electrical RF signal, and a quantizer that encodes each sample of the input signal into its binary representation. MLL: mode-locked laser; PS: photo-conductive switch.

techniques can be found in manuscripts by Valley [12] and Shoop [13]. A brief summary of prominent architectures that use the advantages of photonics to achieve wide bandwidth and improved resolution ADCs are presented in this article.

1.2.1. Optically-clocked ADCs

In optically-clocked ADCs, the electrical input signal is split into N -parallel channels each of which is sampled by a fast photo-conductive “Auston” switch triggered by an optical pulse stream generated by a mode-locked laser. For example, in Ref. [14], ultra-short mode-locked laser (MLL) pulses are applied to low temperature grown GaAs metal-semiconductor-metal switches to sample up to 40-GHz signals. Multiple time-interleaved samples are captured and distributed to a bank of electronic quantizers that digitize each sample. This is followed by digital reconstruction of the input signal by combining the samples obtained from different quantizers into a serial waveform, as shown in Fig. 2.

The motivation behind optically-sampled ADCs is that since MLL pulses typically have very low timing jitter, the aperture jitter noise [6] is reduced. Additionally, photo-conductive switching using laser pulses can provide picoseconds-scale time apertures that result in reduced distortion in the sampled signal. However, the electronic quantizer cannot acquire and digitize such fast pulses and therefore, a fast electronic sample and hold is necessary to capture the pulses and to produce a constant amplitude

voltage for duration long enough for the digitizer to process it. In practice, there are certain trade-offs in terms of ADC input capacitance, linearity, sampling rate, sampling noise, etc., that limit the resolution and bandwidth of these ADCs. Consequently, experimental demonstrations have mostly succeeded in capturing high carrier frequencies but with narrow instantaneous bandwidth. Using this approach, a two-channel 3.5-ENOB ADC sampling up to 40-GHz signals at 160-MS/s conversion rate has been demonstrated [14]. In another example, ~ 11.3 effective bits of resolution was achieved at 10 MHz of instantaneous bandwidth [11].

1.2.2. Wavelength division sampling

Another approach to optical sampling is to sample the fast input signal with a single sampler and then de-multiplex the high repetition rate sample stream into multiple slower rate parallel channels, each of which is digitized by a quantizer, as shown in Fig. 3. This optical carrier may consist of a train of ultra-short pulses or a train of dispersed broadband pulses. In the former case [15], the modulated pulses have to be de-multiplexed by an all-optical switch, which limits the number of channels. The finite extinction ratio of optical switches and their loss will set a limit on the achievable dynamic range, and hence the ENOB.

In wavelength division sampling (WDS), the signal is modulated over chirped broadband pulses [16–19] and de-multiplexed by optical wavelength filtering. By using a passive optical filter to de-multiplex the high repetition rate samples into lower rate streams, this technique eliminates the need for a fast all-optical switch. The extinction ratio of the filter will be a limiting factor on the dynamic range and also a fast sample and hold circuit is still required although the speed requirement is somewhat relaxed by the reduction in the optical bandwidth (due to wavelength filtering) and the chirp in sampling pulses, both of which lengthen pulse duration. Also, this technique requires broadband (i.e., supercontinuum) pulses. Fortunately, high power, stable, and broadband supercontinuum sources can easily be obtained nowadays with advancements in fiber-based mode-locked lasers and nonlinear fiber optics [20,21]. An alternative approach employing polarization-maintaining CFBG to create spectral slices and photonic sampling is also presented in ref. [19].

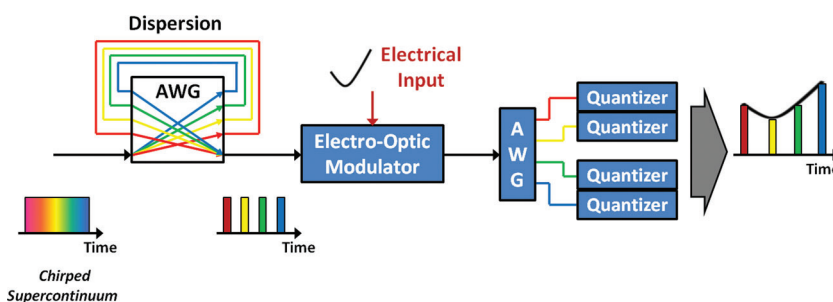


Figure 3 (online color at: www.lpr-journal.org) An optically-sampled time-interleaved ADC employing wavelength-division sampling [16]. AWG: Arrayed waveguide grating.

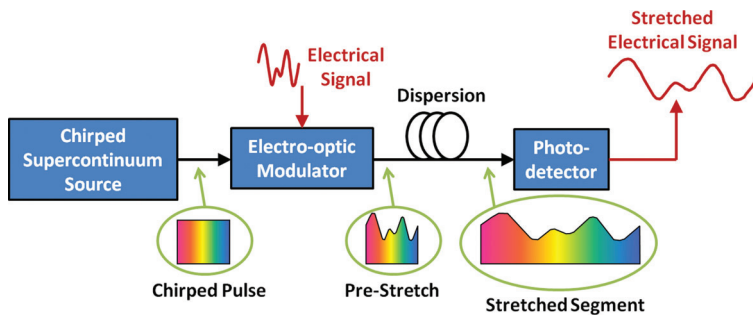


Figure 4 (online color at: www.lpr-journal.org) Schematic of the time stretch pre-processor, which is effectively an analog optical link. The electrical signal is modulated over a chirped optical pulse. Group velocity dispersion followed by photo-detection gives the stretched replica of the original signal [24, 25]. The dispersion penalty that can limit the electrical bandwidth is eliminated by employing either single sideband or phase diversity modulation, as discussed later in the article. The maximum bandwidth is therefore that of the electro-optic modulator.

1.2.3. Photonic time-stretch analog-to-digital converter

The time-stretch ADC consists of an analog front-end pre-processor and an electronic ADC back-end. In the photonic time-stretch analog-to-digital converter (TSADC) [22–25] [also called time-stretch enhanced recorder (TiSER)], the bandwidth of the electrical signal is compressed prior to digitization by stretching the waveform in time using a front-end optical pre-processor, as shown in Fig. 4. Bandwidth compression occurs because of time stretching and is different than down conversion. In the former, both the carrier frequency and the bandwidth are reduced, while in the latter, only the carrier is reduced and the bandwidth remains unchanged. To accomplish the time stretch, the electrical signal is modulated over a linearly chirped optical pulse that is obtained by dispersing a femtosecond mode-locked laser output. Propagation through dispersive fiber stretches the modulated pulses in time. The photo-detector converts these optical signals back to the electrical domain and the resultant electrical signal is the stretched replica of the original signal with much reduced analog bandwidth. This signal can now be recorded by a slow real-time electronic digitizer that would have been too slow to capture the original signal. Time-stretch factors of up to 250 have been achieved, and electrical signals with frequencies up to 108 GHz have been digitized in real-time at intervals down to 100-fsec using the TSADC [26, 27].

To achieve continuous operation, the signal is divided into multiple segments by the front-end optical pre-processor, in addition to time stretching. These time-stretched segments are digitized and then combined to obtain the continuous-time signal in the digital domain. The time-stretch technique effectively extends the bandwidth of back-end electronics digitizers and hence TSADC is one of the most practical approaches to wideband ADCs. In this article, we discuss the fundamental concepts of time-stretch ADC technology and show how it can lead to practical ultra-wideband ADCs, and high-end test and measurement equipment.

This manuscript presents the fundamentals of the TSADC and summarizes its important results addressing the demand for *resolution, dynamic range, bandwidth, and power dissipation*. The use of TSADC for applications in which an optical signal is to be captured is described. Finally, spin-off applications of photonic time-stretch to ul-

trafast imaging and spectroscopy inside and outside the telecommunications band are presented.

2. Fundamentals of photonic time-stretch analog-to-digital converter

The photonic time-stretch analog-to-digital converter (TSADC) [22–25, 28] extends the bandwidth of electronic ADCs. The TSADC is also known as the photonic time stretch (PTS) digitizer [29]. As discussed earlier, this approach employs group-velocity dispersion (GVD) to slow down the analog signal in time (or compress its bandwidth) before digitization by an electronic ADC. This section describes the fundamental considerations and practical issues involved in achieving ultra-wideband high-resolution analog-to-digital conversion using the photonic time-stretch technique.

2.1. Operation principle of the time-stretch ADC

The basic operating principle of the TSADC is shown in Fig. 5. The front-end pre-processor stretches the signal in time and splits it into multiple segments using a coarse wavelength division demultiplexing (WDM) filter. Filtering ensures that the stretched signal segments do not overlap and interfere with each other after time-stretching. The time-stretched signal segments are then converted to digital samples by slow electronic ADCs. Finally, these samples are collected by a digital signal processor (DSP) and rearranged in order to achieve the output signal as the digital representation of the original analog signal. Any distortion added to the signal by the time-stretch pre-processor is also removed by the DSP.

Photonics is an ideal platform for performing the time-stretch because the process requires a broadband chirped carrier wave as well as a low-loss wideband dispersive medium to transform the fast time scale of the input signal to a slower time-scale output signal. The time stretch pre-processor is a modified analog optical link. It consists of an optical source, an electro-optic modulator making up the transmitter, a fiber link, and a receiver consisting of a photo-detector and electronics. The optical source

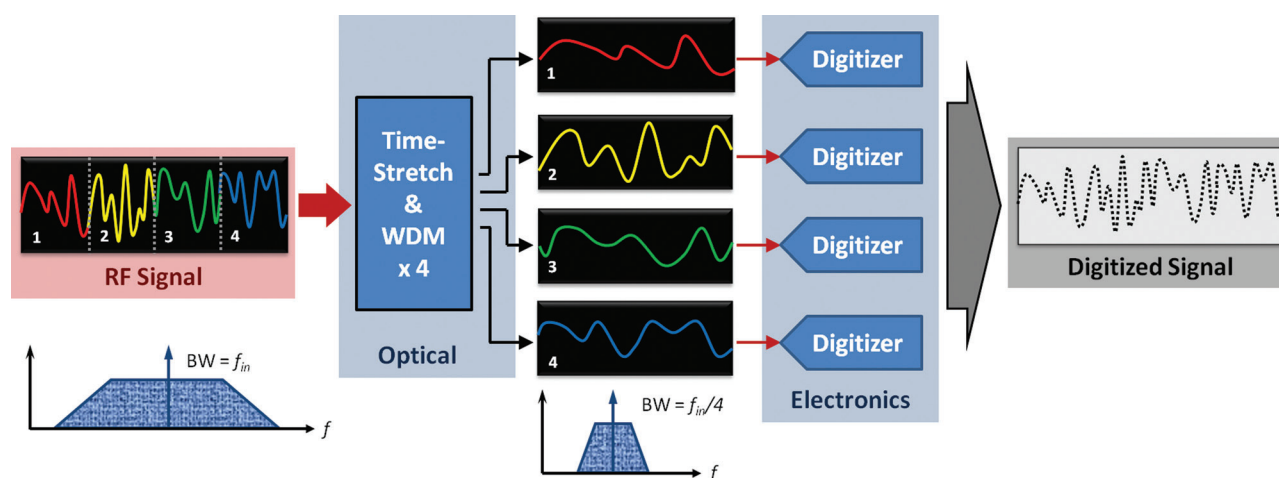


Figure 5 (online color at: www.lpr-journal.org) Conceptual diagram of the photonic time stretch ADC. The electrical signal is stretched and segmented by an optical front-end. Stretched segments are digitized by slow back-end digitizers and combined to obtain the digital copy of the original signal [24, 25]. Unlike a traditional time-interleaved ADC array, the analog signal that each ADC sees is below its Nyquist bandwidth. Because the signal at the input of each digitizer is slowed down to below the digitizer's Nyquist bandwidth (half of the sampling rate) each digitizer captures the full input signal within each segment. This is in contrast to the situation in a conventional sample-interleaved ADC array in which the signal at the digitizer input is above its Nyquist rate. The system functions as a continuous-time ADC, or alternatively as a short-time Fourier transformer, where the time window is the length of individual segments.

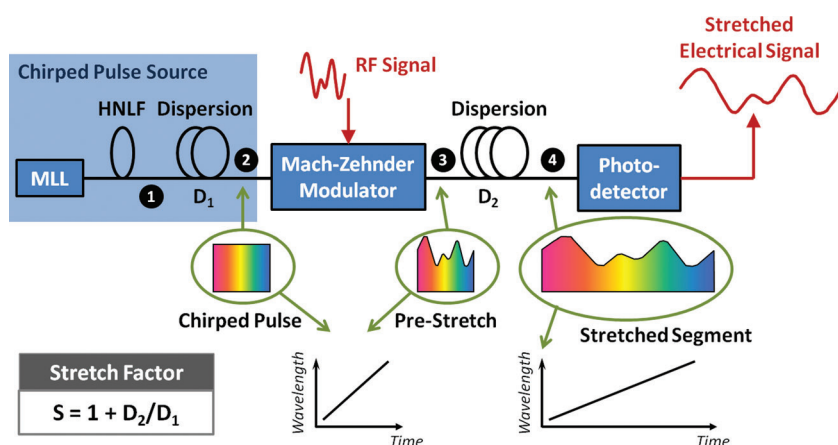


Figure 6 (online color at: www.lpr-journal.org) Physics of the photonic time-stretch pre-processor. The system is effectively a dispersive analog optical link in which the continuous-wave laser source is replaced by a chirped pulse source. MLL: Mode-locked laser; HNLF: Highly non-linear fiber; PD: Photo-detector.

is typically a mode-locked laser (MLL) producing ultra-short optical (supercontinuum) pulses (typically 100 to 200 femtoseconds long) [30] followed by a group velocity dispersive (GVD) element such as dispersion compensating fibers (DCF) or chirped fiber Bragg grating (CFBG), or a recently-developed chromo modal dispersion device (CMD) [31].

A supercontinuum pulse is typically generated using a highly non-linear fiber (HNLF) to broaden the spectrum of a high peak power narrow linewidth pulse through nonlinear interactions such as self-phase modulation, modulation instability and Raman frequency conversion, as shown in Fig. 6. The pulse is then chirped upon propagation through a dispersive medium, e.g. in a fiber with length L_1 and GVD value of D_1 . This process results in time-to-wavelength mapping in the stretched pulse since different wavelength components travel at different velocity due to GVD. The frequency of the chirped pulse varies continuously with

time over a time window that represents the capture window of a single shot. The analog input signal is modulated onto the chirped pulse using an electro-optic intensity modulator (e.g., Mach-Zehnder modulator). This process maps the time scale of the input signal into the optical frequency. The modulated chirped pulse, and hence the analog input signal that it carries, is then stretched in a second dispersive medium with length L_2 and GVD value of D_2 . Finally, the modulated optical pulses are converted to the electrical domain by a photo-detector, providing the stretched replica of the original analog signal. The time stretch factor is given by,

$$S = \frac{\text{Temporal pulse width (after time - stretching)}}{\text{Temporal pulse width (after pre - chirping)}} = \frac{D_1 + D_2}{D_1} = 1 + \frac{D_2}{D_1} = 1 + \frac{L_2}{L_1}. \quad (2.1)$$

For continuous operation, a train of supercontinuum pulses is used to stretch the signal, which is then divided into multiple (wavelength channel) segments using optical filters similar to those used in coarse wavelength division multiplexing.

2.2. Mathematical framework

While the simple qualitative description based on wavelength-to-time mapping is helpful, a detailed mathematical analysis is required to fully understand the working principle of the photonic time stretch. Being a modified communication link, understanding and quantifying its performance requires understanding the nature of the carrier wave and modulation sidebands and what happens to them as they propagate through the system. The mathematical analysis explaining this process and its performance is presented in this section. The symbols used in the mathematical model are defined in Table 1.

The time domain electric fields at different positions in the time-stretch system are denoted by E with the subscripts 1–4 for fields at the different locations shown in Fig. 6. Fourier transforms of these fields are denoted by \tilde{E} to represent them in the frequency domain. Initially, a chirped carrier pulse is created by dispersing supercontinuum pulses (represented by E_1) in the first group velocity dispersion stage to obtain E_2 . In frequency domain, the GVD induces a frequency dependent phase shift onto the carrier wave \tilde{E}_2 .

$$\tilde{E}_1(\omega) = \int_{-\infty}^{+\infty} E_1(t)e^{-j\omega t} dt \quad (2.2)$$

$$\tilde{E}_2(\omega) = \tilde{E}_1(\omega)e^{-j\omega^2\beta_2L_1/2} \cdot e^{-j\omega^3\beta_3L_1/6} \quad (2.3)$$

Here both the linear GVD (β_2) and its dispersion slope (β_3) are included. To simplify the mathematics, in the remainder of this section the β_3 term is ignored. Non-quadratic phase shifts caused by β_3 of GVD elements and elsewhere in the signal path cause time warping in the stretched signal. Time warps and the means to eliminate them are described later in this manuscript.

The chirped carrier field is modulated by the electrical signal in the Mach-Zehnder modulator biased at its quadrature point. It is important to note that, unlike in a time lens [32], the input signal is not dispersed prior to modulation onto the carrier. The lack of low-loss wideband electrical dispersive elements prevents the use of time lens technology for slowing electrical waveforms. We assume a single-tone electrical signal that varies with time as $\cos(\omega_{RF}t)$ and represent the modulation index with m to obtain,

$$E_3(t) = \frac{E_2(t)}{2} \left[e^{j(m/2)\cos(\omega_{RF}t)} + e^{-j(m/2)\cos(\omega_{RF}t)+j\pi/2} \right] \quad (2.4)$$

The above expression is for a push-pull Mach-Zehnder modulator (MZM). However, a similar analysis can also

Table 1 Symbols used in time-stretch ADC mathematical framework.

Parameter	Definition	Dimensions
E, \tilde{E}	Electric fields in time and frequency domains, respectively	V/m
m	Modulation index ($\pi V_{\text{amp}}/V_{\pi}$)	-
ω_{RF}	Angular frequency of the original electrical signal	rad/s
β_2, β_3	Second and third order dispersion parameters, respectively	$\text{s}^2/\text{m}, \text{s}^3/\text{m}$
η	Photo-detector responsivity	A/W
α	Attenuation coefficient	1/m
γ	Nonlinear coefficient	$\text{W}^{-1}\text{km}^{-1}$
n	Refractive index of the fiber	-
ϵ_0	Relative permittivity of free space	F/m
A_{eff}	Effective optical field mode area in fiber	m^2
P_{in}	Average optical power at photo-detector input	W
V_{amp}	Signal amplitude	V
V_{π}	Half wave voltage of the Mach-Zehnder modulator	V
B_e	Electrical bandwidth after stretching	Hz
R	Electrical impedance at source or load (50- Ω)	ohm
NF_e	Electrical noise figure (referred to 50- Ω impedance)	dB
F	Optical noise factor (noise figure in linear scale)	-
n_{sp}	Optical amplifier population inversion factor	-
C	Sampling capacitance	F
i_{signal}	Rms (root-mean-squared) signal current	A
i_n, v_n	Rms noise current and noise voltage, respectively	A, V
q	Electron charge	c
T	Ambient temperature	$^{\circ}\text{K}$
k	Boltzmann constant	J/K
h	Planck constant	J.s
ν	Optical frequency	Hz
RIN	Relative intensity noise of the laser	dB/Hz
P_{NEP}	Photo-detector input noise equivalent power per \sqrt{Hz}	$\text{W}/\sqrt{\text{Hz}}$

be performed when a single-electrode MZM (with non-zero chirp) is used. For simplicity, we assume a linear approximation, where the second and higher order terms in $(m/2)\cos(\omega_{RF}t)$ in the Taylor series expansion of the exponentials are ignored. Second- and third-order distortions

and the means to mitigate them are discussed later in this manuscript (Section 4). The linear approximation leads to a double sideband-modulated chirped carrier,

$$\begin{aligned} E_3(t) &\approx \frac{E_2(t)}{\sqrt{2}} e^{j\pi/4} \left[1 + \frac{m}{2} \cos(\omega_{\text{RF}} t) \right] \\ &= \frac{E_2(t)}{\sqrt{2}} e^{j\pi/4} \left[1 + \frac{m}{4} (e^{j\omega_{\text{RF}} t} + e^{-j\omega_{\text{RF}} t}) \right], \end{aligned} \quad (2.5)$$

and the frequency-domain representation of this double sideband-modulated field is given by,

$$\begin{aligned} \tilde{E}_3(\omega) &= \frac{e^{j\pi/4}}{\sqrt{2}} \left[\tilde{E}_2(\omega) \right. \\ &\quad \left. + \frac{m}{4} (\tilde{E}_2(\omega - \omega_{\text{RF}}) + \tilde{E}_2(\omega + \omega_{\text{RF}})) \right], \end{aligned} \quad (2.6)$$

Once this field propagates through the second GVD element, the electric field is,

$$\begin{aligned} \tilde{E}_4(\omega) &= \tilde{E}_3(\omega) e^{-j\omega^2 \beta_2 L_2 / 2} \\ &= \frac{e^{j\pi/4}}{\sqrt{2}} e^{-j\omega^2 \beta_2 L_2 / 2} \times \left(\tilde{E}_1(\omega) e^{-j\omega^2 \beta_2 L_1 / 2} \right. \\ &\quad \left. + \frac{m}{4} \tilde{E}_1(\omega - \omega_{\text{RF}}) e^{-j(\omega - \omega_{\text{RF}})^2 \beta_2 L_1 / 2} \right. \\ &\quad \left. + \frac{m}{4} \tilde{E}_1(\omega + \omega_{\text{RF}}) e^{-j(\omega + \omega_{\text{RF}})^2 \beta_2 L_1 / 2} \right). \end{aligned} \quad (2.7)$$

For wideband supercontinuum pulses (i.e., $\Delta\omega_{\text{optical}} \gg \Delta\omega_{\text{RF}}$) that have slow frequency dependent variations, $\tilde{E}_1(\omega \pm \omega_{\text{RF}}) \approx \tilde{E}_1(\omega) \approx \tilde{E}_1(\omega \pm \frac{\omega_{\text{RF}}}{S})$. Also, when the dispersion-induced phase is defined as $\phi_{\text{DIP}} = \omega_{\text{RF}}^2 \beta_2 L_2 / 2S$, where $S = 1 + D_2/D_1$, and the envelope function is defined as $\tilde{E}_{\text{env}}(\omega) = \frac{e^{j\pi/4}}{\sqrt{2}} \tilde{E}_1(\omega) e^{-j\omega^2 \beta_2 (L_1 + L_2) / 2}$, (2.7) can be rewritten as,

$$\begin{aligned} \tilde{E}_4(\omega) &= \tilde{E}_{\text{env}}(\omega) + \frac{m}{4} e^{-j\phi_{\text{DIP}}} \\ &\quad \times \left[\tilde{E}_{\text{env}}\left(\omega - \frac{\omega_{\text{RF}}}{S}\right) \right. \\ &\quad \left. + \tilde{E}_{\text{env}}\left(\omega + \frac{\omega_{\text{RF}}}{S}\right) \right], \end{aligned} \quad (2.8)$$

$$\begin{aligned} E_4(t) &= E_{\text{env}}(t) \left[1 + \frac{m}{4} e^{-j\phi_{\text{DIP}}} \right. \\ &\quad \left. \times (e^{j\omega_{\text{RF}} t / S} + e^{-j\omega_{\text{RF}} t / S}) \right]. \end{aligned} \quad (2.9)$$

The photocurrent in the absence of the electrical signal can be written as

$$I_{\text{env}}(t) = \frac{c\epsilon_0 n}{2} \eta A_{\text{eff}} E_{\text{env}}(t) E_{\text{env}}^*(t). \quad (2.10)$$

Therefore, the output current with RF modulation is

$$\begin{aligned} I_{\text{out}}(t) &= \frac{c\epsilon_0 n}{2} \eta A_{\text{eff}} E_4(t) E_4^*(t) \approx I_{\text{env}}(t) \\ &\quad \times \left[1 + m \cos\left(\frac{\omega_{\text{RF}} t}{S}\right) \cos(\phi_{\text{DIP}}) \right. \\ &\quad \left. + \frac{m^2}{4} \cos^2\left(\frac{\omega_{\text{RF}} t}{S}\right) \right]. \end{aligned} \quad (2.11)$$

For small values of m (i.e. $m \ll 1$), the m^2 component can be ignored, and the envelope modulation can be removed using the following operation:

$$\begin{aligned} I_{\text{signal}}(t) &= \frac{I_{\text{out}}(t) - I_{\text{env}}(t)}{I_{\text{env}}(t)} \\ &= m \cos\left(\frac{\omega_{\text{RF}} t}{S}\right) \cos(\phi_{\text{DIP}}) \end{aligned} \quad (2.12)$$

This output signal has a frequency ω_{RF}/S for the input signal frequency ω_{RF} , which implies that the frequency (and the bandwidth) are compressed or the signal is stretched in time by factor S . From this analysis it becomes clear that the *only* requirement for time-stretching is for the analog input frequency to be much less than the optical carrier frequency. In the detailed analysis carried out in [25], the starting pulses are assumed to have Gaussian shapes with pulsewidth T_0 and the terms comprising T_0 are ignored to satisfy the aforementioned condition.

The frequency-dependent phase terms $\cos(\phi_{\text{DIP}})$ results in nulls in the frequency response. This arises due to destructive interference between the two RF components produced by the beating of the optical carrier with the upper and lower modulation sidebands at the photo-detector as illustrated in Fig. 7. This is known as the dispersion penalty in the photonic time stretch [25] and is qualitatively the same phenomenon that occurs in fiber-optic communication links. However, the dispersion penalty is not fundamental

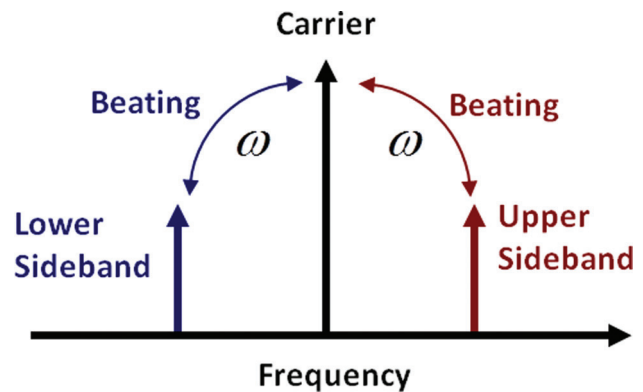


Figure 7 (online color at: www.lpr-journal.org) Dispersion penalty arises due to destructive interference between the two RF components produced by the beating of the optical carrier with the upper and lower modulation sidebands at the photo-detector.

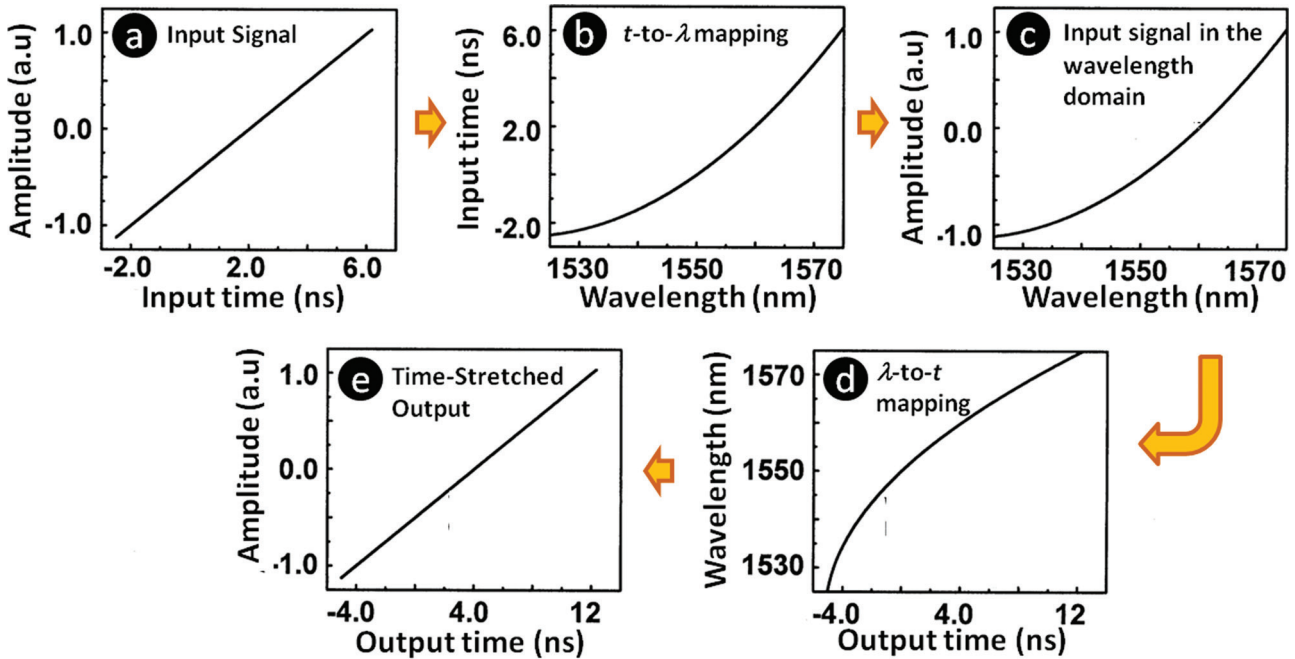


Figure 8 (online color at: www.lpr-journal.org) Graphical description of the time–wavelength transformation. (a) Input signal. (b) Time–wavelength transfer function associated with nonlinear dispersion in the first dispersive fiber. (c) Input signal after time-to-wavelength mapping. (d) Wavelength–time transfer function after the second dispersive fiber. (e) Output time-stretched signal. The stretch process is linear (uniform) despite the nonlinear fiber dispersion.

and can be eliminated. As shown later in this manuscript (Section 3), techniques such as phase diversity and single-sideband modulation overcome the dispersion penalty and provide an ideal impulse response characterized by a flat frequency response.

A physical understanding of time stretching can be obtained from Fig. 8, which shows the evolution of the signal through the system. To highlight the effect of wavelength-dependent GVD, we use a value $\beta_3 = 1 \text{ ps}^3/\text{km}$ which is an order of magnitude higher than that in a single-mode fiber (SMF-28). For simplicity, we consider a linear ramp for the input signal, shown in Fig. 8(a). Assuming operation in the anomalous dispersion regime of the fiber, the λ -to- t mapping is not linear and, in particular, has positive concavity, as shown in Fig. 8(b). This results in an apparent distortion of the signal when the time-domain signal is mapped into the wavelength domain by modulating the ramp signal on the chirped pulse, as shown in Fig. 8(c). However, the λ -to- t mapping in the second fiber has the opposite curvature, as shown in Fig. 8(d), resulting in a linear (and stretched) output after the photodetection, shown in Fig. 8(e). As shown previously, this property is independent of the length of the fibers (hence, independent of the stretch factor) as long as the two fibers have identical dispersion behaviors.

While the time-stretch technique performs linear mapping of the input to output time-scales, mismatches between these parameters (β_3 , β_4 , etc.) lead to non-ideality in the linear mapping of time scales. The non-zero β_3 introduces a slow amplitude modulation in the signal over the stretched pulse duration [25]. If the higher order dispersion param-

eters are not the same for the two dispersive fibers, another effect, called the time-warp is introduced, which can be mitigated using the algorithm discussed in Section 6.

2.3. Fundamental considerations in time-stretch ADC

There are several inherent advantages of using the time-stretch technique that enable us to improve the resolution (i.e., ENOB) and bandwidth of ADCs using the time-stretch technique. However, as in the case of conventional ADCs, there are also a number of sources of noise and distortion in the TSADC that limit its resolution and dynamic range. Since the TSADC is essentially a dispersive analog optical link, noise and distortion effects in the system can be analyzed via a link analysis. The optical signal at the photo-detector input results in an electrical current with a magnitude ηP_{in} . In an analog optical link (and the TSADC), the information is modulated over an optical signal. Hence, power in the information carrying component of the electrical signal is dependent on the modulation depth and can be written as,

$$i_{\text{signal}}^2 R = \frac{1}{2} (m\eta P_{\text{in}})^2 R. \quad (2.13)$$

This signal power is compared with noise and distortion components to obtain the ENOB (effective resolution) of the ADC defined in (1.3). The contributions of

different noise and distortion components are discussed in the following subsections.

2.3.1. Noise

Typically, the readout resolution (in bits) from an ADC is about one bit higher than the ENOB resolution of the ADC, except in case of subsampling ADCs. Higher readout resolution (or higher number of quantization steps) makes the effect of quantization noise in the ADCs insignificant. Here we consider the contributions of different noise sources in a TSADC.

Shot noise. The quantum nature of light results in *shot noise*, with its distribution governed by the Poissonian statistics. The mean-squared shot noise current in the TSADC is

$$i_{n,\text{shot}}^2 = 2q\eta P_{\text{in}} B_e. \quad (2.14)$$

Therefore, from equation (2.13) and (2.14), the shot noise limited SNR can be written as,

$$\text{SNR}_{\text{shot}} = \frac{i_{\text{signal}}^2}{i_{n,\text{shot}}^2} = \frac{m^2 \eta P_{\text{in}}}{4q B_e}. \quad (2.15)$$

Optical losses and amplified spontaneous emission noise. Optical amplification using Raman gain in fibers and/or using Erbium-doped fiber amplifiers (EDFAs) is used for compensating optical losses, which also adds amplified spontaneous emission (ASE) noise. The optical losses and the ASE noise dictate the optical noise figure (F_0). For an amplifier with gain G , the output ASE noise power spectral density can be written as [33],

$$\rho_{\text{ASE}} = n_{\text{sp}} h\nu (G - 1). \quad (2.16)$$

This ASE beats with the carrier and with itself at the photo-detector, generating signal-to-ASE and ASE-ASE beat noise currents. The signal-ASE beat noise is integrated only over the electrical bandwidth B_e as it beats with the carrier, whereas the ASE-ASE beat noise depends on both the optical bandwidth B_{opt} of the wavelength channel and the electrical bandwidth B_e (as out of band components are rejected). As a result, the noise current components in electrical domain are given by [33]:

$$i_{n,\text{sig-ASE}}^2 = 4\eta^2 \rho_{\text{ASE}} P_{\text{in}} B_e \quad (2.17)$$

$$i_{n,\text{ASE-ASE}}^2 = 4\eta^2 \rho_{\text{ASE}}^2 B_e B_{\text{opt}} \quad (2.18)$$

In most cases, the ASE-ASE beat noise is ignored since it is much smaller compared to the signal-ASE beat noise. Therefore, using Equations (2.13) and (2.17), the SNR due

to the amplifier ASE noise can be written as

$$\text{SNR}_{\text{signal-ASE}} = \frac{m^2 P_{\text{in}}}{8\rho_{\text{ASE}} B_e} \quad (2.19)$$

Therefore, using Friis' formula [34], the total noise factor of the optical link ($F_{o,\text{total}}$) due to a series of cascaded loss or gain components (with loss or gain G_i and noise factor F_i) can be calculated as,

$$F_{o,\text{total}} = F_1 + \frac{F_2 - 1}{G_1} + \frac{F_3 - 1}{G_1 G_2} + \frac{F_4 - 1}{G_1 G_2 G_3} + \dots + \frac{F_n}{G_1 G_2 \dots G_{n-1}} \quad (2.20)$$

For a passive lossy optical component, the noise factor can simply be replaced by the loss factor of the device. The noise due to losses and ASE is also characterized as shot noise, as it is due to the quantum nature of light. Therefore, the total shot noise current variance for a cascaded optical link gain G can be written as,

$$i_{n,\text{shot,total}}^2 = 2q\eta P_{\text{in}} B_e + 2P_{\text{in}} h\nu (G - 1)\eta^2 B_e F_{o,\text{total}} = 2\eta P_{\text{in}} B_e [q + h\nu (G - 1)\eta F_{o,\text{total}}] \quad (2.21)$$

Thermal noise. The noise contributed by thermal fluctuations in electronic components and the photo-detector are quantified by the thermal noise. The mean squared thermal noise current, when the photo-detector output is directly fed to the front-end of the electronic digitizer (typically a variable gain amplifier), which has input impedance R and electrical noise figure NF_e , is given by,

$$i_{n,\text{thermal}}^2 = \frac{4kTB_e}{R} NF_e + (\eta P_{\text{NEP}})^2 B_e. \quad (2.22)$$

Since the source impedance of a photo-detector is infinite for all practical purposes, a trans-impedance amplifier (TIA) can be connected directly to the output of the photo-detector, which effectively increases the value of impedance R to improve the sensitivity. As a result, the contribution of the thermal noise can be reduced significantly. In this case, for an input referred TIA rms noise current $i_{n,\text{TIA}}$ in electrical bandwidth B_e , the thermal noise current is written as,

$$i_{n,\text{thermal}}^2 = i_{n,\text{TIA}}^2 + (\eta P_{\text{NEP}})^2 B_e. \quad (2.23)$$

The sample-and-hold (S&H) stage periodically samples the analog signal generated by the TIA onto a capacitor through a switch. In addition to the above mentioned thermal noise sources, an error voltage due to thermal fluctuations in the switch is also added to this sampling capacitor. The mean squared error in the captured voltage (due to thermal fluctuations in the switch) is given by kT/C , and it is independent of the sampling frequency.

$$v_{n,\text{thermal}}^2 = \frac{kT}{C} \quad (2.24)$$

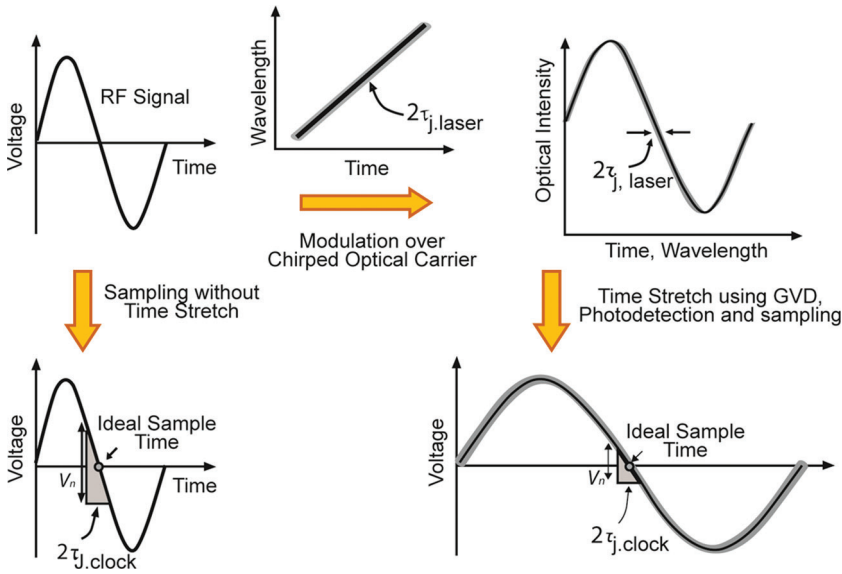


Figure 9 (online color at: www.lpr-journal.org) Sampling a signal with and without time-stretch. When time-stretch technique is used, the noise due to clock jitter becomes insignificant, and noise added by the laser jitter dominates, which is typically much less than the electronic clock jitter (V_n represents the noise voltage).

However, for faster charging/discharging operation in wideband ADCs, the value of sampling capacitance, C , has to be smaller (i.e. higher kT/C noise), which creates a trade-off between sampling speeds and thermal noise-limited SNR in electronic ADCs. Since time-stretching reduces the bandwidth, the kT/C noise constraint is significantly relaxed. Since the kT/C noise component directly influences the resolution of the back-end electronic digitizer, we do not need consider it separately to determine the resolution of the TSADC, if we already know the resolution of the back-end digitizer.

Laser RIN. The laser relative intensity noise (RIN) is the noise introduced into the optical signal due to dynamic fluctuations in the intensity of the laser. It is generally measured on a logarithmic scale with units dB/Hz. Mean squared noise current in the electrical domain due to RIN can be written as,

$$i_{n,RIN}^2 = (\eta P_{in})^2 10^{RIN/10} B_e. \quad (2.25)$$

However, when differential operation is performed in the TSADC using a dual output push-pull Mach-Zehnder modulator [35, 36], the RIN component is common to both outputs of a Mach-Zehnder modulator (assuming the RIN is much above the optical quantum noise limit). Hence, the additive component of the RIN (as defined in [35]) is canceled in differential operation and its contribution becomes,

$$i_{n,RIN,diff}^2 = \frac{m^2}{2} (\eta P_{in})^2 10^{RIN/10} B_e. \quad (2.26)$$

Similar noise rejection is commonly achieved in coherent optical links using a balanced photo-detector [37]. Additionally, when intensity envelope correction is performed by using the envelope from each optical pulse separately [35], the multiplicative RIN component is also rejected, to achieve the shot-noise-limited SNR for the optical signal.

Jitter noise. Clock (or aperture) jitter becomes a significant source of noise in the high-speed ADCs [6]. The clock jitter causes an inaccuracy in the aperture (the time window that defines the sampling point) location in time, as shown in Fig. 9. This inaccuracy in sampling position results in an inaccuracy in the sampled voltage. Clearly, for faster signals, even a small amount of clock jitter can result in a significant error in the captured voltage (as the voltages vary quickly with time). Therefore, the aperture jitter noise is signal frequency (f_{RF}) dependent and can become very significant for moderate to high-speed signals. The aperture jitter limited SNR for rms clock jitter τ_j can be statistically found out to be [6]:

$$SNR_{jitter} = -20 \log(2\pi f_{RF} \tau_j) \quad (2.27)$$

Most of the aperture jitter noise is added by the jitter in the sampling clocks generated by the clock sources. In the time-interleaved electronic ADC architecture used in [38], static timing errors in clocking different sub-ADCs also add the same effect as jitter and limit the achievable SNR. For example, the 20-GS/s ADC reported in [38] shows a resolution of 6.5 effective bits at low frequencies, but the resolution drops to 4.6 effective bits for 6-GHz RF signal because of an effective rms sampling jitter of 0.7 ps. In another example [39], an rms jitter of 250 fs is shown to reduce the effective resolution of a 14-bit ADC to about 11.2-effective bits for a 230-MHz RF signal.

Fortuitously, stretching the signal in time using optical preprocessing reduces the effective signal frequency seen by the S&H block by the stretch factor S . Therefore, as illustrated in Fig. 9, the noise added to the system due to electronic clock jitter is scaled down by S^2 . For example, if a stretch factor of 10 is used in a TSADC, the noise due to clock jitter can be lowered by close to 20-dB compared to a conventional ADC. However, after stretch the timing jitter of the mode-locked fiber laser pulses in the TSADC can become significant. The total effective jitter value in

the TSADC can be written as,

$$\tau_{j,\text{eff}} = \sqrt{\tau_{j,\text{laser}}^2 + \left(\frac{\tau_{j,\text{clock}}}{S}\right)^2}. \quad (2.28)$$

The total mean squared noise current due to jitter noise can therefore be calculated using (2.27) as,

$$i_{n,\text{jitter}}^2 = i_{\text{signal}}^2 \times (2\pi f_{\text{RF}} \tau_{j,\text{eff}})^2. \quad (2.29)$$

Mode-locked fiber lasers can achieve very small jitter values, for example, a mode-locked fiber laser with 18-fs rms jitter has been demonstrated in [40]. Jitter values as low as 1-fs have been predicted and demonstrated, for high frequency components [41]. Low-frequency jitter adds low-frequency phase noise to the digitized signal, which might not be important in many applications. Hence, for such applications, effective jitter performance on the order of 1-fs can be achieved by the optical front-end. On the other hand, the best jitter performance achieved by clocks in high-speed electronic digitizers is on the order of 100-fs. Therefore, the noise limitation due to sampling jitter in high speed ADCs can clearly be overcome by time-stretching the signal. With these major contributors of noise, the total signal-to-noise (SNR) ratio in the stretched RF signal received from the time-stretch preprocessor can be written as,

$$\begin{aligned} \text{SNR}_{\text{total}} &= \frac{i_{\text{signal}}^2}{i_{n,\text{total}}^2} \\ &= \frac{(m^2/2)(\eta P_{\text{in}})^2}{i_{n,\text{shot,total}}^2 + i_{n,\text{thermal}}^2 + i_{n,\text{RIN}}^2 + i_{n,\text{jitter}}^2}. \end{aligned} \quad (2.30)$$

The thermal, shot, and RIN noise components in the above equation are directly proportional to the electrical bandwidth B_e . Hence, larger stretch ratios can be used to reduce the electrical bandwidth and improve the SNR. Larger stretch factors involve longer fibers and more wavelength channels, which requires more optical power to maintain the same power level at the photo-detector inputs. Raman amplification can be used to compensate for these losses (as it can provide a virtually lossless dispersive device) with only a very small increment in the noise spectral density. Therefore, when the bandwidth factor is also taken

into account, larger stretch factors can clearly improve the overall SNR.

When the TSADC uses both the outputs of the MZM to achieve differential operation [36], the contributions of noise components, which are incoherent in the two channels are reduced by 3 dB (because the signal adds coherently whereas noise adds incoherently for these sources). These sources include the shot and the thermal noise. Additionally, the common mode RIN noise can be canceled. Therefore, for differential operation, the SNR achieved is given by

$$\begin{aligned} \text{SNR}_{\text{total,diff}} &= \frac{(m^2/2)(\eta P_{\text{in}})^2}{\frac{1}{2}(i_{n,\text{shot,total}}^2 + i_{n,\text{thermal}}^2) + i_{n,\text{RIN,diff}}^2 + i_{n,\text{jitter}}^2}. \end{aligned} \quad (2.31)$$

The expression for SNR clearly shows that by improving optical signal power and/or modulation depth, the signal-to-noise-ratio can be improved. However, for larger signal levels, nonlinear distortion can become significant, leading to reduction in the dynamic range and ENOB resolution. We briefly discuss the causes of nonlinear distortion in the TSADC in the next section.

Quantization noise. *I. Nyquist ADC:* The quantization noise of a Nyquist ADC is determined by the least significant bit (LSB) of the quantizer. It can be shown that in practical ADCs, quantization noise has a white spectrum [6] and that the total noise power is $P_N = \Delta^2/12$ where Δ is the quantization step. Figure 10(a) represents the power spectrum density of the system before stretching, the signal is assumed to have a bandwidth f_{in} . The sampling rate f_s , according to Nyquist criteria, has to be at least twice the maximum signal frequency. The SNR is given by the hatched area over the gray area. Figure 10(b) represents the power spectrum density of the signal after stretching by a factor of 2. The bandwidth of the signal is reduced by a factor of 2. The signal power is reduced by a factor of 2, but the power spectral density remains unchanged. Similarly the quantization noise power spectral density remains unchanged (the full scale voltage is reduced by $\sqrt{2}$, thus the quantization step can be reduced by $\sqrt{2}$). The SNR is then represented by the hatched area over the gray area in Fig. 10(b) and is unchanged compared to that of the

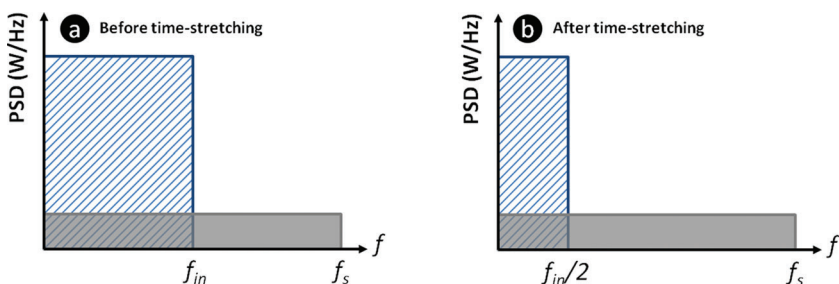


Figure 10 (online color at: www.lpr-journal.org) Power spectral density (PSD) in a Nyquist type ADC (a) before stretching and (b) after stretching by a factor of 2. The signal to quantization noise ratio remains unchanged.

unstretched signal. Hence, the time-stretch process has no effect on the quantization noise of a Nyquist ADC.

II. Σ - Δ ADCs: In Σ - Δ digitizers, the SNR is given by [42],

$$\text{SNR} = \frac{3}{2A} \left(\frac{2L+1}{\pi^{2L}} \right) (2^N - 1)^2 \text{OSR}^{2L+1}, \quad (2.32)$$

where A is the ratio of the amplitude of the signal to the full-scale range of the quantizer, N is the quantizer resolution, and L is the order of the modulator or the number of loops in the Σ - Δ digitizer. Also, in this equation, $\text{OSR} = f_s/f_N$ is the over sampling ratio, where f_s is the actual sampling rate and f_N is the equivalent Nyquist rate. Also, The SNR improves with the oversampling ratio as OSR^{2L+1} .

When the input signal is stretched in time, its bandwidth is reduced by the stretch factor, S . The effect on the Σ - Δ ADC is to increase the OSR. Thus, the SNR is improved by a factor S^{2L+1} . For a first order modulator with a one bit quantizer, the SNR improves by 9 dB (~ 1.5 bit) and 15 dB (2.5 bit) for every octave of time-stretch for a 1st- and 2nd-order Σ - Δ quantizer, respectively [43].

2.3.2. Dispersion penalty

As discussed in the previous section, electro-optic modulation creates the sidebands of the electrical signal in the optical field. When the two sidebands beat with the optical carrier at the photo-detector, the beat terms are in phase and add to recreate the electrical signal in the photo-detector. However, dispersion adds different (optical frequency dependent) phases to these two sidebands. Hence the resultant two beating components at the photo-detector output will no longer be in phase. Since the phase difference is a function of the frequency, the resultant electrical signal amplitude will be frequency dependent with null frequencies at which the two sidebands are 180 degrees out of phase. The dispersion penalty limits the bandwidth of the TSADC but it can be eliminated using one of two techniques: single sideband modulation or phase diversity techniques. A detailed discussion of this topic appears in Section 3.

2.3.3. Nonlinearities

As in any analog communication links, the signal can suffer distortion in the time stretch ADC. The sources of this distortion include the nonlinear transfer function of the Mach-Zehnder modulator, additional nonlinearity when the modulation sidebands produced by the modulator are dispersed during time stretch, photo-detector saturation, all-optical nonlinearities, and nonlinearities of electronic circuits. While larger signal amplitudes (large modulation depth) are preferred for better SNR, increasing the signal power causes intermodulation and harmonic distortion and degrades the signal-to-distortion ratio (SDR). A tradeoff exists between the two when choosing the optimum optical power level (and modulation index) in order to achieve the

best dynamic range and ENOB. Fortunately, since the nonlinear distortion is primarily deterministic and not random, it can be suppressed to a large extent using smart architectures and signal processing algorithms. Different contributions of the nonlinear distortions are briefly discussed here.

Mach-Zehnder modulator and dispersion induced nonlinearity. When the optical field is modulated by the electrical signal using a Mach-Zehnder modulator (MZM), it consists of the optical carrier with the upper and lower sidebands at the fundamental frequency, harmonic and intermodulation components (the harmonic components were ignored in the discussion in Section 2.1.1). At the photo-detector, these sidebands beat with the optical carrier and with each other to generate the electrical signal and its harmonics. For a perfect quadrature biased MZM, and in the absence of dispersion, only odd-order harmonic and intermodulation components remain, while even order components cancel each other. However, in the presence of dispersion (or bias offsets in the MZM), the even order distortion components do not cancel each other because of asymmetry in the phases and amplitudes of the upper and lower sidebands introduced by dispersion. To suppress these distortion components, either *differential* and *arcsine* operations [36] or back-propagation algorithm [44] and/or broadband linearization [45] can be used. The effect of a variable and a chirped optical carrier on the spurious free dynamic range (SFDR) has been also studied in Ref. [46]. A novel wavelength insensitive biasing technique has been also developed that reduces the second order-harmonic distortion and thereby, increases the usable optical bandwidth of the MZM [46].

Photo-detector and electronic nonlinearities. For high dynamic range applications, the nonlinear behavior of the photo-detector and the electronics also becomes very important. In a photo-detector at sufficiently high optical power levels, the photo-generated carriers screen the electric field of the p-n junction, reducing carrier collection efficiency. This leads to a reduction in the detector responsivity at high optical powers. To ensure that photo-detector nonlinearity is unimportant, the optical input power level must be significantly lower than the saturation power P_{sat} of the photo-detector. Fortunately, the second-order distortion, which is a major type of nonlinearity added by the photo-detector, can be suppressed using differential (balanced) operation [36]. We note that second order distortion is only important in very wideband (multi-octave) applications. For two differential (180-degree out-of-phase) signals undergoing the same nonlinearity, the even-order distortion components are in phase and appear as a common mode. Differential (subtraction) operation then doubles the signal amplitudes but cancels these even order distortion components. On the other hand, odd order distortion components remain, but can be suppressed digitally using a lookup table or using adaptive or tunable electronic hardware [47, 48]. The nonlinear distortion contributed by electronics (if significant) has a similar behavior and hence can be suppressed

in conjunction with the suppression of photo-detector added nonlinear distortions.

Optical nonlinearities. The mathematical framework presented in Section 2.1.1 ignores the effect of all-optical nonlinearities, which can become significant in case of wide dynamic range TSADC, where high optical powers may be used to maximize the signal to noise ratio. The nonlinear interaction occurs primarily in the long length of dispersive fiber used to stretch the signal after the electrooptic modulator. Optical pulse propagation under the nonlinear regime in the presence of dispersion in optical fibers can be analyzed using the nonlinear Schrödinger equation (NLSE) described in [30]:

$$\begin{aligned} \frac{\partial A}{\partial z} - j \sum_{m=2} \frac{j^m \beta_m}{m!} \frac{\partial^m A}{\partial t^m} \\ = j\gamma \left[|A|^2 A + \frac{j}{\omega_0} \frac{\partial(|A|^2 A)}{\partial t} - T_R A \frac{\partial|A|^2}{\partial t} \right] \end{aligned} \quad (2.33)$$

Here $A(z,t)$ is the electric field in space and time, β_m represent the dispersion parameters, γ is the nonlinear parameter of the fiber, ω_0 is the center frequency of the optical carrier, and T_R characterizes the delayed nonlinear response in the fiber. The terms on the right hand side square brackets represent the non-linear response corresponding to Kerr effect, self-steepening and Raman effect, respectively. In case of a wide dynamic range continuous time TSADC, the Kerr effect (or self-phase modulation) term can become significant.

The effect of optical nonlinearities in the long dispersive fiber can be numerically simulated using the split-step Fourier method [30, 49]. To minimize optical nonlinearity and obtain good SNR, the optical power levels have to be kept below the nonlinear threshold. At the same time, the power must be large enough to obtain the desired SNR and ENOB. To maintain this delicate balance, distributed Raman amplification can be used, to not only compensate for the loss of the dispersive fiber but also to maintain a relatively uniform and optimum power level inside the fiber. Fortunately, the effect of optical non-linearity in the TSADC is also tolerable because the nonlinear interaction length in the fibers is small thanks to dispersion and wide optical bandwidths used in the TSADC. A detailed discussion on optical nonlinearity and its impact on performance of the TSADC is presented in Section 5.

2.3.4. Time warps correction, and channel-to-channel stitching for continuous operation

The time stretch process modifies the time base of the electrical signal. Ideally, the mapping between the original time base to the stretched time base is linear, i.e., the stretch factor is uniform over the time scale of the stretched pulse. However, in practice, there are a number of non-idealities that result in a non-uniform time transformation. Counterintuitively, optical frequency dependent dispersion char-

acterized by β_3, β_4 , etc. do not cause non-uniform (time dependent) stretch factor as long as the two fibers, one used to create the chirped carrier pulse and the other used to stretch the modulated waveform, have identical dispersion coefficients per unit length (note they can be of different length) [25]. Another source of non-uniform time stretch is self-phase modulation suffered in the first dispersive fiber that occurs near the input of the fiber, where the pulse peak power is high. These non-idealities make the stretch factor time dependent within the stretched pulses adding small amount of phase modulation to the signal.

Another issue that needs to be considered for a continuous-time TSADC implementation is the stitching of signal segments obtained from different parallel channels. These segments need to be aligned properly in time before they can be combined, which is challenging to achieve purely by hardware. Fortunately, both the time-warp and channel misalignment problems are static and deterministic, and are similar in nature. Hence, using training (calibration) signals and digital signal processing techniques, the time-base error can be measured and corrected in the digital domain, as discussed in Section 6.

2.3.5. Time-bandwidth product of TSADC

A crucial feature of the photonic time-stretch system is the spectral efficiency, i.e. the optical bandwidth required to capture a certain time segment (time aperture) of an RF signal with a given RF bandwidth. It is naturally desirable to maximize the time aperture so that more of the signal is captured. The time aperture [25] of the PTS system is equal to the width of the optical pulse after the first dispersive fiber. When double side-band modulation (DSB) is employed to modulate the RF signal onto the pre-chirped pulse, a frequency-fading phenomenon due to the dispersion penalty occurs. The overall effect is to limit the effective 3-dB RF bandwidth which, for the same stretch factor, decreases with the time aperture resulting in a tradeoff between the RF bandwidth and the aperture length. This time-bandwidth product (TBP) increases with the optical bandwidth. Hence spectral usage efficiency is important because improving the spectral efficiency equates to increasing the TBP for the same optical bandwidth. To this end, a dual-polarization photonic time-stretch (DP-PTS) technique has been developed [50], which exploits polarization multiplexing to improve the spectral efficiency.

2.4. Time-Stretch Fourier transform for high-throughput single-shot spectroscopy

The photonic time-stretch technique relies on wavelength-to-time mapping by employing group-velocity dispersion (GVD). In a spin-off application, it has been used to perform Fourier transformation on an optical signal [51]. It indeed replaces a diffraction grating and detector array with a dispersive fiber and single-pixel detector, enabling

ultrafast real-time spectroscopy and imaging. In this section, we briefly discuss the underlying mathematics, and show how a time-stretch Fourier transform (TS-FT) is realized.

In order to examine the role of GVD, we begin with a hypothetical optical field, $E(t)$, that propagates through a dispersive medium. The propagation constant in a medium can be written as,

$$\beta(\omega) \approx \beta_0 + \beta_1(\omega - \omega_0) + \frac{1}{2}\beta_2(\omega - \omega_0)^2 + \frac{1}{6}\beta_3(\omega - \omega_0)^3 + \dots \quad (2.34)$$

where ω is the optical frequency and β_n is the n -th order GVD parameter. The parameters, β_0 and β_1 add a constant phase and a latency, respectively. Both are inconsequential as it relates to wavelength-to-time mapping and time stretching. The quadratic 2nd-order GVD term is the most important, and after propagation over length, z , it changes the phase of each spectral component of optical field by,

$$e^{-j\beta \cdot z} = e^{-j\beta_2 \omega^2 z / 2}. \quad (2.35)$$

Hence, the optical field can be written as,

$$E(t) = \int E(\omega) \cdot e^{-j\beta_2 \omega^2 z / 2} \cdot e^{j\omega t} d\omega, \quad (2.36)$$

where $E(t)$ is the temporal profile of the dispersed optical field, and $E(\omega)$ is the Fourier transform, or equivalently the spectrum of the field, and $\beta_2 z$ is the GVD produced by a linearly dispersive medium of length z . The time-domain waveform after photo-detection is proportional to optical intensity,

$$|E(t)|^2 = \left| \int E(\omega) e^{-\frac{j\beta_2 z}{2} \left(\omega - \frac{t}{\beta_2 z}\right)^2} d\omega \right|. \quad (2.37)$$

If GVD parameter, β_2 , is large, then only $\omega_{opt} = t/(\beta_2 z)$ contributes to the integral. For other frequencies the argument oscillates rapidly and averages out to zero. In optics, this is known as *Stationary Phase Approximation (SPA)* [52]. In physics and mathematics, it is known as the *Saddle Point Approximation*.

As evident from (2.37), at each time instant, t , only one frequency survives and that frequency depends linearly on t . In other words, there is a one-to-one correspondence between time and frequency. Hence, frequency-to-time or wavelength-to-time mapping is achieved. This process, which enables detection of optical spectrum in time-domain, is also called dispersive Fourier transform (DFT) [53, 54]. Note that the time scale in the time-frequency map has a scale factor of $\beta_2 z$; this is the total dispersion that slows down the time scale of the measured signal – it stretches the signal in time. Hence this technique is also known as the time-stretch Fourier transform (TS-FT). The dispersive fiber can also amplify the light, via stimulated Raman scattering, to overcome the noise of

the photodetection circuitry, resulting in high sensitivity detection [26, 52, 54].

2.5. Comparison of time stretch with time lens

While the time-stretch technique is inherently a dispersive analog optical link and was inspired from a work on analog optical links for phase array antennas, it has at times been re-interpreted in terms of its analogy with time lenses [12, 55, 56]. While such re-interpretation does not serve any practical purpose, it may be useful for purely a comparison reason. The time-lens relies on the mathematical equivalence between spatial diffraction and temporal dispersion, or the so called space-time duality, as shown in Fig. 11. It was first introduced in a classic article by Caputi in 1971 [32] and applied to optics by Kolner et al. in 1989 [57] and later advanced by Bennett et al. [58] and most recently by Foster et al. [59].

A lens held a fixed distance from an object produces a magnified image at the screen. It imparts a quadratic phase shift to the spatial frequency components of the optical waves. As the optical waves propagate further, they focus on to the screen generating a magnified image. Owing to the mathematical equivalence between paraxial diffraction and temporal dispersion, an optical waveform can be temporally imaged by following the three step process of applying dispersion (quadratic phase shift in frequency), quadratic phase shift in time (the time-lens), and dispersion again. A focused aberration-free image is only obtained under a specific condition when the quadratic phase shifts imparted in frequency (due to dispersion) and the quadratic phase shift in time satisfy the temporal equivalent of the classical lens equation. Alternatively, the time lens can be used without the second dispersive element to transfer the

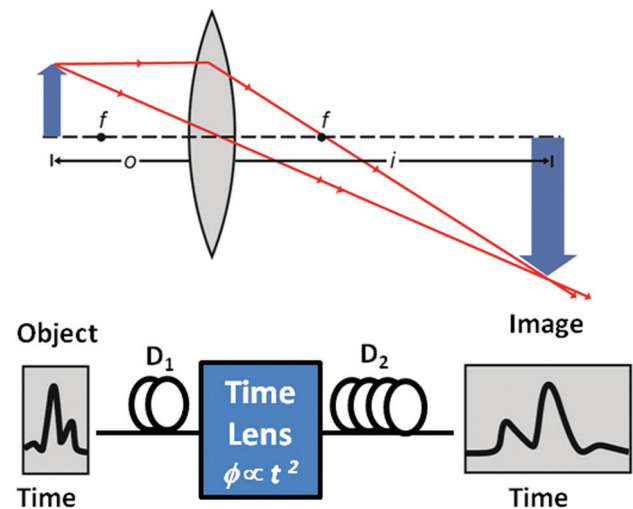


Figure 11 (online color at: www.lpr-journal.org) Comparison between spatial imaging (top) and temporal magnification of an ultrafast waveform (bottom), which are related to each other owing to space-time duality.

waveform's temporal profile to the spectral domain, analogous to an ordinary lens that produces the spatial Fourier transform of an object at its focal points [59, 60]. Here a spectrometer would be used to read the output however, the frame rate (throughput) of such a system would be very slow due to the very low real-time throughput of optical spectrum analyzers (less than 1 kHz).

In contrast to the time-lens approach, the photonic time-stretch (PTS) system is not based on the space-time duality. No lens equation needs to be satisfied in order to obtain an error-free slowed-down version of the input waveform. It is a simpler and more practical system and has already demonstrated true continuous time wideband analog-to-digital conversion [61], a feature that is needed for real-time oscilloscope applications.

A critical difference between the two techniques is that the time lens requires the input waveform to be dispersed before it is mixed with a chirped optical carrier. For electrical waveforms, the required electronic dispersive elements that have sufficient bandwidth and low loss do not exist. This renders time-lens impractical for slowing down wideband electrical waveforms and hence creating wideband analog-to-digital converters. In contrast, PTS does not have such a requirement. It was developed specifically for slowing down electrical waveforms to obtain extremely high-speed digitizers.

3. Impulse response of TSADC

Ever growing high-speed applications have created the demand for ADCs with up to 100-GHz bandwidth. These applications include cognitive radios that are digital receivers (also known as software-defined radio), test and measurement equipment, receivers for 100G+ optical links and millimeter-wave radio, and radar systems. The critical bottleneck in these applications is the analog-to-digital converter, and the photonic time-stretch technique has the potential to provide ultra-wideband conversion by boosting the input bandwidth and sampling rate of electronic digitizers. Therefore, evaluation of the impulse response of the TSADC, which characterizes its input bandwidth, becomes necessary. The dominant source of bandwidth limitation in the photonic time stretch is the dispersion penalty. In this section, it will be shown that dispersion penalty can be eliminated and TSADC can achieve an ideal impulse response.

3.1. Dispersion penalty

The photonic front-end of the TSADC is fundamentally a modified analog optical link that uses chirped optical carrier pulses instead of continuous wave (CW) light. Hence, the impulse response functions of the two systems have similar behavior. Fortunately, since the output of the TSADC is available in the digital domain, it becomes possible to cor-

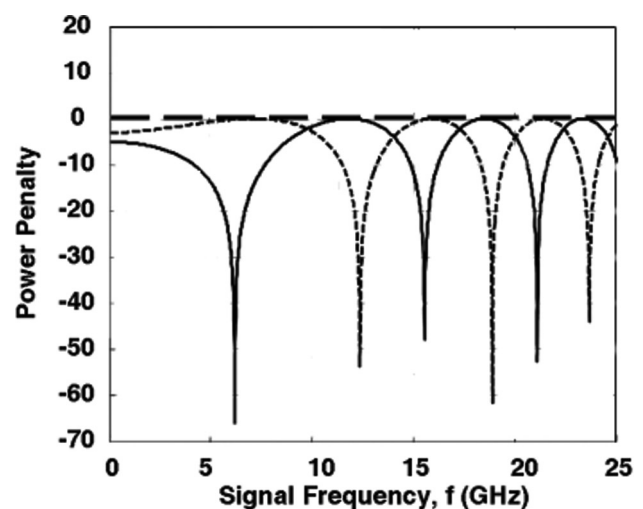


Figure 12 (solid line) Dispersion penalty behavior in a conventional optical link and in the photonic time-stretch ADC (TSADC). The dispersion penalty, characterized by frequency fading (nulls) arises from destructive interference between the upper and lower modulation sidebands when they beat with the carrier inside the photodiode. In practice, the dispersion penalty is eliminated by employing either single-sideband modulation [62], or by taking advantage of the natural phase diversity in the outputs of a dual-output Mach Zehnder modulator [63]. When phase diversity is employed, the outputs have complementary dispersion penalty characteristics (compare dashed and solid lines).

rect for imperfections in its impulse response using digital signal processing (DSP).

In a conventional optical link, the signal is transmitted through the optical fiber by modulating it onto a CW laser. The modulator produces the upper and lower sidebands of the RF signal in the optical spectrum at frequencies $\omega_{\text{optical}} \pm \omega_{\text{RF}}$. In the absence of dispersion, these sidebands beat with the optical carrier at the photo-receiver to reproduce a copy of the original signal. When dispersion is present, the two sidebands slip in phase with respect to each other and interfere at the photo-receiver, creating nulls at certain frequencies (with no signal power). This relative phase shift, thus, results in a non-ideal impulse response with periodic fading characteristic versus frequency, as illustrated by Fig. 12. For a dispersive fiber with dispersion parameter β_2 , fiber length L , and angular frequency ω_{RF} , the two sidebands accumulate additional $\pm \omega_{\text{RF}}^2 \beta_2 L / 2$ phases with respect to the carrier. As a result, at the photo-receiver, the summation of these two sideband products gives the following transfer function:

$$H(\omega) = \frac{Y(\omega)}{X(\omega)} = \cos\left(\frac{\omega_{\text{RF}}^2 \beta_2 L}{2}\right) \quad (3.1)$$

In the photonic time-stretch (PTS) pre-processor, the RF signal is modulated onto a chirped optical carrier, as shown in Fig. 6. Dispersion stretches the chirped carrier along with the modulation in time, giving the stretched replica of the RF signal at the photo-receiver output. As shown in [25],

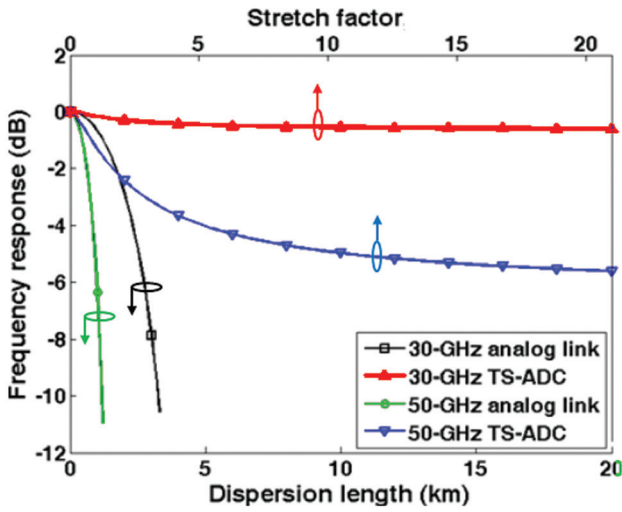


Figure 13 (online color at: www.lpr-journal.org) Dispersion penalty in a conventional optical link and in the TSADC versus dispersion length. Larger dispersion results in a severe dispersion penalty in an optical link, whereas this power penalty saturates with increasing dispersion (or stretch factor) in the TSADC. Hence, very large stretch factors can be achieved without incurring any additional dispersion penalty. As shown below, the dispersion penalty can be eliminated by employing either phase diversity or single-sideband modulation techniques.

because of time-stretch, the transfer function is modified to

$$H(\omega) = \frac{Y(\omega)}{X(\omega)} = \cos\left(\frac{\omega_{RF}^2 \beta_2 L}{2S}\right) = \cos(\phi_{DIP}), \quad (3.2)$$

where the stretch factor S and the dispersion-induced phase ϕ_{DIP} are defined in Section 2. This characteristic frequency-dependent fading of the optical link and the PTS pre-processor is known as the dispersion penalty (Fig. 12). Though the two optical links have similar fading characteristics, there also exists a remarkable difference.

In a conventional optical link, increasing the length of the transmission fiber (or the dispersion value) increases the dispersion penalty at a particular frequency. On the other hand, in the PTS pre-processor, this penalty saturates, which implies that the signals can be slowed down by very large factors without incurring additional power penalty, as evident from (3.1) and (3.2). In Fig. 13, the chirp rate corresponds to the dispersion of a 1-km long standard single mode fiber (SSMF), i.e., 17-ps/nm/km dispersion. In the next section, we discuss different techniques that can be used to overcome the power penalty due to dispersion and achieve the ideal impulse response of unity in the TSADC.

3.2. Dispersion penalty mitigation techniques

Several techniques have been devised that can mitigate the dispersion penalty effects to fully recover the originally

transmitted signal. These techniques either involve eliminating one of the sidebands of the signal in the optical field, or using phase diversity to recover the signal from two measurements that have complementary frequency fading characteristics. The phase diversity techniques are especially suited for the TSADC, as real-time signal processing can easily be performed in DSP, thanks to advancements in highly efficient CMOS technology. The techniques used for mitigating the dispersion penalty are discussed in the following subsections.

3.2.1. Phase diversity technique

When a dual-output single-electrode Mach-Zehnder modulator (MZM) is used to modulate the intensity of the optical field, the two outputs have opposite chirps, as shown in Fig. 14. Chirp is the additional phase modulation component in an amplitude modulated optical field, which modifies the dispersion penalty behavior of the optical link. Since the two outputs of the modulator have complementary chirps, they have complementary fading characteristics [63]. When the chirp factor is unity, a null at one of the outputs after dispersion at certain frequency implies a maximum at the other output (for the same frequency). The two outputs can be combined in different ways to fully recover the originally transmitted signal, implying practically an unlimited bandwidth in the system; hence, an ideal impulse response.

For the TSADC employing phase diversity (with an intensity modulator having chirp factor of ± 1), the two output transfer functions (shown in Fig. 15) can be written as [63]:

$$H_1(\omega) = \cos\left(\frac{\omega^2 \beta_2 L}{2M} - \frac{\pi}{4}\right) \quad (3.3)$$

$$H_2(\omega) = \cos\left(\frac{\omega^2 \beta_2 L}{2M} + \frac{\pi}{4}\right) \quad (3.4)$$

With the phase diversity technique, the following methods can be employed for complete recovery of the original signal.

Maximal ratio combining algorithm. The frequency-dependent signal fading in the two outputs of a phase-diverse TSADC is similar to spatial fading in wireless communications links due to multipath effects. In wireless communications, this fading is overcome by the use of maximal ratio combining (MRC) of the signals obtained from spatially-separated antennas. In the MRC algorithm, weighted summation is used to combine the signals from different channels to obtain the original signal. The frequency dependent weighting coefficients are proportional to signal amplitudes obtained from different channels. Therefore, the final output $Y(\omega)$ is obtained from the two time-stretch pre-processor outputs $Y_1(\omega)$ and $Y_2(\omega)$ as,

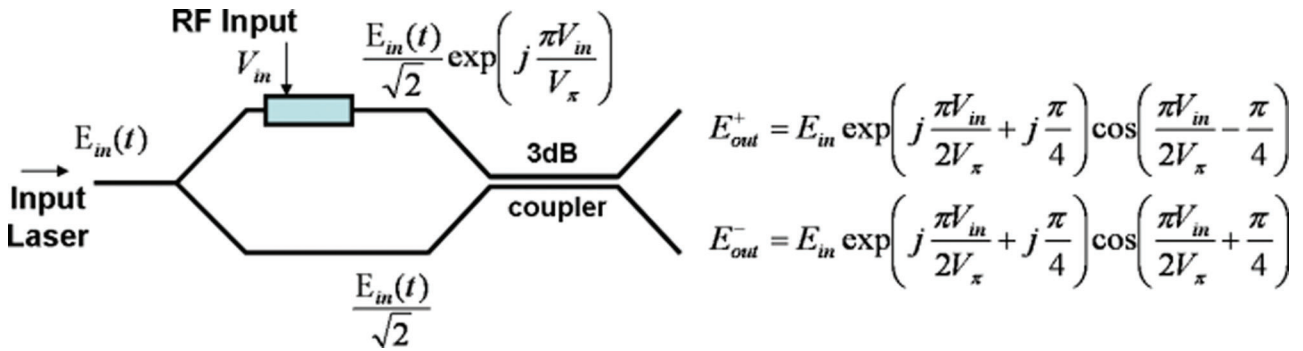


Figure 14 (online color at: www.lpr-journal.org) In the single electrode Mach-Zehnder modulator, the intensity modulation (cosine term) phases are complementary in nature with respect to chirp (exponential term) phases in the two outputs. This phase diversity results in complementary frequency fading characteristics after dispersion. This fortuitous feature of the modulator is used to eliminate the frequency fading (nulls) and hence remove the bandwidth limitation of the photonic time-stretch system.

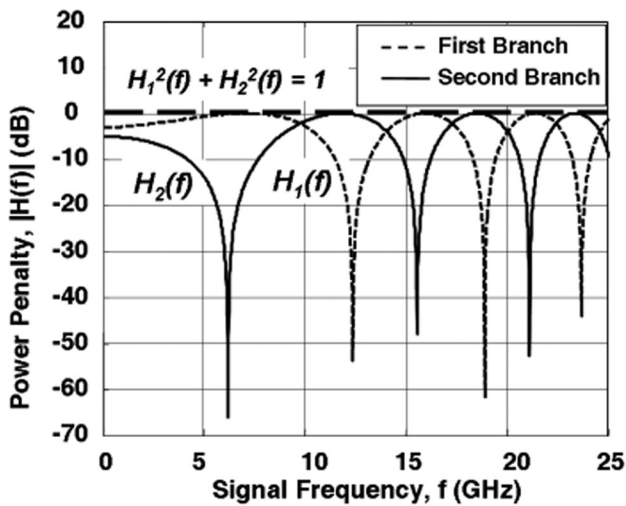


Figure 15 Frequency response for the two phase-diverse TSADC outputs, showing complementary frequency fading behavior [63]. This powerful feature inherent in a dual-output Mach-Zehnder modulator allows the user to eliminate the dispersion penalty and hence the bandwidth limitation of the time-stretch pre-processor. The plot shows how a flat frequency response is achieved; this can be done by summing the two outputs. In practice, however, a maximum-ratio combining is used for better signal-to-noise ratio [63]. The use of this technique for eliminating the dispersion penalty in fibers is not limited to the time stretch system. It can also be employed in digital and analog fiber optic communication links.

$$Y(\omega) = \frac{H_1(\omega)Y_1(\omega) + H_2(\omega)Y_2(\omega)}{\sqrt{|H_1(\omega)|^2 + |H_2(\omega)|^2}}. \quad (3.5)$$

As evident from (3.5), for any input signal $X(\omega)$, the transfer function for the final output $Y(\omega)$ turns out to be unity. Even if the magnitude of the chirp factor is not unity, the signal can be completely recovered without loss of any information as long as phase diversity due to non-zero chirp exists. This, in fact, ensures that the two channels never have

a common null frequency. The phase diversity technique with MRC has been used to demonstrate an ultra-wideband TSADC with an ideal impulse response [63]. When the chirp factor and dispersion parameters of the link are not exactly known, an adaptive two-dimensional spatio-temporal signal processing algorithm can be employed to mitigate dispersion penalty fading [64]. The MRC technique ignores the nonlinearities added due to the non-linear MZM transfer function and dispersion that are discussed in Section 4. However, the back-propagation algorithm discussed below is able to eliminate these nonlinear distortions.

Back-propagation algorithm. The back-propagation algorithm can be used for obtaining a distortion-less signal from the two phase-diverse outputs of the time-stretch pre-processor [44]. It requires use of a single-electrode MZM, in which only one arm of the MZM phase-modulates the signal (i.e., chirp factor = ± 1), as shown in Fig. 16. This simplifies computation of the optical fields at the inputs of the two photo-detectors that are used for recovering the original signal.

In this algorithm, the modulated field A_M at the output of the phase modulating arm in the MZM can be accurately obtained by numerical back-propagation of the optical fields at the two photo-detectors (as shown in Fig. 16). Optical intensities I_{D1} & I_{D2} , measured at the detector, are obtained from the superimposed optical fields from the modulated arm of the Mach-Zehnder interferometer (P_M) and that from the non-modulated arm (P_0), after propagation through the second dispersive fiber.

$$I_{D1} = |P_0|^2 + |P_M|^2 + 2|P_0 P_M| \cos(\varphi_p) \quad (3.6)$$

$$I_{D2} = |P_0|^2 + |P_M|^2 - 2|P_0 P_M| \cos(\varphi_p) \quad (3.7)$$

Hence, P_M can be calculated unambiguously from the I_{D1} & I_{D2} :

$$|P_M| = \sqrt{\frac{I_{D1} + I_{D2}}{2} - |P_0|^2} \quad (3.8)$$

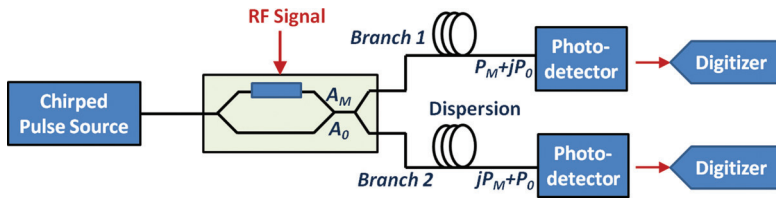


Figure 16 (online color at: www.lpr-journal.org) Phase-diverse TSADC employing the back-propagation technique for eliminating the bandwidth limitation associated with dispersion penalty. From intensity measurements I_{D1} & I_{D2} , the RF signal represented by the phase of modulated field A_M can be obtained by calculating A_M numerically.

$$\phi_P = \cos^{-1} \left(\frac{I_{D1} - I_{D2}}{4|P_M||P_0|} \right) \quad (3.9)$$

$$P_M = |P_M| \exp(i(\arg(P_0) + \phi_P)) \quad (3.10)$$

where ϕ_P is the phase difference between the two fields at the detector. The magnitude of P_0 (the non-modulated optical field component) can be established from the envelope of the measured pulses. The phase of P_0 can, for slowly varying pulse envelopes, be assumed to be constant. Having calculated the complex P_M , it is trivial to back propagate the field to the phase modulation point (A_M), at which the input signal voltage can be calculated. This approach not only removes dispersion penalty fading, but also removes any nonlinear distortions added to the signal due to generation of signal harmonics in the optical field when the signal amplitudes are large, as demonstrated in [65].

3.2.2. Single sideband techniques

As discussed earlier, the dispersion penalty is caused when the two sidebands of the RF signal slip with respect to each other and interfere destructively. This problem can be overcome if one of the sidebands of the signal in the optical field is suppressed, and hence, resulting in an ideal impulse response of the system. The following techniques can be used to accomplish this goal.

Single sideband modulation. A dual-drive Mach-Zehnder modulator has two phase-modulating arms that can be independently driven by RF sources. It can be used to modulate the optical field with the RF signal in one arm and its quadrature in the other arm (as shown in Fig. 17). In this case, when the modulator is biased at quadrature point, one of the RF sidebands in the optical field from the two arms adds destructively at the output coupler, whereas the other sideband adds constructively. This suppresses one of the sidebands, and thereby, eliminates the frequency dependent fading even in the presence of dispersion. This technique is known as single sideband modulation and it is commonly used in analog optical links and wireless communications systems. The single-sideband modulation has been used to demonstrate dispersion penalty mitigation in the TSADC [66]. The bandwidth of the hybrid coupler sets the limit on the maximum system bandwidth that can be achieved.

Time-gated filtering. In the time-stretch ADC, the electro-optic modulation generates sidebands of the signal in the

chirped pulse. In a conventional TSADC, this chirped pulse is dispersed to stretch the signal and slow it down in time. Instead of stretching, if the modulated chirped pulse is first compressed using dispersion of opposite sign, the two signal sidebands can be separated in time (shown in Fig. 18). One of the signal sidebands in the optical field can now be removed by time gating [67]. If the resultant optical signal is dispersed, a dispersion-penalty-free stretched signal with single sideband is obtained.

It should be noted that even though the single-sideband technique eliminates the frequency dependent fading, the group-delay variations versus frequency need to be equalized to achieve an undistorted impulse response. Thanks to advancements in low-cost CMOS technology, this equalization can be easily performed digitally using simple linear tapped delay filters.

3.3. Ideal impulse response of TSADC

Different techniques described in the previous sections can be used to overcome the dispersion penalty in the TSADC. However, the limited bandwidth of the Mach-Zehnder modulator can also affect its impulse response. Fortunately, these modulators can be designed to operate with 100-GHz bandwidths, which is sufficient for almost all practical applications. For example, 110-GHz electro-optic modulators have been demonstrated in [56] and the commercial availability of 100-Gbps modulators has been announced by GigOptix, Inc [68]. Therefore, for all practical electrical signals, an ideal impulse response can be obtained in the TSADC. As an example, a phase-diverse TSADC is simulated with a 10-ps Gaussian-pulse-shaped electrical signal and a stretch factor of 100 [69]. Figure 19(a) shows the two phase-diverse outputs captured by a 3-GS/s digitizer. The signal reconstructed using the back-propagation technique perfectly matches the input 10-ps Gaussian pulse [Fig. 19(b)].

4. Nonlinear distortion and its correction in TSADC

All real world analog systems exhibit some degree of nonlinear behavior, even though the nonlinearity can be negligible. Nonlinear behavior induces distortion to the signal as the output amplitude does not change perfectly linearly with respect to the input. This becomes more severe for large amplitude signals. Nonlinearity can cause gain modulation,

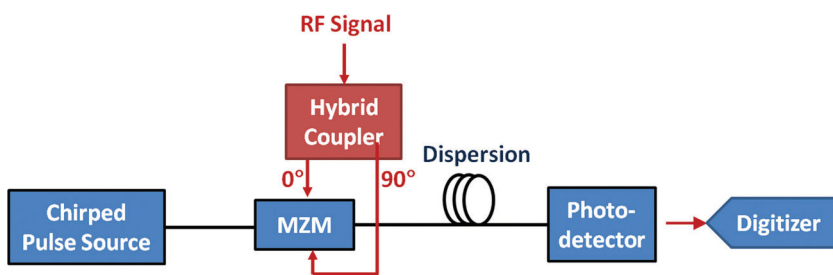


Figure 17 (online color at: www.lpr-journal.org) Time-stretch ADC employing a dual-drive modulator to achieve single sideband modulation. Single sideband modulation eliminates the frequency dependent fading caused by dispersion penalty and can be used instead of the phase diversity technique. The choice depends on which architecture is more readily implementable in a particular application.

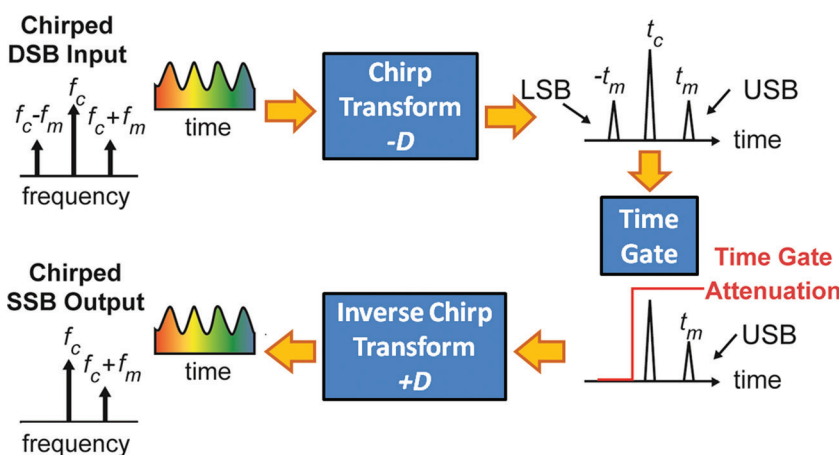


Figure 18 (online color at: www.lpr-journal.org) Application of time-gated filtering to remove one of the signal sidebands in the optical field. This technique can be used to mitigate dispersion penalty in the TSADC [67]. DSB: double sideband, SSB: single sideband, LSB: lower sideband, USB: upper sideband.

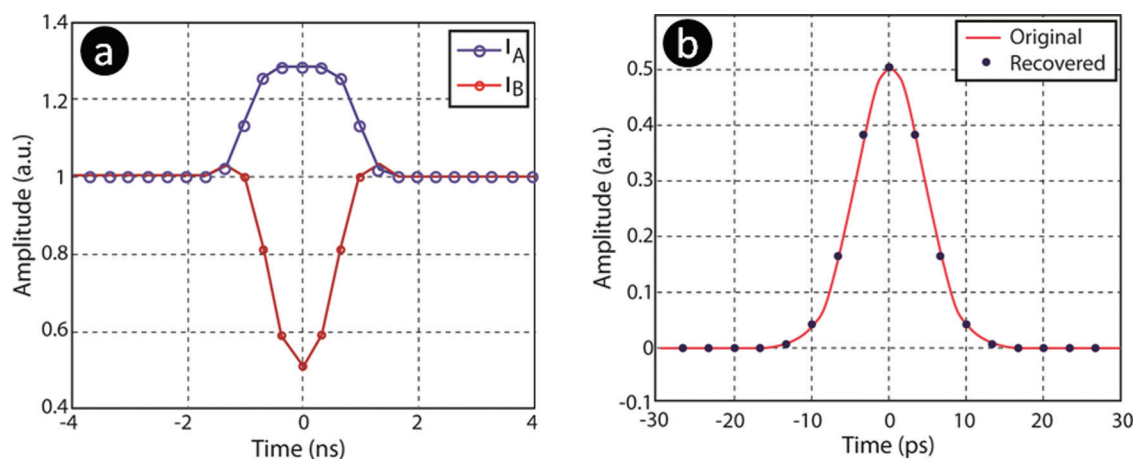


Figure 19 (online color at: www.lpr-journal.org) (a) Simulation results showing a 10-ps Gaussian pulse captured by the phase-diverse time stretch ADC with a stretch factor of 100. Two output channels are denoted by I_A and I_B . (b) The original signal and the reconstructed signal after numerical back-propagation (the effective sample rate is 300 GS/s). These simulations show that the TSADC has no fundamental bandwidth limit imposed by dispersion. Simulations do not include the practical limit set by the maximum frequency response of the MZ modulator which at the time of this writing is between 100–150 GHz [27, 55, 68]. © 2009 IEEE. Reprinted, with permission, from [69].

resulting in mixing of different frequency components, and hence, generates new frequencies that are within the bandwidth of the signal, and cannot be filtered out. As an example, due to nonlinearity, an out-of-band signal can interfere with the signal-of-interest and result in loss of information. Even in the absence of an interferer, the nonlinearity can result in self-phase modulation and saturation, and thereby, limits the dynamic range of the system.

The nonlinear behavior can be memory-less or dynamic (i.e., it can show memory effects) [70]. Memory-less nonlinearity is frequency independent, resulting in a direct mapping between the instantaneous amplitude of the input signal to the corresponding output signal amplitude. On the other hand, in the presence of memory effects, nonlinear distortion of the signal depends upon input signal behavior over a period of time instead of a single time

instant. Correcting for memory-less nonlinearity is relatively easy as it requires a one-dimensional lookup table that maps the observed signal amplitudes to the correct values (assuming a one-to-one mapping between input signal and its corresponding output). However, the presence of memory effect makes this task extremely challenging even if the system transfer function is well known. For such a system, the response of the system is approximated by multi-dimensional coefficients – such as Volterra series kernels [70–72]. In practical systems, obtaining these coefficients becomes very challenging. Moreover, even if these coefficients are known, obtaining the inverse of the transfer function to estimate the input to the system from the observed output may be extraordinarily difficult and computationally intensive. In this section, the origin of the nonlinear distortion in the electrical signal due to various effects in the TSADC is described. The techniques developed to overcome this distortion are also discussed here. It should be noted that the effect of optical nonlinearity occurring inside the optical fiber are discussed separately in Section 5.

4.1. Nonlinear distortion in TSADC

In a TSADC, the analog RF signal modulates the optical field, generating RF signal sidebands and their harmonics in the optical field as shown in Fig. 20. In the presence of dispersion, these harmonics and sideband components undergo different phase shifts at different frequencies, and, therefore, frequency-dependent nonlinear distortion at the photo-receiver output occurs. A detailed mathematical derivation of these distortion components is available in [25]. The major sources of the nonlinear distortion in TSADC are discussed below.

4.1.1. Dispersion-induced nonlinearity

In the absence of dispersion and for quadrature biasing of a Mach-Zehnder modulator (MZM) in an analog optical link,

even-order distortion is cancelled; yielding the well-known *sinusoidal* transfer function of the MZM that has only the odd-order distortion components (Fig. 20). In the presence of dispersion, however, the even-order components appear and their intensity increases rapidly as the signal frequency and the amount of dispersion increase. Similar distortion behavior is observed when the signal is obtained from the TSADC. For a multi-octave system, this harmonic distortion can severely limit the dynamic range of the link. In analog links, transmission fiber dispersion can be compensated optically by employing dispersion compensating fibers (DCFs), chirped fiber Bragg gratings (CFBGs), etc. In the case of the TSADC, however, the dispersion is actually used for time stretching, and hence optical compensation techniques are not viable solutions.

4.1.2. Nonlinearity due to MZM bias offsets

Mach-Zehnder modulators have small bias drifts due to temperature variations, stress, humidity, etc. [73]. While bias controllers can be employed to partially control the drifts, if the optical carrier is chirped or varied over a wide range of wavelengths, the bias offsets vary with optical wavelength [46] and therefore, they are not easily controllable. These bias offsets introduce significant 2nd-order distortion that has a different behavior compared to the dispersion-induced nonlinearity. A small DC offset in the *sinusoidal* transfer function creates an imbalance in the symmetry of the sinusoidal transfer function of the MZM, which results in 2nd-order distortion of the signal.

4.1.3. Photo-detector and electronic nonlinearities

All photo-detector and active electronic components such as amplifiers show a saturation behavior. This behavior can cause nonlinear (harmonic and intermodulation) distortion. Typically, the 2nd-order distortion is much stronger compared to other distortion components. For sub-octave bandwidth systems, however, this distortion is generated outside

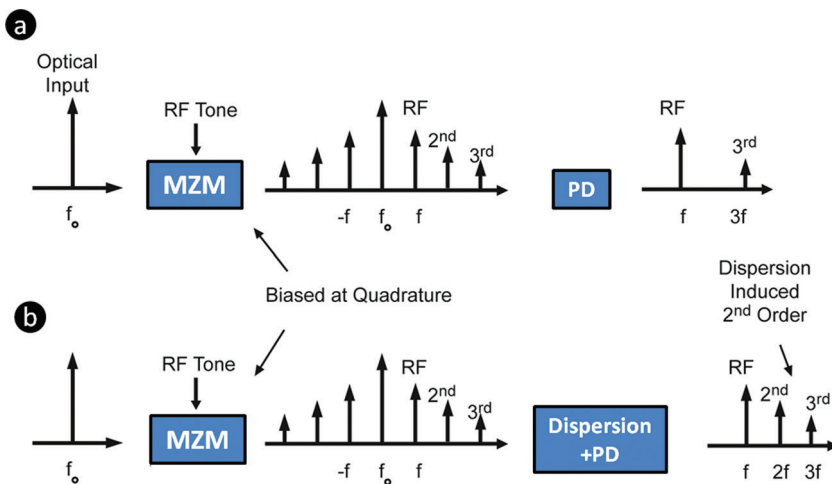


Figure 20 (online color at: www.lpr-journal.org) Nonlinear distortion in an analog optical link caused by the periodic transfer function of the Mach-Zehnder modulator. (a) In the absence of dispersion, only 3rd-order distortion is present at the photo-detector (PD) output. (b) When photo-detection is after dispersive transmission, dispersion breaks the phase symmetry in the modulation sidebands and induces 2nd-order distortion. Mach-Zehnder modulator (MZM) bias offset, i.e. deviation from the ideal quadrature bias point, causes 2nd-order distortion in both cases.

the signal bandwidth and can be filtered out. Unfortunately, for multi-octave systems, this distortion can also lead to a significant degradation in the dynamic range of the system unless removed.

4.2. Nonlinearity suppression techniques in TSADC

The following distortion suppression techniques have been developed for improving the dynamic range of the TSADC, which can be exploited based on the targeted application.

4.2.1. Differential and arcsine operations

The Mach-Zehnder modulators that use an optical directional coupler as the output combiner have two complementary outputs. For an MZM with push-pull operation (dual electrodes), the modulated output fields have zero chirp – a well-known property used in long-haul optical communications [74]. For such modulators biased at quadrature, the output electric fields of the complementary outputs can be written as,

$$E_{\pm}(t) = \frac{1}{\sqrt{2}} E_{in}(t) \cos\left(\frac{\pi}{4} \pm \frac{m}{2} \cos \omega_{RF} t\right), \quad (4.1)$$

where m is the modulation index, $E_{in}(t)$ is the input electric field, and $\cos(\omega_{RF} t)$ is the normalized RF modulation signal. Using the mathematical framework developed in [25], we find that the detector currents obtained after propagation of this field through a dispersive fiber of length L and group-velocity dispersion parameter β_2 , can be written as,

$$\begin{aligned} I_{\pm}(t) = & I_{Env}(t) \times (1 \mp m \cos \phi_{DIP} \cos \omega_{RF} t \\ & + \frac{m^2}{8} (1 - \cos 4\phi_{DIP}) \cos 2\omega_{RF} t \\ & \pm \frac{m^3}{96} (\cos 9\phi_{DIP} + 3 \cos 3\phi_{DIP}) \\ & \times \cos 3\omega_{RF} t + \dots), \end{aligned} \quad (4.2)$$

where $\phi_{DIP} = \beta_2 \cdot \omega_{RF}^2 \cdot L / 2$ and $I_{Env}(t)$ is the photo-detector current in the absence of modulation. Clearly, odd harmonics in the expressions for I_+ and I_- are 180 degrees out-of-phase, whereas the even harmonics are in-phase. Thus, taking the difference of I_+ and I_- removes all even-order nonlinear distortion components (also described in [36]). It should be noted that even though the dispersion-induced 2nd-order distortion is completely removed in theory using differential operation, the cancellation may not be perfect in practice because of amplitude and phase errors in the two complementary signals. For practical applications, these errors are small and can be reduced further with careful design, and hence, significant distortion suppression can be achieved [36]. However, 2nd-order distortion added due to

the MZM bias offsets is not corrected by the differential operation. If the Mach-Zehnder modulator is biased at the quadrature point with a small slow time varying bias offset $\delta(t)$, the two outputs I_+ and I_- after RF modulation by signal $x(t)$, can be written as,

$$\begin{aligned} I_{\pm}(t) = & I_{Env}(t) \\ & \times \left[\begin{array}{c} 1 \mp \sin(m \cdot x(t) + \delta(t)) \\ + \text{dispersion induced distortion components} \end{array} \right]. \end{aligned} \quad (4.3)$$

Typically, the dispersion-induced distortions for RF frequencies that are relatively smaller than the first dispersion-penalty null are negligible. These signals only have 3rd- and higher-order distortions due to the *Sine* function in (4.3) and a 2nd-order nonlinearity caused by $\delta(t)$. Therefore, (4.3) can be rewritten as,

$$I_{\pm}(t) \approx I_{Env}(t) [1 \mp \sin(m \cdot x(t) + \delta(t))]. \quad (4.4)$$

Hence, the input RF signal can be recovered from the detector outputs by performing the following operation [75]:

$$I_{out}(t) = \sin^{-1}\left(\frac{I_+ - I_-}{I_+ + I_-}\right) \approx m \cdot x(t) + \delta(t) \quad (4.5)$$

The subtraction of the intensities in the argument of the inverse sine function in (4.5) removes dispersion-induced 2nd-order distortion because 2nd-order distortion in (4.2) appears as a common mode in the two outputs. For the summation of intensities in the denominator, ($I_+ + I_-$), we use the sum over many pulses. Therefore, the division operation corrects for the optical pulse envelope. It also helps in the rejection of optical intensity noise or any other multiplicative noise [15, 25]. The *arcsine* operation plays a crucial role in removing the 3rd-order harmonic and intermodulation distortions. In Section 6, we describe how the bias offset error can be eliminated.

There are certain other advantages of using this technique. Owing to the symmetry in the two signals (i.e., I_+ and I_-), the differential operation can be very useful in suppression of 2nd-order (and other even-order) distortions added by the photo-detector and subsequent electronics, provided that there is a good matching between the two differential channels [36]. Additionally, this operation suppresses uncorrelated noise by 3 dB relative to the signal, as the noise adds incoherently whereas signal adds coherently. Differential operation is also able to suppress RIN because it appears as common mode. Lastly, by using this approach, the division operation in (4.5) is also able to remove intensity envelope non-uniformities [25]. Using the *differential* and *arcsine* approach, suppression of nonlinear distortions due to dispersion, and nonlinear MZM transfer function and its bias offsets has been demonstrated experimentally [9].

The schematic for this demonstration this technique is shown in Fig. 21. In the experiment, the optical pulses were

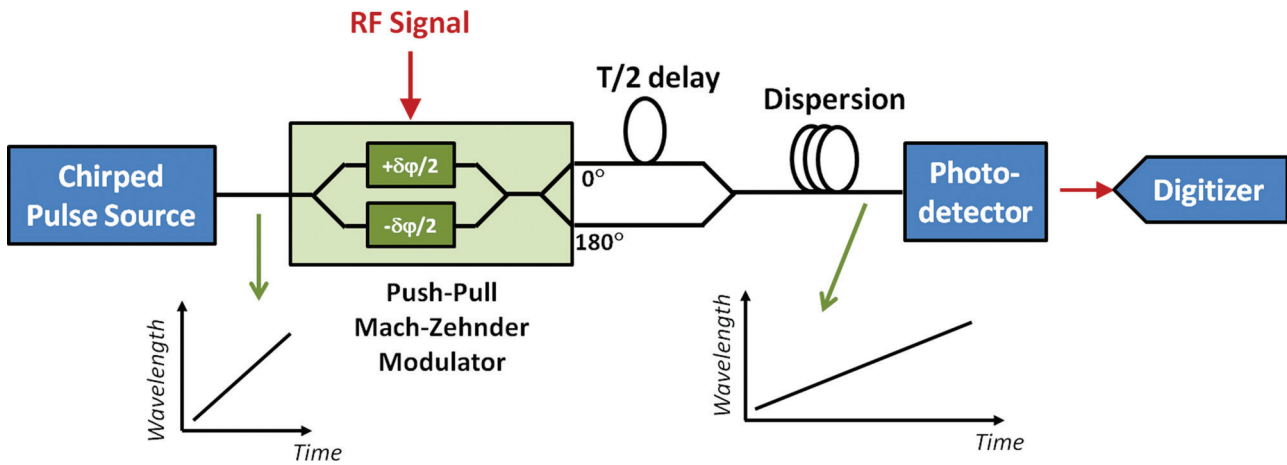


Figure 21 (online color at: www.lpr-journal.org) TSADC experimental setup employing a push-pull Mach-Zehnder modulator (MZM) for differential operation. The two outputs of the MZM are time-division multiplexed onto the same fiber to simplify the experimental demonstration. DSP: Digital signal processing.

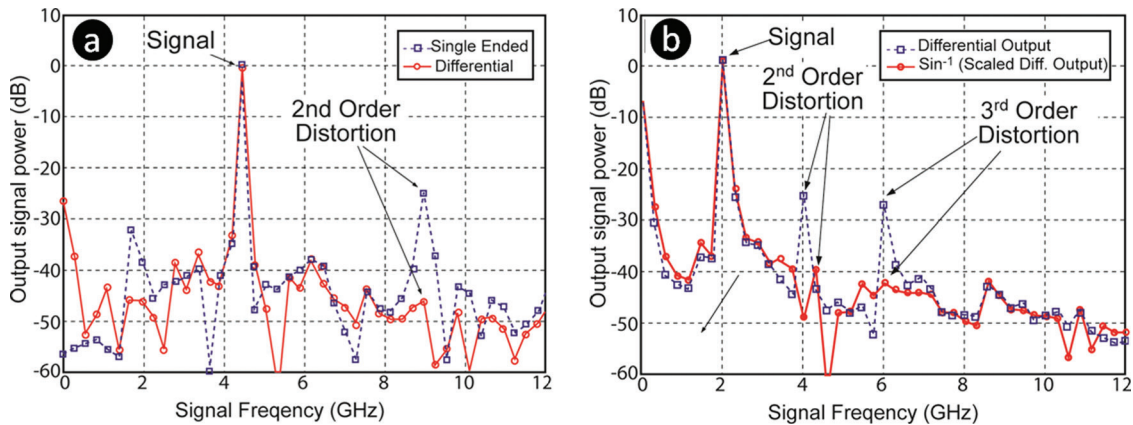


Figure 22 (online color at: www.lpr-journal.org) Spectra of RF signal captured by TSADC. (a) A 4.5-GHz RF signal is applied to the time-stretch analog-to-digital converter (TSADC). The 2nd-order dispersion-induced distortion (at 9-GHz) is completely suppressed by differential operation. (b) A 2-GHz RF signal is applied to the TSADC. Even with differential operation, Mach-Zehnder modulator (MZM) induces 2nd- and 3rd- order distortions due to bias offset and MZM transfer function. These distortions are suppressed by arcsine operation. © 2007 IEEE. Reprinted, with permission, from [36].

modulated with an RF signal at 4.5 GHz. The amount of dispersion was chosen to be such that the dispersion effects were quantitatively similar to an analog optical link with 15.5-km standard single mode fiber (SSMF) and also, the stretch factor was ~ 7.5 . The modulation index, m , was set to a high value of ~ 0.85 to obtain prominent harmonic distortion tone. Differential operation suppresses the dispersion-induced penalty as shown in Fig. 22(a). In the second experiment, a 2-GHz RF tone was used and a strong MZM bias offset was intentionally added [Fig 22(b)]. The arcsine operation was shown to suppress the 2nd- and 3rd- order distortion tones added due to MZM bias offset and MZM sinusoidal transfer function, respectively.

Even though these results are promising, for a wide-bandwidth and very-large-dynamic-range TSADC, the dispersion-induced 3rd-order distortion becomes important and cannot be ignored. Additionally, in the push-pull MZM configuration, the signal frequency has to be lower than

the dispersion null frequency. Hence, the back-propagation algorithm described in the next section becomes important under these circumstances.

4.2.2. Optical back-propagation algorithm

The optical back-propagation algorithm [44] (also described in Section 3) becomes important for wideband operation. This technique uses the two time-stretched output intensity measurements from the two outputs of a phase-diverse MZM to reconstruct the transmitted signal. Even in the presence of bias offsets, the signal can be recovered using this approach, as the bias offsets can typically be filtered out as the slow-varying components of the recovered signal. Figure 23 shows the results obtained from these intensity measurements [65]. As evident from the results, the algorithm is able to recover the signal for the two-tone input and suppress the nonlinear distortion by up to 26 dB. Use

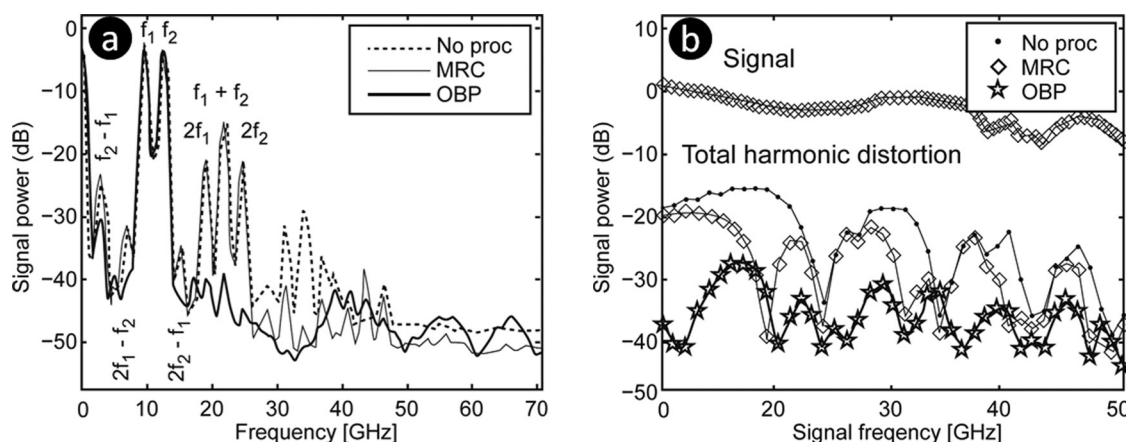


Figure 23 (a) Two-tone RF power spectrum (x-axis in both plots shows pre-stretch frequencies with resolution bandwidth of 1 GHz). (b) Signal and 3rd harmonic distortion for single-tone frequency sweep tests. The optical back-propagation technique is able to recover the signal and to suppress the nonlinear distortions. © 2007 IEEE. Reprinted, with permission, from [65].

of maximal ratio combining (MRC) algorithm, which is meant for obtaining signal from the phase-diverse channels (without attempting to correct for nonlinear distortion), is able to suppress the nonlinear distortion by only 3 dB. The main requirement for this algorithm is the use of a strictly single-electrode MZM (with chirp factor of ± 1). However, it was found that the chirp factor in the Z-cut LiNbO₃ MZM used in the experiment was about ± 0.7 . Hence, the results shown here can be further improved by increasing the chirp factor.

The two techniques discussed above can be very useful in overcoming nonlinear distortion in the TSADC. The back-propagation technique is very useful in removing the nonlinear distortion as well as in overcoming the dispersion penalty to achieve ultra-wide bandwidth operation. However, the waveforms from the two phase-diverse outputs are not symmetric. Therefore, the 2nd-order distortion and other common mode error components due to the photo-receivers and other electronic components cannot be canceled using this approach. Also, for the same input signal level, the back-end digitizer full-scale range needs to be 3 dB higher because of possible power imbalance between the two phase-diverse channels.

The use of differential operation can help. However, the involved arcsine operation requires capturing both the input signal and its intermodulation spectrum. The measurement bandwidth will then need to be three times larger than the input signal's bandwidth, which is clearly undesirable. To solve this problem, a broadband linearization technique has been developed. This technique, described in the next section, is intended for improving the 3rd-order nonlinear distortion without requiring excess bandwidth.

4.2.3. Broadband linearization technique

The availability of digital signal processors (DSP) and field-programmable gate arrays (FPGA) enable one to perform real-time digital processing of captured data in real time. In

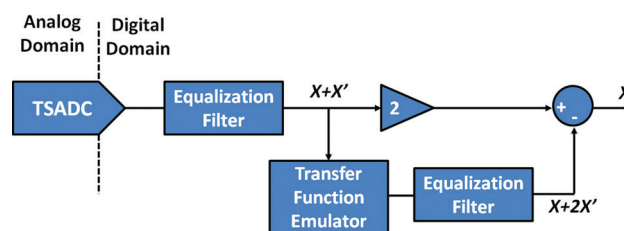


Figure 24 (online color at: www.lpr-journal.org) Block diagram of the broadband linearization technique for distortion suppression of TSADC. Equalization filters compensate for frequency dependence caused by dispersion in the dispersive fiber. The first compensates the frequency dependence of the physical link (dispersive fiber) and the second that of the virtual (digital) propagation modeled by the transfer function emulator. The emulator is a numerical model of the optical signal propagation through the dispersive link. This linearization technique works with time-domain representation of the RF signal; it is hardware friendly meaning that its digital implementation is computationally efficient. In principle, this technique can be also used for linearization of any nonlinear system.

this technique, a post-compensation algorithm, illustrated in Fig. 24, removes both the dispersion penalty and the 3rd-order distortion produced by electro-optic modulator, and the 2nd-order distortion produced by the interplay of the EO modulator's transfer function and dispersion. The digitized signal is linearly equalized and scaled using a linear equalization filter to obtain the original signal and its distortion $X(t) + X'(t)$. This enters an algorithm which emulates the transfer function of the physical nonlinear system including the dispersion induced frequency response and the modulator's nonlinear transfer function. As a result, under the assumption that the distortion component $X'(t)$ was small compared to the original signal $X(t)$ so that the higher order $X''(t)$ term is negligible, the obtained signal is approximately equal to $X(t) + 2X'(t)$ as shown in Fig. 24.

Another copy of the signal plus its distortion ($X(t) + X'(t)$) is doubled in amplitude, and the signal obtained from previous steps (transfer function emulator followed by equalizer and scaler) is subtracted from it. The resultant signal is the estimation of the original signal $X(t)$.

As discussed earlier, in terms of nonlinear distortions, the TSADC behaves in the same way as an analog optical link and has a well-defined transfer function [25, 44, 65]. Thus, to digitally generate the nonlinear distortions with memory effect, an analog optical link model introduced in [44, 65] has been used. In this model, a continuous-wave optical signal is modulated with an RF signal through the electro-optic modulator and then, propagated through the dispersive fiber, in digital domain. Since all calculations in this model were performed in the chirp-free equivalent domain (CW optical analog link), the number of numerical sampling points reduces by several orders of magnitude compared to a full optical bandwidth back-propagation method. In the TSADC, the optical power is generally low enough that the optical nonlinearity is not significant.

In order to evaluate the performance of the broadband linearization technique [45], it has been compared with the conventional memory-less correction technique, i.e. the arcsine operation that has previously been discussed in the previous section (also in [36]). A two-tone signal with fundamental frequencies 8.2 GHz and 10.25 GHz was sent to TSADC. The RF signal power was increased to achieve a modulation index of ~ 0.5 , resulting in significant nonlinear distortions by the MZ modulator. The 3rd-order intermodulation distortions appear at 6.15 GHz and 12.3 GHz as shown in Fig. 25(a). Prior to performing the corrections for nonlinear distortions, corrections for 2nd-order distortions due to bias offset of the Mach-Zehnder modulator and time warps were performed using the techniques introduced in Section 6 (also in [9]). The digitized signal provided by TSADC undergoes the conventional arcsine operation [Fig. 25(b)] and the broadband linearization technique [Fig. 25(c)] for comparison [45]. As can be seen in Fig. 25(a), nonlinear distortions over 15-GHz bandwidth could be as high as -30 dB without any correction for nonlinear distortions, and can be reduced to -35 dB with arcsine operation. This is a useful but modest improvement. In comparison, as shown in Fig. 25(c), the broadband linearization technique suppresses nonlinear distortions to below -50 dB. This represents > 15 dB better performance than the arcsine linearization under the same conditions. This means an improvement of ~ 2.5 bits in terms of the ADC resolution.

5. Impact of optical nonlinearity on performance of TSADC

Dispersion compensating fiber (DCF) provides a large dispersion-to-loss ratio (150–300 ps/nm per dB) with small phase distortion over a wide optical bandwidth and is ideal

for pre-chirping and time-stretching in the TSADC. Generally, it is desirable to increase the optical power to improve the performance of TSADC. The signal-to-noise ratio can be improved by increasing the optical power. In addition, for continuous-time operation, the TSADC uses multiple parallel wavelength channels and digitizers to time-interleave the time-stretched segments of the RF signal [25, 61]. When multiple wavelength channels are employed, intensity-modulated optical pulses with high peak power are required. However, when high-power pulses propagate inside the dispersive fiber, both optical nonlinearity and dispersion influence the shape and spectrum of the pulses. This leads to amplitude distortions and can degrade the signal-to-noise-and-distortion ratio (SNDR) and the ENOB of the TSADC. In such cases, optical propagation deviates from the linear regime, and it becomes imperative to consider effects of optical nonlinearity on the time stretch process. In this section, we review the impact of the most important optical nonlinearity in fiber, namely the Kerr effect, on the performance of TSADC.

5.1. Optical nonlinearity in TSADC

The basic equation that governs the propagation of optical pulses in the presence of dispersion and weak optical nonlinearity is the nonlinear Schrödinger equation (NLSE):

$$\frac{\partial A}{\partial z} + \frac{i\beta_2}{2} \frac{\partial^2 A}{\partial t^2} = -\frac{\alpha}{2} A + i\gamma |A|^2 A, \quad (5.1)$$

where α is the attenuation constant, β_2 is the GVD parameter (the second derivative with respect to angular frequency of the modal wave number), γ is the nonlinear coefficient related to the nonlinear index n_2 by $\gamma = (n_2 \omega_0) / (c A_{eff})$, and A_{eff} is the effective mode area of the fiber [30]. A in (5.1) is the slowly varying envelope proportional to the optical field. Equation (5.1) has been successful in explaining a large number of nonlinear effects, e.g., self-phase modulation and four-wave mixing, which are the main causes of nonlinear optical distortions in the TSADC. The split-step Fourier method is commonly employed to solve the NLSE numerically, obtaining an approximate solution by assuming that the dispersive and nonlinear effects act independently over a very small length of fiber [30]. It has been also found that the local-error method algorithm [49] reduces the computation time for split-step calculations, and offers a significant improvement in the context of TSADC, where a broad time window and fine time resolution are needed.

The impact of optical nonlinearity is particularly important in the time stretch (second dispersive) fiber after the intensity modulator because it is here that the nonlinearity affects the RF signal. In order to significantly reduce the number of sample points and simulation run-time, a single broadband optical pulse propagating through the TSADC has been evaluated in each simulation [76].

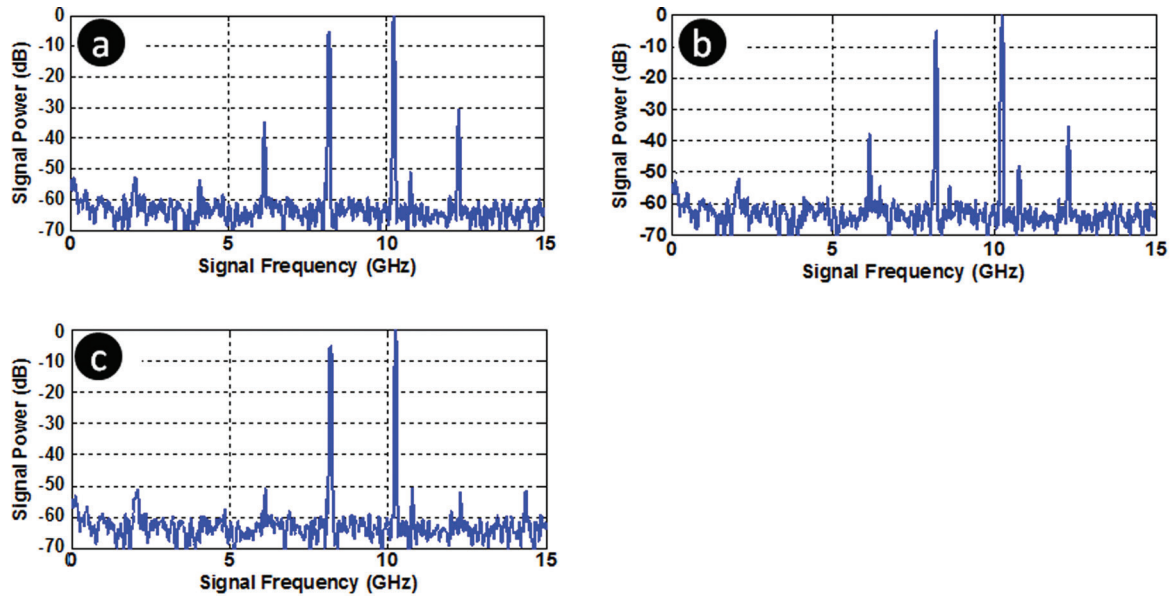


Figure 25 (online color at: www.lpr-journal.org) Measured spectrum in two-tone test ($f_1 = 8.2$ GHz, $f_2 = 10.25$ GHz), (a) before linearization, (b) after conventional Arcsine operation, showing incomplete cancellation of intermodulation distortion, (c) after linearization with the new broadband linearization algorithm. The data shows the superior performance of the new algorithm compared to the conventional arcsine linearization. This is because the Arcsine technique is unable to account for the system's frequency dependencies (memory effect) whereas our algorithm has this capability. The algorithm shows drastic improvement of intermodulation distortions ($2f_1 - f_2 = 6.15$ GHz and $2f_2 - f_1 = 12.3$ GHz) over conventional arcsine operation.

In an effort to explain the effect of optical nonlinearity, an analytical model for the un-modulated chirped pulse envelope was developed in [76] and this helps to qualitatively explain the results shown in the next section. The model begins with an un-chirped Gaussian pulse (pulse width T_0 and power P_0) that propagates linearly through the first dispersive fiber with length L_1 and GVD parameter β_2 . In the linear propagation regime, the dispersed pulse envelope is:

$$A_c(z, t) = \sqrt{\frac{P_0 T_0}{T(z)}} e^{i\varphi(z, t)} e^{-t^2/T^2(z)}, \quad (5.2)$$

where

$$T(z) = T_0 \sqrt{1 + (z/L_D)^2},$$

$$\varphi(z, t) = \varphi_L(z, t) \quad (z < L_1),$$

$$\varphi_L(z, t) = \frac{-(z/L_D)t^2}{2T^2(z)} + \frac{1}{2} \tan^{-1}(z/L_D), \quad (5.3)$$

where L_D is the dispersion length and related to GVD parameter by $L_D = |T_0^2 \beta_2^{-1}|$, t is time, and z is propagation distance [30]. The model then adds a nonlinear phase term to this solution to include optical nonlinearity. If the nonlinearity is weak enough, the pulse maintains its shape [30] and its envelope maintains a (dispersed) Gaussian profile with a phase that starts to accumulate after the first disper-

sive fiber:

$$\varphi(z, t) = \varphi_L(z, t) + \varphi_{NL}(z, t) \quad (z > L_1),$$

$$\varphi_{NL}(z, t) = \int_{L_1}^z \gamma |A_c(z', t)|^2 dz'. \quad (5.4)$$

Note that the model includes the linear phase accumulated over both fibers, while the nonlinear phase is only added in the second fiber. This model is based on [77], except that the drop in optical peak power due to dispersion was neglected previously. As opposed to the split-step Fourier method, this analytical model does not take into account the modified dispersion of the nonlinearly-generated frequencies.

A subtle issue in calculating φ_{NL} is that different instants on the optical pulse travel at different speeds, carrying the nonlinear phase with them. The nonlinear phase at any instant along the envelope is then the total nonlinear phase accumulated by that portion of field throughout the fiber. The split-step Fourier method applies the dispersion to the field in the frequency domain as the nonlinear phase is accumulated during propagation, which carries the nonlinear phase with the frequency components automatically; but in the analytical model, it must be explicitly ensured that the nonlinear phase factor is dispersed along with the pulse envelope. Fortunately, the dispersion causes each point of the optical pulse to remain the same number of pulse widths from the peak of the pulse as illustrated in Fig. 26. Note

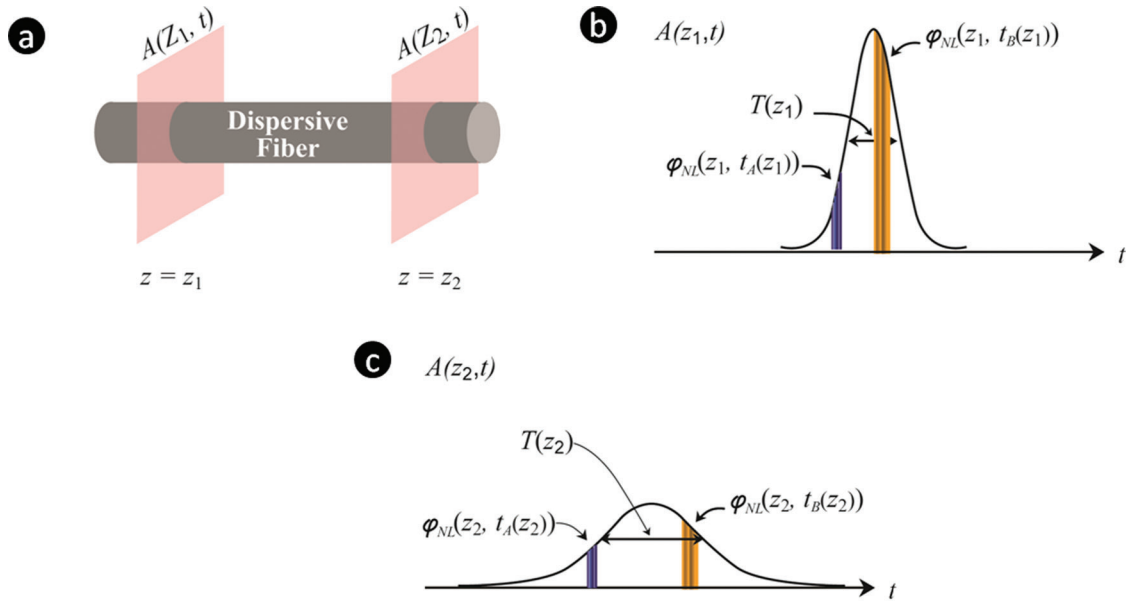


Figure 26 (online color at: www.lpr-journal.org) (a) A section of a typical optical fiber. $A(z_1, t)$ and $A(z_2, t)$ are the slowly varying envelopes of the optical field at distances z_1 and z_2 , respectively. (b) Optical field envelope before propagating through a short segment of dispersive fiber. (c) Dispersed optical field envelope after propagating through a short segment of dispersive fiber. © 2011 IEEE. Reprinted, with permission, from [76].

that this simplification occurs because the analytical model starts the nonlinear phase calculation with a chirped Gaussian pulse; arbitrary pulses do not in general satisfy this property. Thus, for each point along the optical pulse, the value in the Gaussian function is constant, and can be taken out of the integral,

$$\begin{aligned} \phi_{NL}(z, t) &= \gamma P_0 e^{-t^2/T^2(z)} \int_{L_1}^z \frac{dz'}{\sqrt{1 + (z'/L_D)^2}} \\ &= \phi_{NL}^{\text{peak}}(z) e^{-t^2/T^2(z)}. \end{aligned} \quad (5.5)$$

Upon taking the limit of no dispersion ($L_D \rightarrow \infty$; equivalent to ignoring the drop in optical power), (5.5) reproduces the result found in [30, 77], (cf. (4.1.5) and (3.4), respectively):

$$\phi_{NL}(z, t) = \gamma P_0 (z - L_1) e^{-t^2/T^2(z)}. \quad (5.6)$$

By substituting the stretch factor $S = (L_1 + L_2)/L_1$ (the amount by which the electrical pulse is effectively stretched in time), the nonlinear length $L_{NL} = (P_0 \gamma)^{-1}$, and the dispersion length L_D into (5.5), the peak nonlinear phase shift (5.5) after L_1 and L_2 can be obtained,

$$\phi_{NL}^{\text{peak}} = \left(\frac{L_D}{L_{NL}} \right) \left[\sinh^{-1} \left(\frac{SL_1}{L_D} \right) - \sinh^{-1} \left(\frac{L_1}{L_D} \right) \right], \quad (5.7)$$

If $L_1 L_D^{-1} > 2$ and $S > 1$, both of which hold for the TSADC system, then (5.7) can be very well approximated

with a logarithm. In terms of system variables,

$$\phi_{NL}^{\text{peak}} \approx \left(\frac{L_D}{L_{NL}} \right) \ln(S) = \frac{\gamma P_1 T_A}{\Delta \lambda |D|} \ln(S), \quad (5.8)$$

where P_1 is the optical peak power after L_1 and $D = -2\pi c \beta_2 \lambda^{-2}$ is the GVD parameter in wavelength units. Note that this value is not independent of the fiber lengths, as

$$L_1 = T_A / (\Delta \lambda D); L_2 = L_1 (S - 1). \quad (5.9)$$

Numerically, this approximation shows an excellent agreement with the split-step Fourier simulations in the absence of RF modulation. The error of the analytical approximation relative to the split-step solution, given by

$$\begin{aligned} \text{error} &= \sqrt{\frac{\int_{-\infty}^{+\infty} |A_{SSFM}(L_1 + L_2, t) - A_c(L_1 + L_2, t)|^2 dt}{\int_{-\infty}^{+\infty} |A_{SSFM}(L_1 + L_2, t)|^2 dt}}, \end{aligned} \quad (5.10)$$

was found to be less than 0.01% along the entire length of propagation for P_1 up to 300 mW, where A_{SSFM} is the optical envelope as calculated by the split-step Fourier method. If one ignores the nonlinearity in the analytical approximation, the error exceeds 30% even at P_1 of 100 mW. Therefore optical nonlinearity is significant for the conditions considered, and the analytical approximation does properly account for it. Other analytical approximations, such as the variational method [78] and moment method

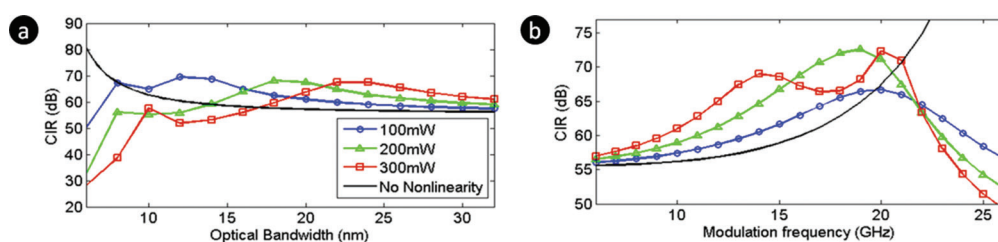


Figure 27 (online color at: www.lpr-journal.org) (a) Carrier-to-interference ratio (CIR) of the TSADC versus optical bandwidth for different optical powers. CIR is defined as the ratio of the amplitude of the fundamental tone to that of the 3rd-order harmonic. (b) CIR of the TSADC versus the frequency of the RF signal for different optical powers with constant optical bandwidth (32 nm). © 2011 IEEE. Reprinted, with permission, from [76].

[30], were compared with the split-step Fourier method as well, but were found to be in worse agreement. This is because this model finds the time dependence of the nonlinear phase while other methods include the phase through extra parameters (e.g., chirp) in a fixed functional form.

Equation (5.8) shows that the effect of nonlinearity increases with optical power and stretch factor. Interestingly, the logarithmic term indicates that the nonlinearity does not increase quickly with stretch factor. This can be understood by considering that when the pulse is stretched further, the peak power is decreased and nonlinearity is weaker. In other words, one should safely be able to scale the stretch factor without any excessive optical nonlinearity.

Note that in each of our simulations the local-error method chose the step size to maintain a constant change of φ_{NL}^{peak} per step. Intuitively, the error in each step depends on the amount by which the nonlinear and linear operators in the NLSE do not commute, which is dependent on the change in nonlinear phase.

5.2. Impact of optical nonlinearity on the performance

The TSADC configuration used in [76] to numerically evaluate the performance exploits a pre-chirped broadband optical pulse (variable optical bandwidth from 5 nm to 32 nm) and modulates the RF signal onto the pulse using a dual-output push-pull Mach-Zehnder modulator. Then the two complementary outputs of the modulator propagate through the dispersive fibers [lossless with dispersion parameter (D) of $-100 \text{ ps}\cdot\text{nm}^{-1}\text{km}^{-1}$ and nonlinear coefficient of $5 \text{ W}^{-1}\text{km}^{-1}$]. The first dispersive fiber for pre-chirping and the second dispersive fiber for time-stretching are set to provide a stretch factor of 20, while the total time aperture is kept below 10 ns [see (5.9)].

The sinusoidal transfer function of the Mach-Zehnder modulator followed by GVD generates the RF signal sidebands and their harmonics as discussed in Section 4. In that section, many techniques have been discussed to mitigate and/or cancel out these harmonic distortions (also in [36, 45, 65]). It has been shown that the differential operation utilizing the complementary Mach-Zehnder outputs is able to cancel out the even-order (2nd, 4th, etc.) distortions.

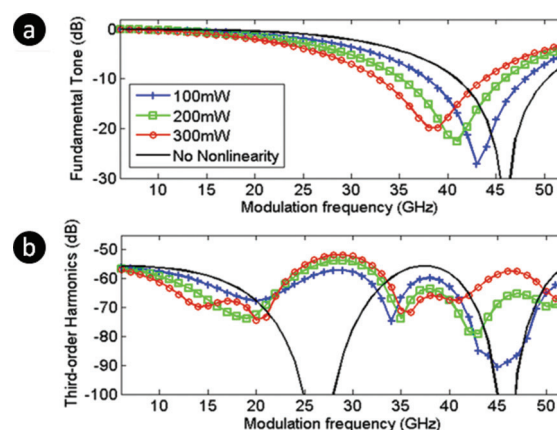


Figure 28 (online color at: www.lpr-journal.org) Single-tone dispersion penalty of the (a) fundamental tone and the (b) 3rd-order harmonic distortion for different optical powers with constant optical bandwidth (32 nm). The dispersion penalty was extracted for a single-tone RF signal sent to the TSADC. The bandwidth limitation imposed by the dispersion penalty becomes more severe at high optical powers. © 2011 IEEE. Reprinted, with permission, from [76].

However, odd-order distortion cannot be fully eliminated because the frequency-dependent phase shift, caused by GVD, changes the effective transfer function of the electro-optic modulation process. The strongest odd order distortion that limits the performance is the 3rd-order term. The carrier-to-interference ratio in the TSADC is defined as the ratio of the fundamental tone to the 3rd-order harmonic. Figure 27(a) shows the carrier-to-interference ratio versus optical bandwidth of the source for different optical powers (peak power at the beginning of the second dispersive fiber), while the frequency of the RF signal is kept constant. At large optical bandwidths, the nonlinear phase shift is small [see also (5.8)] because the optical pulse disperses faster in the second dispersive fiber. This is manifested in Fig. 28(a) in the convergence of carrier-to-interference ratio for different optical power levels at large optical bandwidths. However, since the optical peak power drops slowly at lower optical bandwidth, the nonlinearity can greatly degrade the carrier-to-interference ratio in the narrowband regime. Figure 27(b) illustrates the carrier-to-interference ratio

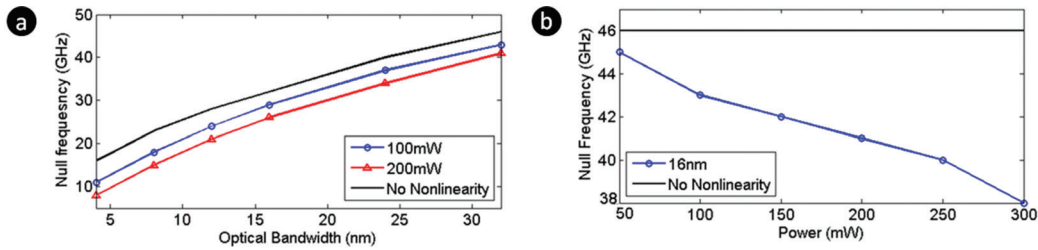


Figure 29 (online color at: www.lpr-journal.org) Single-tone dispersion null frequency versus (a) optical bandwidth for different optical powers and (b) optical power for constant optical bandwidth (16 nm). The null frequency moves higher for larger optical bandwidths and to lower frequencies for higher optical powers. © 2011 IEEE. Reprinted, with permission, from [76].

versus the frequency of the RF signal for different optical power levels while the optical bandwidth of the optical source is constant (32 nm). The carrier-to-interference ratio improves at low modulation frequencies due to the suppression of the 3rd-order harmonic (see also Fig. 28). However, optical nonlinearity can greatly degrade the carrier-to-interference ratio at high modulation frequencies, limiting the effective number of bits at those frequencies.

The dispersion penalty (see Section 3) for the fundamental tone and 3rd-order harmonic distortion is illustrated in Fig. 28(a)–(b), respectively. The dispersion penalty exists in the linear-optical regime; however, nonlinearity causes a shift in the dispersion-penalty null frequency. This shift can be explained by the analytical approximation developed in the previous section. Since the carrier of the optical pulses is the strongest component, it has the largest influence on the nonlinearity. Therefore, (5.2) still holds for the carrier even in the presence of RF signal sidebands. The nonlinear phase factor adds with the linear phase in (5.4) and so shifts the dispersion null in Fig. 28(a). In other words, larger GVD is required for a given RF bandwidth and stretch factor at high optical power levels. Interestingly, we found that if the GVD is anomalous, the dispersion penalty is shifted in the opposite direction; however, use of anomalous GVD fiber is not desirable due to lower dispersion-to-loss ratio and possible occurrence of modulation instability, which would significantly distort the RF signal. It should be noted that the shift of the dispersion penalty null at high optical power has been also experimentally observed and reported in [79].

A set of simulations was performed to understand the behavior of the dispersion null frequency versus optical bandwidth and optical power. As illustrated in Fig. 29(a)–(b), the null frequency goes to higher frequencies for larger optical bandwidths and to lower frequencies for higher optical powers, which is due to the dependence of nonlinear phase shift on optical bandwidth and power, as expected from (5.8).

6. Time warp distortion correction and calibration

Distortions due to non-uniform intensity envelope in chirped pulses, nonlinearity due to Mach-Zehnder modulator’s (MZM’s) transfer function and dispersion effects,

and the laser RIN effects reduce the dynamic range of the TSADC. These effects are mitigated using differential and arcsine operations and other post processing techniques described in section 4. However, the signal still suffers from another type of distortion that is caused by non-uniformities of the stretched time scale. These distortions are caused by non-uniform stretching (in time) across the optical spectrum and the channel-to-channel timing offsets in the multi-channel or continuous-mode TSADC. The resulting effect is best described as “time warp” distortion. In addition, wavelength dependent bias offsets in the MZM become significant for wider optical bandwidths that are required for continuous operation, leading to rapidly varying 2nd-order distortion with wavelength (or time). The following subsections describe these effects and the techniques developed to remove the distortions, leading to digitization of signals with 10-GHz bandwidth and 7.2-ENOB resolution.

6.1. Time warp distortion and its mitigation

The effect of time warp caused by non-uniformity in the stretch factor across the optical spectrum is illustrated by Fig. 30. The time stretch, or equivalently the bandwidth compression factor is given by $S = (D_2 + D_1)/D_1$, where D_1

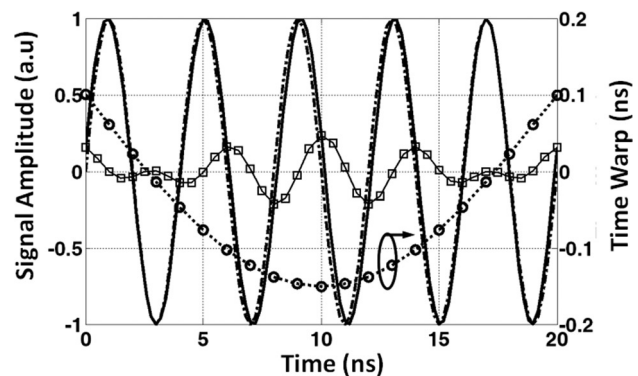


Figure 30 Solid trace shows an ideal signal without time warp; dashed trace is a signal with time-warp; trace with squares represents the error; trace with circles represents amplitude of the time warp.

and D_2 are the dispersion values of the first (used to create the chirped optical carrier) and second (used for time stretching) dispersion compensating fibers [25]. These dispersion values are wavelength dependent but their ratio, and hence S , are wavelength independent, if the two fibers have matching dispersion coefficients $\beta_2, \beta_3, \beta_4$, etc. However, finite mismatches in dispersion coefficients between the two fibers cause the stretch factor to be wavelength dependent (and hence, time dependent by virtue of wavelength-to-time mapping), which culminates in the time warp. Wavelength division multiplexing/demultiplexing (WDM) filters have wavelength dependent group delay variations [80] and result in additional time warps. Fortunately, their contribution to the distortion is reduced by the stretch factor if placed after the MZM, in the same way as time stretching helps in reducing noise due to electronic clock jitter.

Optical nonlinearity in the fiber can be yet another source of time-warp distortion. The ultra-fast optical pulses originating from the mode-locked laser initially have very high peak power (in the first DCF stage), which can result in self-phase modulation (SPM) due to optical Kerr non-linearity [30]. If present, SPM combined with GVD can distort the desired linear wavelength-time mapping and result in time warps. Another source of time warp is timing skew between adjacent WDM channels that are combined to create continuous-time operation. Even though this can be removed to some extent in hardware by adjusting electronic clocks and delays using feedback, some residual skews remain, which effectively appear as sharp time warps at channel boundaries, as evident from Fig. 31.

The time warp due to all these effects is essentially static over time and can be corrected by calibration. In order to measure the time warps and obtain the necessary calibration data, a sinusoidal RF tone is stretched using a few hundred optical pulses and captured by slow ADCs. The waveforms from adjacent WDM channels are coarsely aligned in time and concatenated [9]. A sinusoidal curve fit is then performed and the difference between the measured waveforms' and ideal sine-fit curves' zero crossings

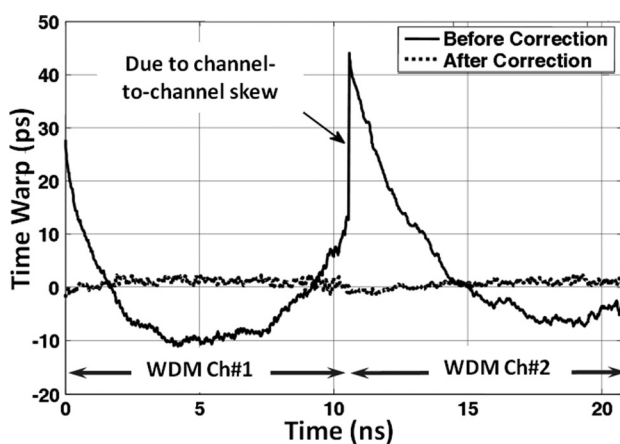


Figure 31 Time warp magnitudes before and after correction along the time axis of two combined WDM channels. © 2008 IEEE. Reprinted, with permission, from [81].

(averaged over these waveforms) is obtained (Fig. 31). The sharp jump in the center shows timing skew between sinusoids from the adjacent WDM channels. These data are used to correct the time warp in unknown arbitrary signals by performing 2nd-order polynomial interpolation. Once the averaged time warp data is obtained, interpolation can easily be performed in real time using a dedicated digital signal processor.

6.2. Removal of distortion due to wavelength-dependent bias offsets

Even after the correction of time warp distortion, the signal still has a 2nd-order distortion due to the wavelength dependence of the MZM bias offset [46]. In TSADC, because the optical carrier entering the MZM is chirped, this 2nd-order distortion is time dependent. This effect becomes significant when wide optical bandwidths are employed but can be reduced, to some extent, with the arcsine operation itself [36]. The 2nd-order nonlinearity generates a contribution to the DC term in the photo-current. However, estimating the bias offset from DC terms is difficult as there are other unknown DC offsets added by the electronics.

To overcome these problems and correct for nonlinearity due to MZM bias offsets, the same sine-fitting technique is used as for time warp correction. However, in this case, the amplitude of the 2nd-order harmonic component (for a certain wavelength) is proportional to the average quantity obtained by adding the timing offsets in zero crossings of positive edges and subtracting that of the negative edges - when compared to those of an ideal sinusoid. As shown in Fig. 32 and as expected from the wavelength dependence of MZM bias offset, it is found that 2nd-order harmonic amplitude $\delta(t)$ varies linearly with the wavelength. Once

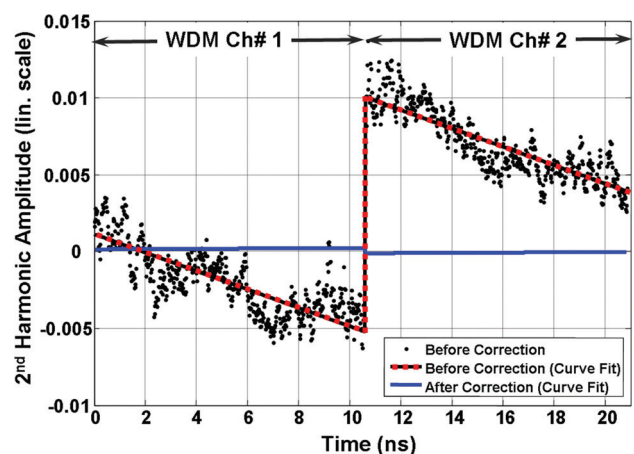


Figure 32 (online color at: www.lpr-journal.org) Measured second harmonic amplitude versus time/wavelength due to wavelength-dependent bias offsets in the Mach-Zehnder modulator. After correction in the digital post processing, the distortion is almost entirely suppressed. © 2008 IEEE. Reprinted, with permission, from [81].

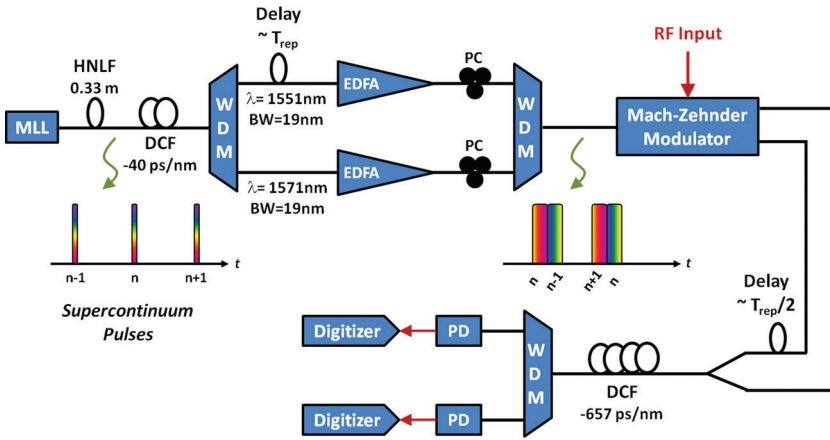


Figure 33 (online color at: www.lpr-journal.org) Experimental setup of the system used for demonstration of the 7-ENOB 2-channel time stretch ADC with 10-GHz bandwidth.

$\delta(t)$ is measured, the linearized signal $y(t)$ is obtained from the uncorrected signal $x(t)$ as,

$$y(t) = x(t) - \delta(t) \cdot (2x^2(t) - 1) \quad (6.1)$$

For example, an RF signal, $\cos(\omega t)$, with time-dependent 2nd-order harmonic amplitude given by $\delta(t)$, takes the form $x(t) = [\cos(\omega t) + \delta(t) \cdot \cos(2\omega t)]$. Equation (6.1) gives $y(t) = [\cos(\omega t) + 2\text{nd order terms in } \delta(t)]$. Since $\delta(t)$ is small, the $\delta^2(t)$ terms become negligible and hence, the original signal $y(t) \approx \cos(\omega t)$ is obtained.

6.3. Demonstration of 7-ENOB 2-channel 10-GHz bandwidth and scaling towards continuous-time operation

The algorithms mentioned in the previous sections are used to capture wideband signals with high resolution [9]. Figure 33 shows the experimental setup of the TSADC used for this purpose. Optical pulses from the MLL are sent through a long highly non-linear fiber (HNLf). These pulses are stretched in the first dispersive fiber with a dispersion value of -40 ps/nm to obtain chirped pulses. Broadband pulses are carved out from them using standard telecommunication 19-nm bandwidth filters at 1551-nm and 1571-nm wavelengths, and amplified using C-band and L-band band EDFAs, respectively.

In addition to amplification, the 1551-nm channel pulses are delayed, so that the trailing edge of the n -th pulse in the L-band slightly overlaps with the leading edge of the $(n-1)$ th pulse in the C-band. This ensures continuity of the RF signal between adjacent WDM channels. The overlapping L-band and C-band pulses are derived from separate laser pulses to demonstrate seamless combination of the time-stretched signals from adjacent pulses, as required in a fully continuous operation. Polarization controllers after the EDFAs in two WDM channels independently correct for their polarizations, before combining the optical pulses in

the second CWDM filter, which is followed by the intensity modulator.

The RF signal differentially modulates the optical pulses using dual-output push-pull MZM [36]. For ease of implementation and to minimize the mismatch, the two MZM outputs are relatively skewed in time and multiplexed onto the second dispersive fiber with a dispersion value of -657 ps/nm, achieving a stretch factor of ~ 17 . The WDM channels at the dispersive fiber output are demultiplexed and detected using photo-receivers (with ~ 0.5 mW average input optical power). The obtained RF signal is digitized by a conventional electronic digitizer (Tektronix DPO71604), and further signal processing is performed on a computer. Single and two-tone tests were performed with signal frequencies varying from 4 GHz to 16 GHz and modulation depth of ~ 0.7 and ~ 0.5 , respectively. The time warps were found to be almost constant, whereas channel-to-channel timing skews had a slow variation with time.

For any signal, calibration data obtained from first half of the captured waveforms (365 pulses in 10 μ s) were applied for correcting distortions in the remaining 365 pulses. For these pulses, 10-GHz noise bandwidth gave 7.05–7.25 ENOB on an average (obtained by sine curve fitting). For two-tone tests, signal power was reduced by 3 dB to avoid clipping, resulting in about 6.5–6.7 ENOBs (or effectively 7.0–7.2 ENOBs when referred to the full-scale signal power). High time-bandwidth product was achieved by concatenating 30 time segments synchronously, giving an SFDR of 52 dB, as evident from Fig. 34. This experiment demonstrates the ability of the TSADC to scale to continuous-time operation. The measured SNR was limited primarily by the back-end digitizer. In these experiments, the digitizer's bandwidth was reduced to 1 GHz to maximize its ENOB, but nevertheless, the maximum ENOB it could deliver was 7.2 [9]. Higher resolution (> 8 -ENOB) employing the photonic time-stretch pre-processor has also been recently demonstrated by Ng et al. [82]. The SFDR measurement for a high-speed photonic time-stretch A/D converter has been performed by Gee et al. in Ref. [83].

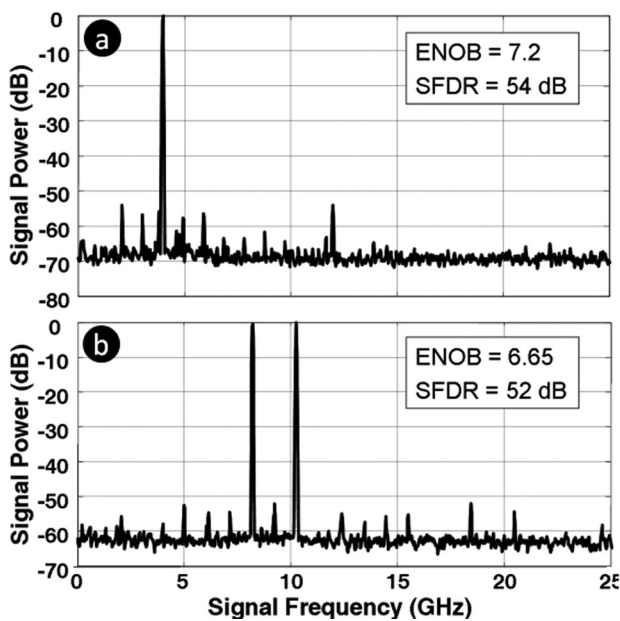


Figure 34 RF signal spectrum for (a) a single-tone test with 4-GHz RF input; (b) a two-tone test with 8.2-GHz & 10.25-GHz RF inputs. In both plots, 30 waveforms are stitched coherently to achieve high-resolution bandwidth and to show scalability to continuous time operation. The SFDR in both cases is in excess of 50 dB over a 10-GHz input (pre-stretch) noise bandwidth. © 2008 IEEE. Reprinted, with permission, from [81].

7. Power scaling in TSADC

While faster analog-to-digital converters are required for new applications, improving speeds also increases their power consumption with the effect more pronounced in high-speed ADCs. It, therefore, becomes important to consider power dissipation in such ADCs, which increases rapidly with frequency. The power scaling trend in electronic ADCs is discussed in this section, and it is shown that time-stretching can offer a significant reduction in the power consumption by reducing the speed at which the back-end digitizer must operate at.

Continued scaling of CMOS technology [84] has improved digital circuits tremendously in terms of performance, power efficiency, and cost. However, analog circuits (and ADCs) have not kept pace. Even though the bandwidth of an analog circuit improves with technology scaling, since smaller devices run faster thanks to reduced capacitances, power dissipation for the same functionality does not always scale because of lower intrinsic gain in shorter channel CMOS transistors [85]. In fact, most improvements in the power efficiency of analog circuits can be attributed to architectural improvements and scaled voltages, rather than to reduced capacitances in CMOS devices.

In electronic ADCs, analog full-scale voltage cannot be reduced arbitrarily because of thermal noise limitations. As a result, while technology scaling has not directly resulted in decreased analog power dissipation, the power reduction and increased speed of digital circuits have allowed

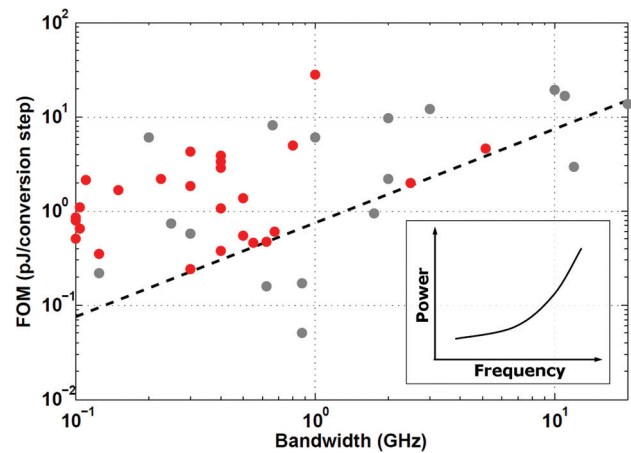


Figure 35 (online color at: www.lpr-journal.org) Energy per conversion step versus performance of state-of-the-art high-speed electronic analog-to-digital converters (2002 onwards). Red markers represent ADCs with >5-ENOB resolution and the dashed line corresponds to the estimated linear increase in FOM with frequency (the corresponding quadratic increase in power dissipation is shown in the inset).

extensive use of digital correction and calibration techniques in ADCs, which have led to improvements in performance. The most commonly used figure of merit (FOM) for ADC efficiency is the energy required per conversion step,

$$\text{FOM} = \frac{P_{\text{diss}}}{2^{\text{ENOB}} \times 2 \times \text{ERBW}}, \quad (7.1)$$

where P_{diss} is the power dissipation of the ADC, ENOB is the effective number of bits, and ERBW is the effective resolution bandwidth of the ADC [6]. ERBW is defined as the frequency at which the SNDR of the ADC degrades by 3 dB compared to its low-frequency value. For ADCs in which the ERBW is greater than the Nyquist bandwidth (i.e. Nyquist rate ADCs), ERBW is replaced by the Nyquist bandwidth in the above expression.

Figure 35 shows the energy per conversion step as a function of ERBW for ADCs demonstrated from 2002 to present. While Fig. 35 lumps together ADCs with different electronic technologies, it is evident from the plot that above 1 GHz, the energy per conversion step for the best ADCs increases rapidly with bandwidth. A similar trend is found from the data obtained in [86] for CMOS technologies for high speed (>1-GHz ERBW) and moderate to high-resolution (>5 ENOB) ADCs. In ref. [86], Murmann finds that the power efficiency of the ADCs has improved by a factor of 2 every two years, thanks to technology and power supply scaling. However, the data in [86] also confirms that this trend is not observed for high-speed ADCs with such a resolution.

We note that the power dissipation, as quantified by FOM, in such high-speed ADCs increases super-linearly with f_s for a constant resolution, where f_s is the Nyquist sampling frequency. Alternative technologies are becoming

important in reducing the power consumption. Photonics-based analog-to-digital converters have been mostly pursued for high-speed operations [12]. As is shown below, the photonic time-stretch pre-processor enables linear power scaling to very large frequencies and also breaks through the so-called walls in the ENOB-bandwidth tradeoff caused by comparator ambiguity and timing jitter in the ADCs [6, 7].

In this section, we first describe the fundamental limitations to noise and power dissipation in electronic ADCs. Second, we discuss frequency scaling in digital circuits and show why similar trends are observed in ADCs. Third, we show how the photonic time-stretch pre-processor can push the linear scaling of power dissipation versus sampling frequency in the ADCs well into the gigahertz band. Finally, we compare power dissipation trends in high-speed ADCs with and without the use of the photonic time-stretch pre-processor.

7.1. Fundamental limits to power dissipation in ADCs

As described in section 1, an electronic ADC consists of sample-and-hold (S&H) stage(s), quantization stage(s), clock generation circuitry, and reference buffers. Additionally, almost all modern ADCs make extensive use of digital post-processing circuitry for correction and calibration, in order to remove distortions caused by non-idealities and mismatches.

In the sample-and-hold stage, the analog signal and the thermal noise generated in the switch are sampled onto a capacitor with capacitance C . The sampled noise voltage has a mean squared value (variance) of kT/C , where k is the Boltzmann constant and T is the ambient temperature. Note that the total magnitude of the thermal noise is independent of the sampling frequency. This is because the thermal noise at all frequencies is folded back into the Nyquist bandwidth in a sampling system. If the thermal noise is the dominant noise source and V_{FS} is the full scale voltage, we obtain the signal-to-noise ratio and dissipated power as:

$$\text{SNR} \propto \frac{V_{FS}^2}{kT/C}, \quad P_{\text{diss}} \propto CV_{FS}^2 f_s \quad (7.2)$$

$$\Rightarrow P_{\text{diss}} \propto kT f_s \text{SNR} \quad (7.3)$$

Therefore, for a given signal power (V_{FS}), thermal noise (kT/C) places a lower limit on the capacitance that can be used in the sample-and-hold stage. On an average, bias currents required in the buffer amplifiers to charge the sampling capacitors with the signal, or the reference voltage, are directly proportional to the value of C and the charging time. This fundamentally limits the power dissipation of an ADC, a problem that can be quantified in terms of the ENOB by substituting the standard expression for SNR as

a function of ENOB [6, 87]:

$$P_{\text{diss}} \propto kT f_s 10^{(6.02 \times \text{ENOB} + 1.76)/10} \propto kT f_s \text{SNR} \quad (7.4)$$

In practical circuits, the power dissipation is at least 3 to 4 orders of magnitudes higher than this value [88], since the individual components such as voltage buffers, op-amps, comparators, and clock sources have to satisfy requirements of low noise and jitter, high linearity, high-speed and high-precision settling. Currents in all these circuits scale proportionally with the capacitance for a fixed sampling frequency.

Equation (7.4) also suggests that ADC power dissipation should scale linearly with f_s . However, from the trend seen in Fig. 35 and in [89], and from the discussion in the following sections, it becomes clear that in reality, the energy per conversion step scales roughly as f_s or higher powers of f_s , i.e., power dissipation scales super-linearly with f_s in high-speed ADCs. Observation of a similar trend has previously been reported for pipelined ADCs in [90].

7.2. Power scaling in digital circuits

Power dissipation in digital circuits, which until recently has been dominated by the dynamic power required for switching transistors is equal to $C \cdot V^2 \cdot f / 2$, where C is the average node capacitance, V is the supply voltage and f is the clock frequency [91]. To run the circuits at fast speeds, high switching currents are required to rapidly charge or discharge the node capacitances, which demand a higher supply voltage. The minimum operating voltage V at which a digital circuit can operate correctly is roughly proportional to $f^{1/2}$ for a wide range of frequencies or voltages [91]. This implies that if the frequency of operation is reduced by a factor α , the required power decreases by factor α^2 . As a result, the energy-delay product for performing an operation is roughly constant over a wide range of operating frequencies in digital circuits [91]. This simple observation implies that when more delay is allowed for a set of operations, less energy is required to perform them. This implication is the reason that the digital world is moving towards architectures exploiting parallelism [92], and the same trend is found in high-sample-rate ADCs and real-time digital oscilloscopes [89, 93–97]. The time-stretch technique, which uses the same approach of parallelism to digitize very high bandwidth signals, can also help in reducing power dissipation in high-speed ADCs.

7.3. Power scaling in electronic ADCs

In deriving (7.3), it was assumed that to increase the sampling frequency, the bias currents need to be increased linearly to charge up the sample and hold capacitors fast with no limitation being imposed by the transistor response time. In reality, the unity gain frequency f_T of the transistors will also place a limit because the operational amplifier

(op-amp) outputs that drive the capacitors must settle in a shorter time at higher frequencies.

Increasing the bias current in a CMOS transistor can be done in two ways. In the first method, the device size is kept constant and the bias current (I_D) is increased by increasing the overdrive voltage (V_{OD}). This increases the unity gain frequency $f_T \propto I_D^{1/2}$, as for a device with a fixed size, transconductance $g_m \propto I_D^{1/2}$ and $f_T \propto g_m$. However, it also results in a lower output resistance r_o , which is proportional to $1/I_D$, and hence, a lower intrinsic gain of $g_m r_o \propto (1/I_D)^{1/2}$. Lower gain results in higher gain errors in the op-amps, reducing the linearity and hence the dynamic range of the ADC.

In the second approach, overdrive voltages are kept constant and only the transistor widths are increased linearly for a proportional increase in current. In this case, the intrinsic gain is maintained, but f_T does not increase, resulting in an incomplete settling of the Op-Amp outputs for higher sampling frequencies. In both cases, we note that just by scaling currents proportionally, one cannot fulfill the requirements of faster response time while maintaining the same linearity (and resolution).

For the quantization process, the voltage comparators also need to switch faster to avoid the so-called comparator ambiguity [6]. The same arguments discussed above indicate that currents must increase with frequency and doing so linearly is not sufficient. These facts suggest that power dissipation in ADCs will increase rapidly with frequency, following similar trend as in digital circuits. This frequency scaling trend, as shown in Fig. 35, is found not only in CMOS technologies, but is also central to compound semiconductor technologies, such as SiGe, GaAs, and InP, that are traditionally used for very high-speed ADCs.

To overcome these issues in frequency scaling, new ADC architectures employing parallelism are used as in the case of digital circuits [91]. In the time-interleaved architecture (i.e., a parallel ADC architecture) such as the one shown in Fig. 36, multiple sub-sampling ADCs are used in parallel to sample the RF signal at different time instants within a full sampling clock cycle [89, 93, 94]. The outputs of these “sub-ADCs” are combined in the digital domain and post-processing is performed to suppress distortions caused

by timing errors, gain mismatches, and DC offsets between channels. The front-end of the time-interleaved architecture can have a single S&H stage [93], feeding all sub-ADCs, or a separate S&H block corresponding to each sub-ADC [89], or a combination of the these two approaches [94]. In the first and the third case, scalability to high sampling frequencies and to large sub-ADC numbers is still a challenge, and the same power considerations as discussed above for the ADCs apply to the front-end circuitry. The second architecture (discussed in [89]) can potentially be scaled to have higher sampling rates, but noise contributions due to timing jitter and residual timing offsets, which are discussed in the following paragraphs, reduce the ADC resolution. Also, this architecture requires a buffer to drive a large capacitive load of S&H blocks, which can limit the bandwidth and add significant power dissipation. As described in section 2, the noise added due to jitter in the sampling clock (aperture jitter noise) becomes significant at high frequencies. This noise increases quadratically with signal frequency and can severely degrade the SNR in high-speed ADCs.

For high speed and resolution in electronic ADCs, time-interleaving is required. In these ADCs, the clock jitter becomes much larger as the extensive clock generation circuitry, required to generate multiple clocks with precise phase delays, itself adds additional phase noise (or jitter). In addition, even after adaptive alignment and calibration, there is a residual timing misalignment between clocks going to different channels (for example, see the discussion regarding jitter in ref. [89]). Stringent requirements on clock accuracy thus become extremely challenging and ~ 100 -fs jitter levels demand very large clock amplitudes to avoid conversion of amplitude noise to phase noise in the electronic circuitry. Therefore, power dissipation in the clock generation and distribution circuitry in such ADCs becomes significant. In addition to all these contributors, the digital circuitry used for calibration and corrections in post processing steps can also add to the power consumption in all modern high-speed ADCs, in particular for high resolution and high sampling rate converters.

7.4. Power scaling in TSADC: A case study

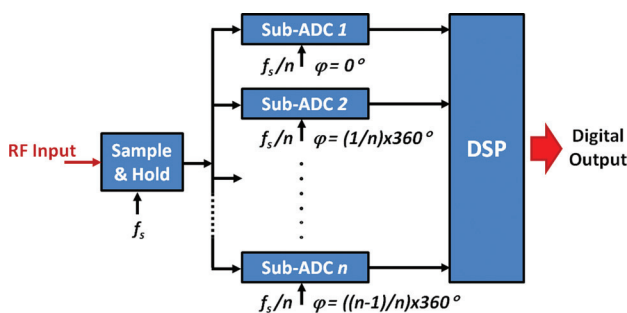


Figure 36 (online color at: www.lpr-journal.org) Schematic of a time interleaved ADC. The DSP reconstructs the input signal from individual samples and also performs calibration and error correction.

Time-stretching provides several advantages that can lead to reduced power consumption in high-speed ADCs. As described in section 2, stretching the signal in time by factor S reduces the noise power due to clock jitter by S^2 . This makes the time-stretch architecture very favorable for high-frequency applications, in which aperture jitter is the dominant source of noise.

Another key advantage of time-stretching is that none of the electronic digitizers see the original high frequency signal, since the signal frequency scales down upon stretching. In a TSADC operating in continuous time, the number of back-end digitizers is equal to the stretch factor. As a result, power consumption scales linearly with sampling frequency for the ADC. Of course the optical losses must

also be taken into account. In this section, we consider an example to show how time-stretching can be very effective in reducing power dissipation in high-speed ADCs.

The block diagram of a TSADC system for continuous operation is shown in Fig. 37. As an example, we consider the case of an 8-ENOB 10-GHz bandwidth TSADC. For this system, we consider an MLL source with 100-MHz pulse repetition rate. Therefore, the time segments that need to be captured by electronic digitizers are 10-ns long. A usable optical bandwidth of 40-nm (i.e. 5-THz optical bandwidth at 1550-nm center wavelength) can easily be obtained from a femtosecond fiber MLL, followed by a highly non-linear fiber [9]. For continuous modulation of the RF signal, these 40-nm pulses have to be stretched to 10-ns time width prior to electro-optic modulation, which requires -250 ps/nm dispersion in the first dispersive fiber, corresponding to dispersion of about 15-km standard single-mode fiber (SSMF). For the TSADC, dispersion compensating fibers (DCFs) are used because of their high dispersion-to-loss ratio compared to SSMF. Also, the normal dispersion prevents modulation instability that would occur and distort the signal if dispersion was anomalous such as in SSMF at similar wavelengths. Using a DCF, a dispersion value of -250 ps/nm is achieved with a distributed loss of about 0.65 dB (as found in [97] and from measurements in our lab), to which connector losses are added separately. If the stretch factor is S , the dispersion required in the second dispersive fiber becomes $(S-1) \times (-250$ ps/nm). Considering typical values, we estimate the losses in the Mach-Zehnder modulator to be 4 dB and losses in WDM filter, polarization controller, and connectors to be an additional 3 dB. Therefore, total loss in the optical link is about $S \times 0.65 + 4 + 3 = (S \times 0.65 + 7)$ dB. Also, we estimate the power at the input of each photo-detector to be ~ 1 mW, which gives 58-dB shot noise limited SNR for 500-MHz RF bandwidth, ~ 0.5 modulation depth, and ~ 0.8 A/W photo-detector responsivity. Similar or better thermal noise can easily be achieved from electronics and

photo-detector, resulting in better than 58-dB SNR with differential operation [36]. Back-end ADCs with 8-ENOB (i.e. 50-dB SNDR) can now be used to obtain 8-bit resolution, as the additional noise is compensated by differential operation. The noise contribution due to laser relative intensity noise (RIN) will not be significant, as even a readily available laser with a RIN of -150 dB yields an SNR of 63 dB under such conditions.

Power calculations for back-end digitizers and comparisons with electronic ADCs are based on the best available FOM giga-samples-per-second digitizer (with >8 ENOB resolution) published as of the date of this writing [94]. This digitizer captures waveforms at 1-GS/s (with 500-MHz Nyquist bandwidth) and has 0.5-pJ/step FOM. For these specifications and 8-ENOB resolution, power consumption is calculated to be 125 mW per back-end digitizer. For each optical WDM channel, differential and arcsine operations are performed, which not only improve the SNR by 3 dB but also suppress nonlinear distortion due to electro-optic modulation and chromatic dispersion. However, this requires that the number of back-end digitizers and photo-detectors be twice the stretch factor (or the number of optical channels). The electrical-to-optical power conversion efficiency of the laser is assumed to be 20%, since such efficiency is easily possible in fiber lasers [98] due to tight optical mode confinement in the fibers. For the photo-receivers, 50 mW of power is sufficient to bias each photo-detector and the subsequent amplifying stage to bring the signal to the full-scale voltage of the electronic digitizer, hence, this value is used in the calculations.

Finally, the combination of channel outputs in the digital domain requires signal processing and memory. Even though CMOS scaling has made digital circuits highly power efficient, a large amount of digital data is generated by ADC channels, resulting in significant power consumption in digital post-processing. Digital power is estimated to be the same as the total power consumed in the ADCs (as a similar trend is observed in [89]). Using these numbers with

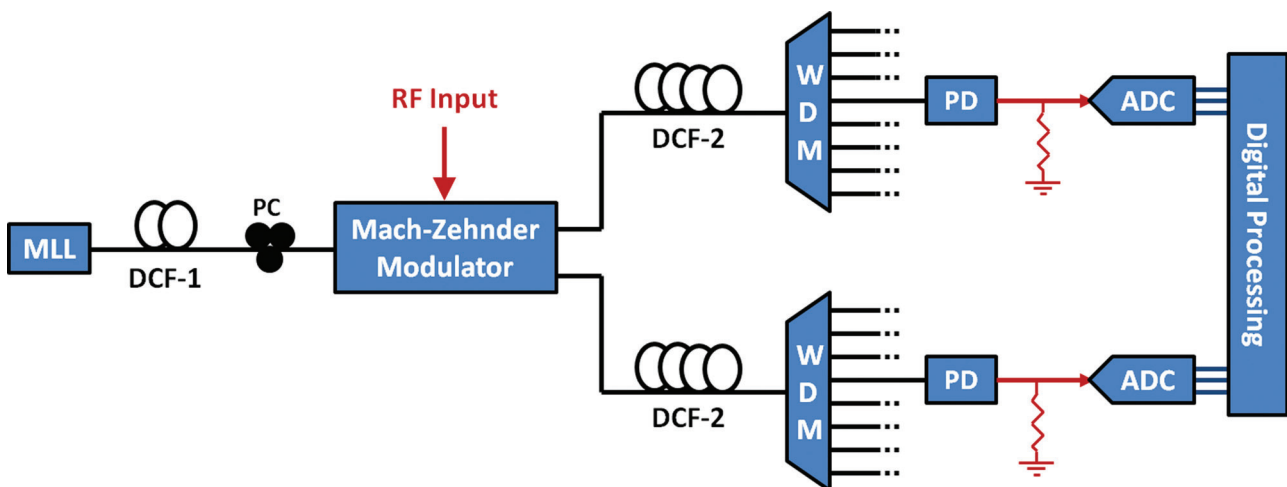


Figure 37 (online color at: www.lpr-journal.org) Schematic diagram of the time-stretch ADC for continuous operation (MLL: Mode locked laser; SC: Super-continuum; PC: Polarization controller; DCF: Dispersion compensating fiber; MZM: Mach-Zehnder modulator; PD: Photo-detector).

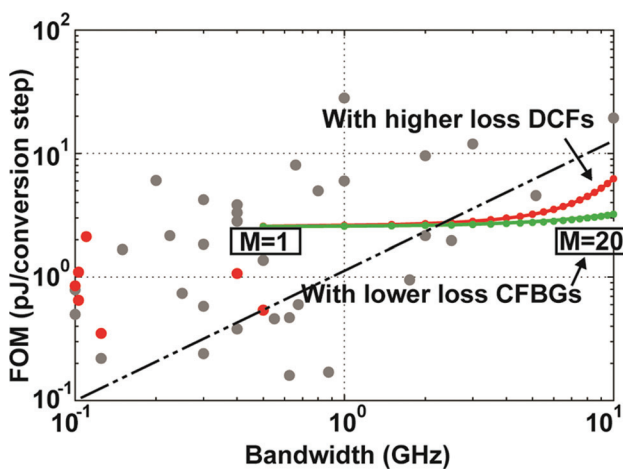


Figure 38 (online color at: www.lpr-journal.org) Projected figure of merit (FOM) for an 8-ENOB TSADC (red and green traces) and a conventional electronic ADC (dashed line - if the FOM were to scale linearly with bandwidth) as a function of ADC bandwidth. Constant FOM scaling can be continued to higher bandwidths if low-loss dispersive devices such as CFBGs and/or mid-stage optical amplification are used. Red markers represent electronic ADCs with >8 ENOB resolution. © 2009 IEEE. Reprinted, with permission, from [99].

1-mW input optical power at each photo-detector, the total optical and electrical powers can be calculated. The resulting power scaling for TSADC is plotted as the red curve in Fig. 38. It is observed that the FOM roughly stays constant up to 5 GHz as the power consumption of the electronics dominates at lower frequencies.

For higher RF signals, longer dispersive fibers are required to have larger stretch ratios, which add higher power penalty due to optical losses. Optical amplification using Erbium-doped fiber amplifiers, or distributed Raman amplification can be used to overcome these losses and improve the overall power efficiency significantly, while maintaining high SNR. Furthermore, with lower loss dispersive media, such as chirped fiber Bragg gratings (CFBGs), the linear power scaling trend can continue to larger bandwidths, as shown by the green curve in Fig. 38. In these calculations, the loss in CFBGs is assumed to be half that of the DCFs, though in reality, the loss in CFBGs is even lower [100]. However, the CFBGs can have a significant group delay ripple, which must be reduced or corrected using digital signal processing [101, 102].

Table 2 summarizes the power consumption budget in a 10-GS/s TSADC using DCFs and 20-GS/s TSADCs using DCFs and CFBGs as the dispersive media. All these power calculations are for 8-effective bits of resolution and Nyquist rate sampling. The 10-GS/s TSADC is projected to consume power of about 8.3 W and the 20-GS/s TSADC using DCFs is expected to consume about 32 W of power. In the 20-GS/s ADC, the optical power requirement increases because of longer DCFs that add more losses. However, if optical amplification or CFBGs are used, the power consumption can be reduced to about 16.5 W.

Compared with this, the projected power consumption of purely electronic 10-GS/s and 20-GS/s ADCs is 12.5 W and 50 W respectively. These projected values are based on linear FOM variation with frequency. However, from empirical data, it appears that this variation is super-linear, which increases the power consumption of high-speed electronic ADCs even faster, and hence, makes the use of photonics even more attractive. At present, however, there are no electronic ADCs available with 8 or higher ENOB resolution and 10 or 20-GS/s Nyquist sampling rates – a direct consequence of the aperture jitter limitation.

If a back-end electronic digitizer with higher bandwidth is available, the laser pulse repetition rate in the TSADC can be increased, resulting in a reduced time aperture (or inter-pulse period). Reducing the time aperture reduces the dispersion values required in the system, which helps in reducing optical losses and scaling TSADC power linearly to even higher frequency ranges. Use of wider optical bandwidths also reduces the demand on dispersion and curtails optical losses. Although Mach-Zehnder modulators generally add significant wavelength-dependent bias offsets for wide optical bandwidths, digital processing can easily suppress the distortions added by these bias offsets in the TSADC [36, 44].

As a preliminary experimental proof-of-concept, we consider a Tektronix DPO71604 digitizer which is the highest ENOB electronic digitizer capable of 10-GHz bandwidth available today. This digitizer has 5.9-ENOB resolution over 10-GHz bandwidth, and consumes about 1000-Watt electrical power for 4 channels. Assuming the power scales linearly with the number of channels, this digitizer will consume 250 W for a single 10 GHz unit. As an example of a comparable TSADC, we present results for a recent demonstration [9]. The digitizer attained 7.2-ENOB resolution over 10-GHz instantaneous bandwidth, which to the best of our knowledge, is the highest resolution achieved to date for an analog-to-digital conversion over 10-GHz instantaneous bandwidth (not to be confused with reports of conversion at high carrier frequencies but over a very narrow instantaneous bandwidth). As outlined below, such a TSADC consumes only 85W.

In this demonstration, a duty cycle of 4% was set and the power consumption of the optical front-end (including photo-receivers) was 3 W. For continuous operation (100% duty cycle) the power dissipation in the optical front-end will be 75 W. In that experiment, the Tektronix DPO71604 was used as the back-end digitizer for ease of implementation. The RF bandwidth was digitally filtered to 1 GHz to increase the resolution to 7.2 ENOB. Hence, the optical front-end was not the resolution bottleneck. Since only 1 GHz of bandwidth is required in the subject TSADC, the Tektronix DPO71604 is obviously not the ideal back-end for this demonstration. If monolithic 1-GHz electronic digitizers, such as those considered in Table 2, were used, the power dissipation for the entire back-end of the TSADC would be 10 W, resulting in a total dissipation of 85 W for the 10-GHz TSADC with 7.2 ENOB resolution. This is to be compared with 250 W for the best 10-GHz all-electronic digitizer (DPO71604), which only provides

Table 2 Power dissipation budget in the TSADC with 8-ENOB Resolution [Watts]. (DCF: Dispersion compensating fiber; CFBG: Chirped fiber Bragg grating.)

	10-GS/s TSADC using DCFs (S=10)	20-GS/s TSADC using DCFs (S=20)	20-GS/s TSADC using CFBGs (S=20)
Laser	2.3	20	4.5
Photo-detectors	1	2	2
Back-end Electronic ADCs	2.5	5	5
Digital Electronics & Memory	2.5	5	5
Total TSADC Power	8.3	32	16.5
Electronic ADC Power for same Performance	12.5	50	50

5.9-ENOB resolution. In fact, the duty cycle of the DPO71604 is a fraction of one percent (due to memory size limitation and data processing overhead); therefore, the comparison favors the TSADC much more decisively than the power numbers above suggest.

8. Spectral efficiency improvement in TSADC via polarization multiplexing

As described in this manuscript (section 2), the time aperture [25] of the PTS system is equal to the width of the optical pulse after the first dispersive fiber. When double side-band modulation (DSB) is employed to modulate the RF signal onto the pre-chirped pulse, the dispersion penalty limits the effective 3-dB RF bandwidth of the PTS to an expression proportional to the inverse square root of the initial dispersion. Hence, for a certain desired RF bandwidth, a limit is placed on the maximum pre-dispersion that can be tolerated. Hence, in order to increase the time aperture, one must use time-stretching pulses with larger optical bandwidth. Alternatively stated, a figure of merit termed the time-bandwidth product (TBP), which is the product of the time aperture and the RF bandwidth, depends linearly on optical bandwidth. In order to meet the increasing RF bandwidth demands of modern applications, the PTS system must therefore employ broadband optical pulses with larger optical bandwidth, straining the capabilities of the super-continuum (SC) source, and eventually leading to undesired distortions, such as wavelength-dependent loss and optical nonlinearity. Improving the spectral efficiency of the PTS system equates to increasing the TBP independent of optical bandwidth. In this section, we describe a dual-polarization photonic time-stretch (DP-PTS) technique [50], which exploits polarization multiplexing to improve the spectral efficiency of the PTS technique.

8.1. Dual-polarization time-stretch pre-processor

The DP-PTS presented in [50] maps two consecutive segments of the RF signal onto two orthogonal polarization

states and multiplexes them onto a single-wavelength channel, thereby doubling the effective time aperture while keeping the optical bandwidth constant. To demonstrate this approach, a broadband pulse laser followed by a dispersive fiber (total dispersion of -41 ps/nm) is used to generate pre-chirped pulses as illustrated in Fig. 39. The pre-chirped optical pulses are polarized and split into two orthogonally polarized pulse trains via a polarization beam splitter. A polarization controller before the polarization beam splitter is adjusted to ensure equal amplitudes in the two channels upon detection. The two orthogonally polarized pulse trains are skewed relative to each other in time, leaving a small region of overlap. They are then modulated by the same RF signal in two dual-output push-pull Mach-Zehnder modulators. Due to the time skew, the two corresponding pulses capture two consecutive segments of an RF signal, doubling the time aperture. The two complementary outputs of the modulators are used to perform differential operation for 2nd order distortion cancellation. To avoid mismatch between the signal paths of the complementary outputs, the complementary pulse trains are multiplexed in time onto the same polarization state. Polarization controllers at each output are used to align the polarizations. The pulses from the complementary outputs are delayed relative to each other by approximately half the pulse period to avoid overlap after stretching. The orthogonally polarized pulse trains from the two modulators are overlapped in time by a second delay line in one of the arms and then separately amplified using two C-band erbium doped fiber amplifiers (EDFA). The two signals are then polarization-multiplexed using a polarization beam combiner. The polarization multiplexed optical pulse trains are stretched using total dispersion of -606 ps/nm to achieve a stretch factor of ~ 16 .

In order to mitigate the crosstalk between the polarization channels due to polarization mode dispersion (PMD), a double-pass configuration consisting of a spool of dispersive fiber with total dispersion value of -303 ps/nm, a circulator, and a Faraday mirror was used. After dispersion, the polarization multiplexed signals are demultiplexed via a polarization beam splitter. The useful portion of the optical bandwidth (~ 20 nm) around 1551 nm is filtered, and the stretched optical pulses are detected using two photo-detectors. The obtained RF signals are digitized

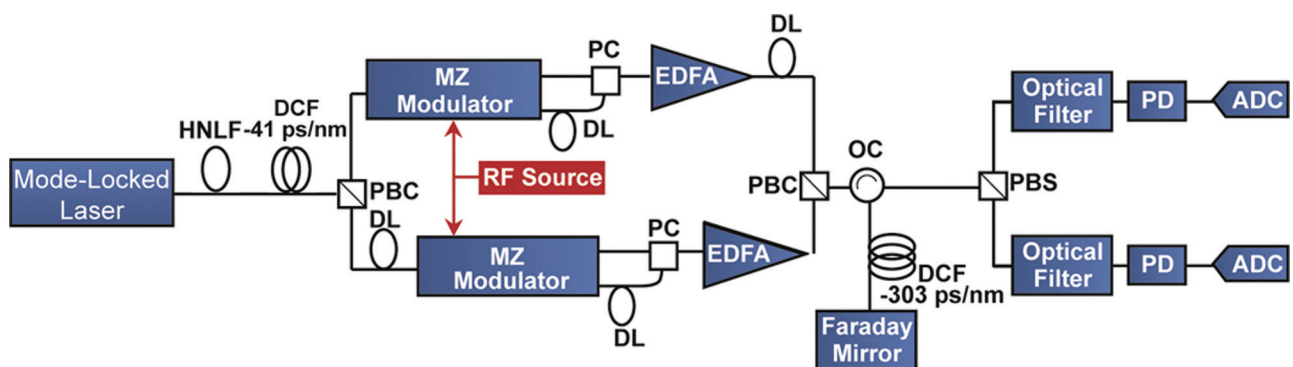


Figure 39 (online color at: www.lpr-journal.org) Schematic of dual-polarization photonic time-stretch (DP-PTS) preprocessor. HNLf: Highly nonlinear fiber, DCF: Dispersion compensating fiber, PBS: Polarization beam splitter, DL: Delay line, EDFA: Er-doped fiber amplifier, PC: Power combiner, PBC: Polarization beam combiner, OC: Optical circulator, PD: Photo-detector, ADC: Analog-to-digital converter. In order to mitigate the crosstalk between the polarization channels in the DP-PTS, a double-pass configuration consisting of a spool of DCF and a Faraday mirror was used to stretch the RF signal. For simplicity, the polarization controllers before the polarization beam splitters/combiners and Mach-Zehnder modulators are not shown. © 2012 IEEE. Reprinted, with permission, from [50].

by a 16-GHz real-time oscilloscope with 50-GS/s sampling rate (Tektronix-DPO71604).

Since the bandwidth of the time-stretched RF signal is lower than 1.1 GHz, a digital low-pass filter was applied in the digital signal processing stage to reduce the bandwidth from 16 GHz to 1.1 GHz, thereby emulating a monolithic commercial off-the-shelf ADC. Digital signal processing is performed offline for correcting nonlinear distortions (described in section 4) such as 2nd-order distortion due to dispersion, time-warps, and 3rd-order distortion due to the Mach-Zehnder modulator. The DP-PTS preprocessor demonstrated in [50] achieves an effective time aperture of $2 * 41\text{ps/nm} * 20\text{ nm} = 1.64\text{ nsec}$. In the current configuration, the 3-dB RF bandwidth due to the dispersion penalty is 28 GHz, whereas a single channel PTS, requiring double the dispersion, would have a reduced 3-dB RF bandwidth of 20 GHz.

8.2. Experimental results

To demonstrate the functionality of the DP-PTS preprocessor, a single-tone test at 6 GHz and a two-tone test at 8.2 GHz and 10.25 GHz were performed as shown in Fig. 40(a) and 40(b). After distortion corrections, the captured segments of each polarization channel are stitched in the digital domain to verify the increase in the effective time aperture. The power spectrum of the RF signal is calculated after stitching more than 300 consecutive segments. For a 10-GHz instantaneous bandwidth, the single-tone [Fig. 40(a)] and two-tone [Figure 40(b)] tests show 6.1–6.3 (obtained by the sine-curve fitting method) and 5–5.1 (obtained by spectral domain method) effective number of bits (ENOBs) respectively. These results showcase the recording of high-bandwidth RF signals using this system.

Polarization mode dispersion (PMD), caused by the birefringence of the optical fiber and the random variation of its orientation along the fiber length [103] is the

major source of noise in the DP-PTS system. The PMD results in crosstalk between the two polarization channels while propagating through the second spool of DCF. The double-pass configuration for time-stretching in the second spool of DCF reduces the channel crosstalk to a great extent. However, this configuration may not be useful for applications in which the RF signal is to be detected at the remote site. An additional source of noise is the Rayleigh back scattering of the signal in forward propagation that is directed to the photo-detector.

9. TSADC simulator and roadmap to 10-ENOB 10-GHz TSADC

The time-stretch ADC is a complex system that requires a non-trivial theoretical framework to understand the underlying principles in detail. Additionally, numerous electrical, optical, and electro-optic components are needed for practical realization of the system, which add their own noise and distortion effects to the system, influencing the overall system performance. Therefore, to quickly verify the theoretical prediction and to determine the influence of different component parameters on the time-stretch system performance, a TSADC computer simulator has been developed and described in [104]. This simulator can also aid a person who is not well-familiar with the TSADC in learning more about this system or in designing a TSADC for a particular application.

9.1. Simulator description

To simulate the TSADC functionality and evaluate its performance, the TSADC Simulator program has been developed using Simulink [105]. Simulink is a commercial software tool developed and distributed by The Mathworks Inc., and it is part of the MATLAB software suite. It provides the capability of performing signal flow based simulations,

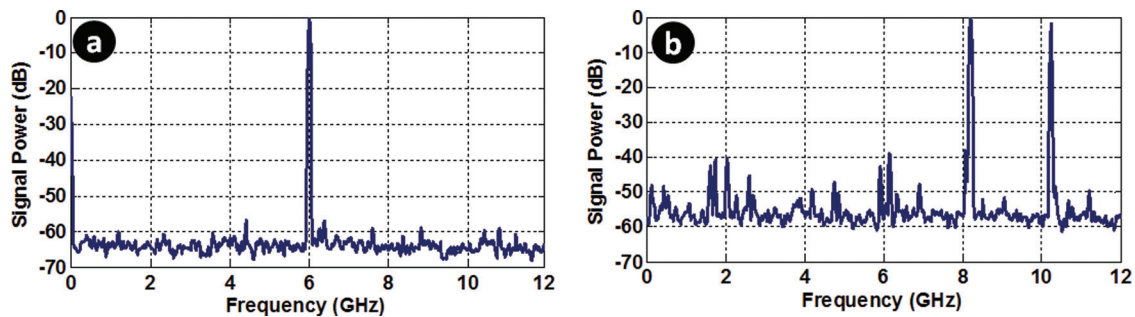


Figure 40 (online color at: www.lpr-journal.org) (a) Single-tone test with 6-GHz RF signals; (b) two-tone test with 8.2-GHz and 10.25-GHz RF signals. More than 600 segments (300 segments per polarization channel) are stitched coherently to generate these plots. © 2012 IEEE. Reprinted, with permission, from [50].

as well as performing large-scale vectorial operations. A library of hierarchical models for different components in the system can be developed in Simulink. Each model can in itself consist of many subsystem models. The models can also include a large variety of functions, such as IIR/FIR filters, FFT/IFFT blocks, non-linear components, and mathematical functions etc. At any level of the hierarchy, these models can be dragged and dropped and graphically connected by arrows to achieve signal flow based simulations.

The parameters used in simulation can be set as constants or as variables. These values can also be changed by the user before running the simulation by clicking on the “model masks” representing different subsystem blocks. Figure 41 shows a representation of the top-level schematics for the baseline architecture of the TSADC system. The different photonic components shown in the schematics include the laser pulse generator that provides its output to the first dispersion component, creating a chirped pulse. The output of this component goes to a dual-output Mach-Zehnder modulator (MZM) which modulates the RF signal over it. Currently, the RF signal is generated internally in the MZM, but it can be modified to provide an external RF signal. As illustrated in the block-level schematics, the blocks with a label “(w)” indicate that the inputs to those blocks are in frequency domain. Hence, if the time-domain signal is to be given as an input to these blocks, first it should be converted to frequency domain using the fast Fourier transform block available in the Simulink library.

The two outputs of the MZM, which facilitate differential [36, 63] or phase-diverse operations [63, 65], propagate through the Raman-amplified dispersion compensating fibers (DCFs) that act as virtually lossless dispersive components [26], and stretch the modulated optical pulses in time. The outputs of these fibers are filtered by the WDM filters, and are subsequently converted to the electrical domain by the photo-receiver. By default, the photo-receiver block models the commercially available AD-50IR photo-receiver from Newport Corporation.

The obtained electrical signal is quantized using an ADC model. Before quantization, the full-scale voltage range of the ADC is automatically adjusted through the “ADC V_{in} Autorange” block, which senses the power level received from the photo-receivers. The baseline architec-

ture also includes “Variable Time Delay” blocks that emulate timing and gain mismatches between the channels. The signal vectors coming out of the ADCs are sent to the MATLAB workspace, where different post-processing algorithms are applied to the signal to remove envelope modulation and distortions from the signal. The TSADC performance can finally be evaluated from these measurements for different configurations and signal processing algorithms.

Each block, representing a component, has a number of different parameters that can be modified to change the configuration of the TSADC system. For example, the optical pulse generator (“Single Pulse Generation”) block includes the following variable parameters [as shown in Fig. 42(a)]: number of simulation points, center wavelength, laser pulse width, average laser power, laser pulse repetition rate, and relative intensity noise (RIN) in the laser. There is also a checkbox to enable/disable the relative intensity noise of the laser. Flexibility of enabling or disabling different noise contributors gives the capability of evaluating noise contributions from different stages independently. Similarly, for the Mach-Zehnder modulator block, there are different options that include type of the modulator, the drive voltages and frequencies, bias voltages and insertion loss, as illustrated in Fig. 42(b). A complete list of different blocks used in the baseline architecture (Fig. 41) and their details are shown in Table 3.

The current version of the simulator includes almost all non-idealities that can affect the TSADC system performance except the optical nonlinearities (described in section 5). Simulation of optical nonlinearities is a computationally intensive process. It is carried out by solving the nonlinear Schrödinger equation (NLSE) described in section 5. Analytical solution to the NLSE does not exist. Numerically, the NLSE is solved using split-step Fourier method [30]. This becomes computationally very exhaustive due the large signal vector size, particularly in case of the TSADC, which has a very large time-bandwidth product due to large optical bandwidth and simulation time window. A MATLAB code for simulation of optical nonlinearities has been developed. However, it has not yet been integrated with the main TSADC simulator so far because of its heavy computational requirements.

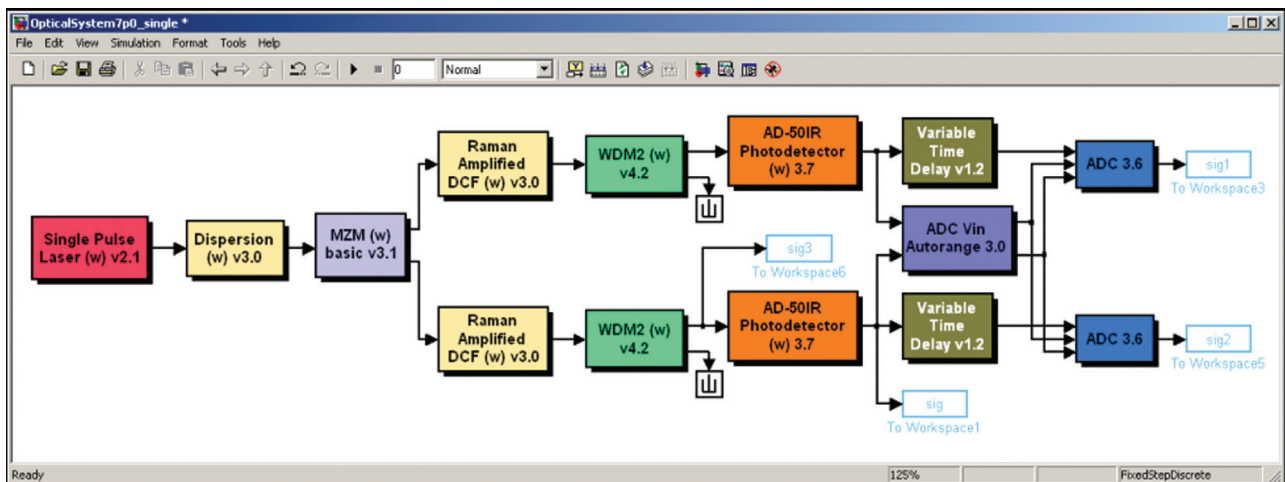


Figure 41 (online color at: www.lpr-journal.org) A snapshot of the top-level schematic of the TSADC system as it appears in Simulink. An extension of this schematic is intended to be used for the demonstration of a continuous-time 10-ENOB resolution TSADC with 10-GHz bandwidth.

9.2. A roadmap for 10-ENOB resolution over 10-GHz bandwidth

With this TSADC simulator, a baseline architectural model of the TSADC has been created (shown in Fig. 41), for achieving 10-GHz bandwidth analog-to-digital conversion with 10 bits of resolution. The parameter values used in the architecture are listed in Table 4. For different simulations, all but one of the parameters were held constant. Values of the variable parameters were swept across a practical range to obtain the ENOB resolution results versus these parameters.

Figures 43(a)-(e) show the results obtained from these simulations (reproduced from [104]). The obtained ENOB values do not perfectly lie on the fitting curves because of randomness of the noise added by different stages in the simulator. However, these results are very useful in giving the trends and the average behavior. For more accuracy, a large number of Monte Carlo simulations would be required, which will improve the accuracy, but will become very time consuming.

These trends indicate that the shot noise and the amplified spontaneous emission (ASE) noise are the dominant sources of noise for this system, as the ENOB continues to improve with improving Raman amplification noise figure or increasing input power at the photo-detector. The simulations also give the optimum value of the modulation depth to be ~ 0.35 . Figure 43(b) predicts an optimum value of the modulation depth to be ~ 0.4 . However, as discussed earlier, the ENOB results obtained from each simulation run are not perfect because of variances in random noise. From a large number of simulations, a modulation depth of 0.35 was found to be optimum value giving >10 -ENOB resolution.

Larger modulation depth results in stronger nonlinear distortion, while smaller modulation depth decreases the

signal power, and hence, the SNR. Without the arcsine operation, it can be observed that the effect of increasing modulation depth is severe, as the 3rd-order distortion increases monotonically with the modulation depth. Hence, even though the memory-less arcsine operation cannot perfectly suppress the 3rd-order distortion, which shows a frequency-dependent behavior, it is still useful for suppressing the distortion to a great extent. The TSADC simulator can be very useful in designing the TSADC system and characterizing its performance for different system parameters. Using this simulator, a time-stretch analog-to-digital conversion with 10-GHz bandwidth and 10-ENOB resolution has been shown to be viable.

10. Real-time burst sampling technique

With faster electronics, increasing bandwidths in communication systems (such as 100Gbps+ optical links), and newer applications, the demand for larger bandwidth oscilloscopes continues to grow. Availability of high-speed digitizers (or ADCs) for fault diagnostic techniques, such as time-domain reflectometry (TDR) [106], can obviate the necessity of costly and difficult-to-use instruments such as network analyzers, which require slow frequency domain sweeps and a number of time-consuming calibration steps. Time-domain oscilloscopes are also replacing the spectrum analyzers as the speed of ADCs improves. Eventually, with faster ADCs, these oscilloscopes are expected to become universal equipment for measuring and analyzing all types of electrical signals.

Purely electronic ADCs cannot meet the demand for these applications in the near future because of their bandwidth limitations, as discussed in section 1. Here, we begin with the classification of different oscilloscopes (i.e., digitizers) and show how a simplified (single channel) version

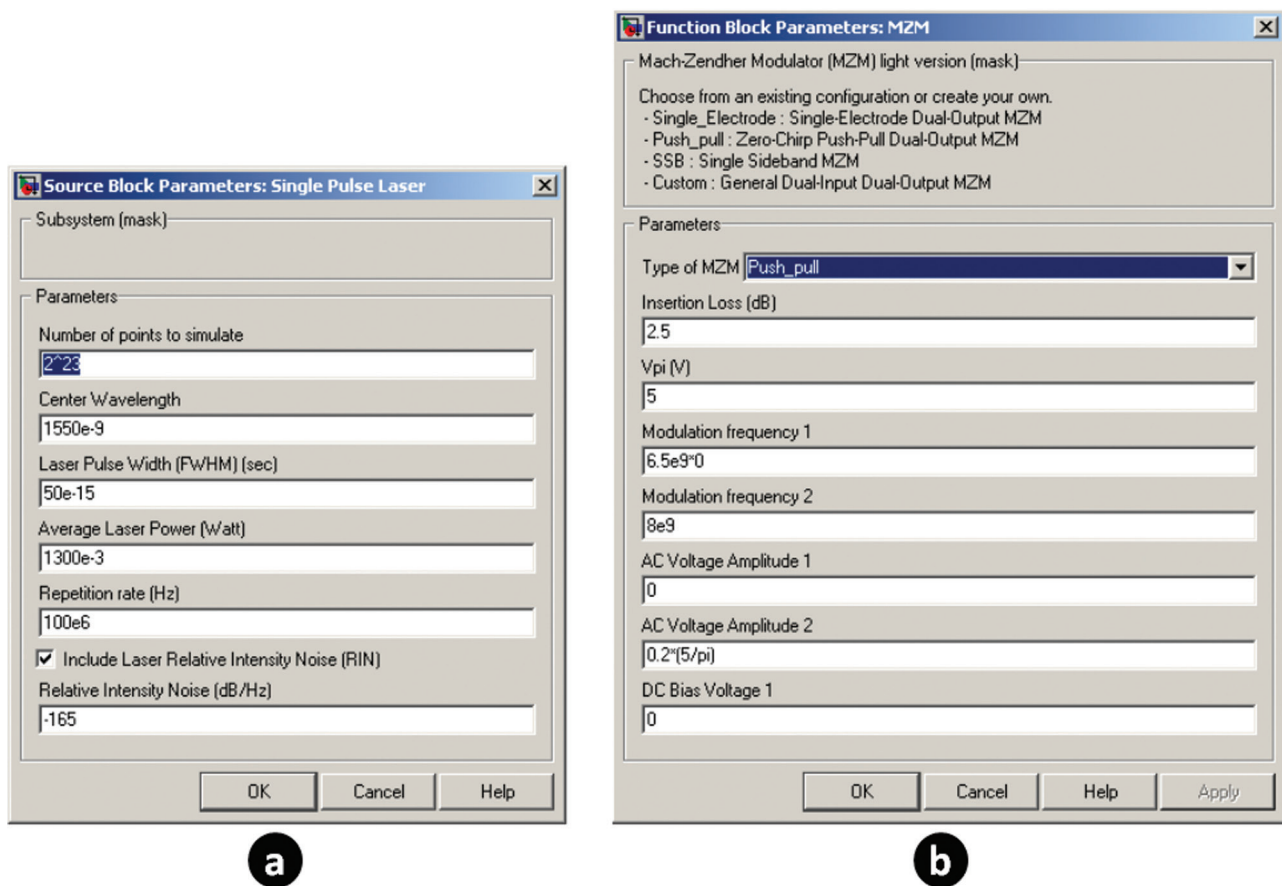


Figure 42 (online color at: www.lpr-journal.org) Snapshots of menu windows that open up on double-clicking different blocks. Menu window for specifying: (a) different laser pulse parameters; (b) the Mach-Zehnder modulator (MZM) parameters.

of the TSADC, which performs real-time burst sampling, can achieve this goal. Since oscilloscopes primarily rely on digitizers (or ADCs), these words have been interchangeably used in the discussion.

10.1. Classification of digitizers

Digitizers are broadly categorized into two classes. Equivalent-time digitizers (or sampling oscilloscopes) rely on repetitive or clock synchronous nature of the signals to reconstruct them in time. In a sampling oscilloscope, the signal is sampled at mega-hertz frequencies (typically 100-kHz to 10-MHz) and then, reconstructed digitally. Hence, it requires a long time to obtain the original signal with high fidelity [as shown in Fig. 44(a)]. While they can reach equivalent-time bandwidths of up to 100-GHz, they are not capable of capturing non-repetitive waveforms. Even for repetitive signals, they cannot provide real-time information about the dynamics that occur at rates faster than a few MHz. Equivalent-time sampling is similar to the strobe light technique used for measuring cyclical events, which are much faster than the speed of the detector. For example, periodically flashing strobe light on a vibrating tuning fork can make it appear stationary or very slowly vibrating and can be used for studying its vibrational motion.

The second type of digitizers, called real-time oscilloscopes [Figure 44(b)], continuously sample the signals, but have input bandwidths limited to only a few GHz. The fastest practical real-time oscilloscope available today has a bandwidth of about 60 GHz.

Recently, real-time burst sampling (RBS), a new technique that uses equivalent time operation of the TSADC, was introduced. The instrument performing this operation is called the time stretch enhanced recording (TiSER) oscilloscope [107]. In contrast to a sampling oscilloscope, which captures only a single sample in one shot, this instrument asynchronously records real-time snapshots of the signal segments, each spanning several samples [Figure 44(c)]. It then displays them on equivalent time scale, after proper synchronization and timing in software. Since the captured segments are in real-time (not just single sample point), the TiSER oscilloscope can record ultrafast non-repetitive dynamics that occur within the segment period. Such fast events cannot be observed by a sampling oscilloscope because it lacks real-time capability, or by a real time digitizer because of its limited front-end bandwidth. Therefore, the TiSER oscilloscope fills the performance and functional gap between sampling oscilloscopes and real-time digitizers.

As illustrated in Fig. 45, a commercially available 1.5-GHz real-time ADC can be used to achieve real-time burst

Table 3 Different TSADC simulator blocks used in the baseline architecture.

Component	Description
Single Pulse Laser	Optical Pulse Source. Variable parameters: number of simulation points, center wavelength, laser pulse width (FWHM), average laser power, repetition rate, and relative intensity noise (RIN). Also, there is an option to enable/disable RIN.
Dispersion	Dispersive component. Variable parameters: propagation parameters $\beta_0, \beta_1, \beta_2, \beta_3$, fiber length, fixed and distributed loss
Mach-Zehnder Modulator (MZM)	Variable parameters: Type of modulator, insertion loss, V_π , modulation frequencies and amplitudes, DC bias voltage
Raman Amplified DCF	Dispersive fiber with Raman amplification. Variable parameters: propagation parameters, fiber length, net distributed loss (or gain), connector loss, Raman amplification noise figure
WDM2	Wavelength division multiplexing filter with multiple output channels. Different filter types include Super-Gaussian, Equiripple, Brick-wall or a custom shape. Other parameters are based on the filter type selection.
AD-15IR Photo-detector	Uses an empirical model of Newport AD-15IR photo-detector. Variable parameters include: responsivity, detection bandwidth and 3-dB saturation power. There is an option of including thermal noise and/or shot noise, etc.
Variable Time Delay	Applies variable delay and gain for each channel (to emulate gain and delay mismatches between different channels).
ADC V_{in} Autorange	Obtains input signal and feeds back to range and adjusts voltage range of the ADC to maximize dynamic range.
ADC	Analog-to-Digital Converter. Variable parameters include: number of quantization bits, input ADC bandwidth, sampling rate, and specification of ENOB, SNR, or noise figure, option to include or not include thermal noise bandwidth, voltage range (if auto-setting of voltage is disabled).

Table 4 Parameters used for simulations of the TSADC with the baseline architecture shown in Fig. 41.

Simulation Parameters	Value
Laser optical bandwidth	70 nm
Laser repetition rate	100 MHz
Laser RIN	-165 dB/Hz
Stretch factor	20
Total dispersion value	3 ns/nm
Raman amplification noise figure	3 dB
MZM modulation depth	0.35
Two-tone input frequencies	6.5 GHz and 8 GHz
WDM bandwidth	30 nm
Photo-detector responsivity	0.8 A/W
Photo-detector saturation power	120 mW
Photo-detector input power (average)	13 mW
Back-end ADC bandwidth	50 MHz
Back-end ADC resolution	11 ENOB

sampling with up to 50-GHz bandwidth when the stretch factor is 34. The spectral capture shows a gap in the middle of real-time bandwidth coverage of TiSER, which is due to the non-continuous nature of the RBS technique. This gap is bounded on the lower end by the pulse repetition frequency of the laser $1/T_{\text{laser}}$ and on the upper end by the

inverse of the segment length of the unstretched signals ($1/T_{\text{segment}}$).

10.2. Operation of time-stretch enhanced recording oscilloscope

In a time-stretch system, the effective bandwidth of the RF signal is compressed prior to digitization by stretching the waveform in time. The resultant signal can be recorded by a slow real-time electronic ADC. As in a conventional sampling oscilloscope, time-stretching also distorts the signal, but these distortions can be removed digitally, as discussed in Sections 3, 4, and 6. Thanks to digital post processing algorithms, the bandwidth of the TiSER at present is limited only by the bandwidth of the electro-optic modulator, which is currently over 100-GHz [27, 56, 68].

In the TiSER oscilloscope, each segment of the input waveform is captured by a chirped optical pulse. For the n -th laser pulse, the signal recorded at absolute time instant, t , by a real-time digitizer is displayed on the time axis of the oscilloscope window at the time point,

$$t_{\text{out}} = \left(nT_{\text{laser}} + \frac{t - nT_{\text{laser}}}{S} \right) \text{modulo } T_{\text{trigger}} \quad (10.1)$$

Here, T_{laser} is the pulse repetition period of the laser, T_{trigger} is the period of the trigger signal (eye diagram time

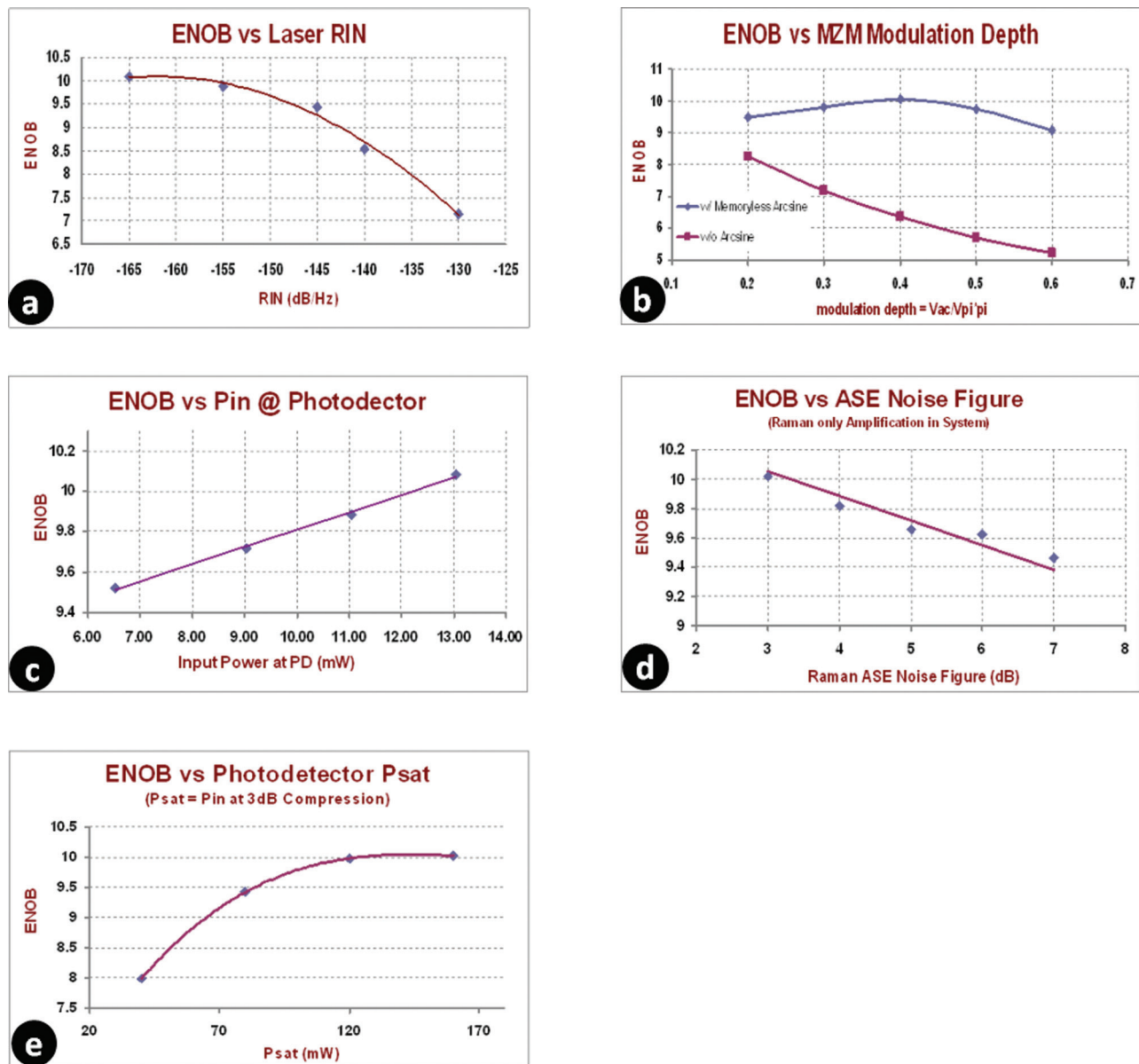


Figure 43 (online color at: www.lpr-journal.org) Effective number of bits (ENOB) of resolution obtained from the TSADC simulator versus different variable parameters.

window) that is synchronous with the signal to be captured, and S is the stretch factor. The expression in the braces converts the time scale of the captured (stretched) signal segments to original signal time scale (division by S is for unstretching the segments). The *modulo* operation generates the eye diagram by chopping and overlaying these time segments. The trigger signal is provided externally as in case of most sampling oscilloscopes. The trigger and laser periods can be obtained in software from the captured pulses and the trigger clock using digital phase locking. Hence, the TiSER *does not* need to satisfy any additional condition to capture the signal when compared to a sampling oscilloscope.

10.2.1. Capture of 45-Gbps data eye using TiSER oscilloscope

Capture of a 45-Gbps pseudo-random bit sequence (PRBS) data eye was demonstrated using TiSER [107]. This data was generated by an Anritsu MU181020A pattern generator and the obtained eye diagram is shown in Fig. 46. The system consists of a time-stretch pre-processor with a stretch factor of 34, and a back-end electronic digitizer with 1.5-GHz analog bandwidth (i.e. 3-GS/s Nyquist sampling rate). Therefore, time-stretching increases the effective analog bandwidth to 50 GHz and Nyquist sampling rate to 100 GS/s, respectively. The segment length, given by the

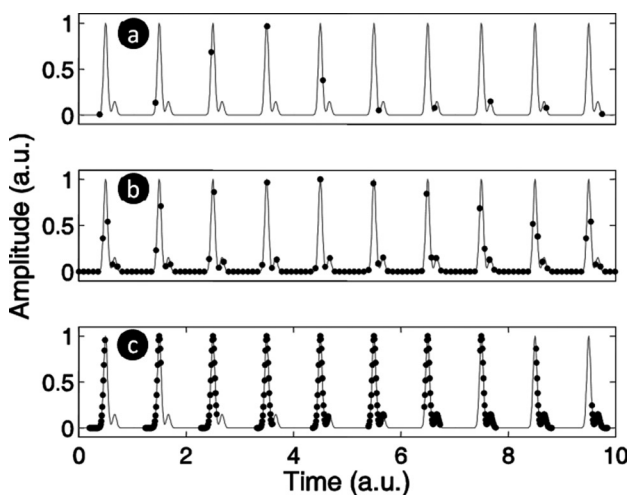


Figure 44 Different sampling techniques are shown. (a) An equivalent-time oscilloscope samples signals at very slow rates and reproduces their repetitive or average behavior. (b) A real-time digitizer samples signals continuously but has limited bandwidth, hence can only record slow signals accurately. (c) The TiSER scope can perform real-time burst sampling (RBS), capturing ultra-wide bandwidth signal segments in real-time and reproducing them on equivalent time scales. Therefore, it can capture both fast signals and their transient behavior. Reprinted with permission from [107]. Copyright 2009, American Institute of Physics.

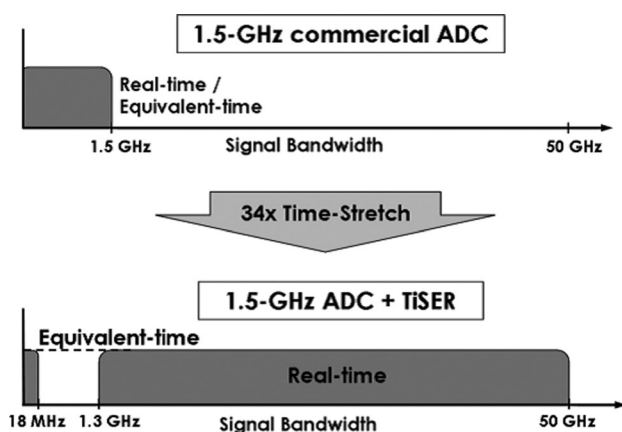


Figure 45 The TiSER oscilloscope can extend the real-time and equivalent-time bandwidths of electronic ADCs by the stretch factor. The gap in the middle of the real-time bandwidth coverage is due to the non-continuous nature of the real-time burst sampling (RBS) technique.

length of the chirped optical pulse that captures the analog signal is 0.6 ns. As a result, every captured segment consists of 60 independent samples, which repeats every 37 MHz (pulse repetition period of the laser). Hence, the system provides a sample collection rate of $60 \times 37 \text{ MHz} = 2.2 \text{ GHz}$. Compared with this, the sampling rate achieved by the fastest commercially available equivalent-time oscilloscope is only 10 MS/s, which results in about 220 times faster sampling rate using TiSER.

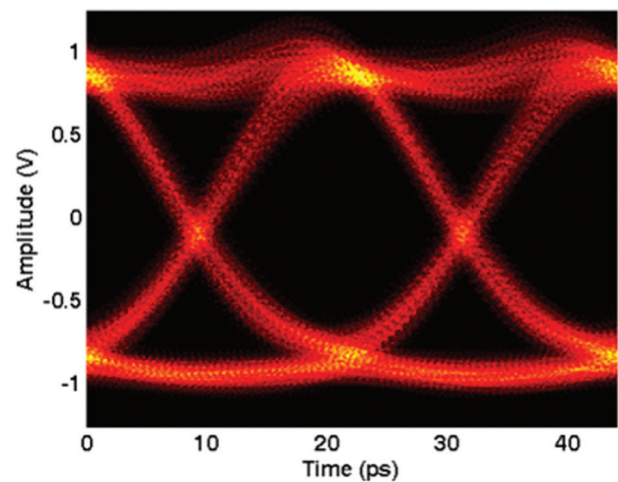


Figure 46 (online color at: www.lpr-journal.org) Eye diagram of 45-Gbps PRBS data captured in 10 μs using TiSER scope with a stretch factor of 34. The experiment used a 50-GS/s real-time oscilloscope with 16-GHz analog bandwidth. A 1.5-GHz low pass filter was applied in software to emulate the digitizer as a monolithic commercial off-the-shelf ADC.

Eye diagrams provide vital information about signal integrity in a serial data communication link. Jitter measured as fluctuations in zero-crossing points in the eye diagram, indicates channel response and transmitter characteristics. Measurement of jitter for long PRBS is required to ensure better than 10^{-12} bit error rate (BER). Eye diagram measurements performed using BER test oscilloscopes may require more than a day to scan the data eye completely [108]. Even when the jitter is analyzed statistically, the observation time can be long (since all captured points do not lie close to the zero crossings). On the other hand, each segment from the TiSER has a continuous run of samples. As a result, time points for all zero crossings occurring within one segment can be obtained using interpolation between segments, improving jitter histogram acquisition speeds by 3 to 4 orders of magnitude. Additionally, with RBS, fluctuations occurring over very short time intervals, such as short time jitters, can be analyzed easily.

10.2.2. Digital equalization of high-speed data

High-speed communications systems can achieve >100-Gbps data rates using advanced modulation formats and will require high-resolution ADCs with 20-GHz or more bandwidth. While there is an effort on developing the desired ADCs operating in continuous mode, the TiSER oscilloscope can act as a dummy receiver for such high-speed applications. Since the TiSER oscilloscope can capture real-time segments of wideband signals with high-resolution, demodulation and post processing steps such as equalization, clock recovery, carrier phase recovery etc. can be performed on these segments to evaluate the transmission system performance.

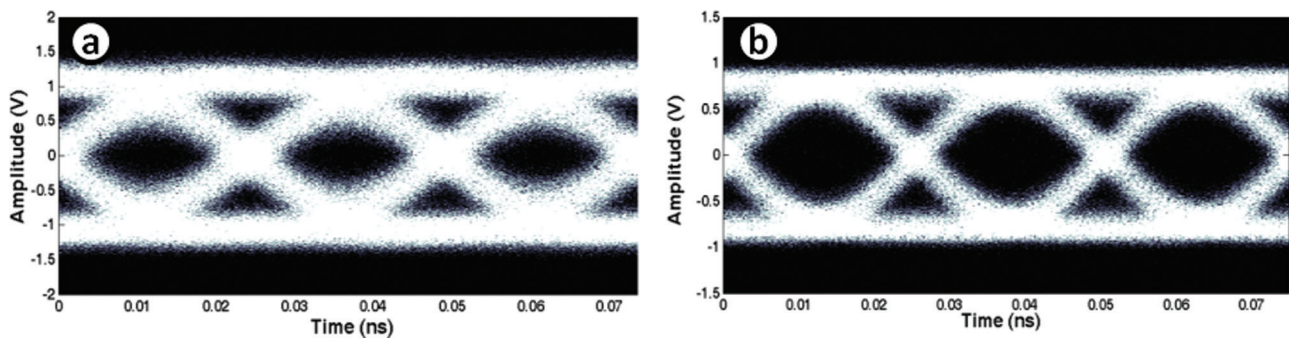


Figure 47 (online color at: www.lpr-journal.org) (a) Eye diagram of 40-Gbps pseudo-random serial data captured using TiSER before equalization; (b) Applying a linear 4-tap feed forward equalizer in digital domain improves the data eye significantly.

As a proof of concept, real-time burst sampling was used to capture 40-Gbps PRBS data signal. This signal was corrupted by inter-symbol interference due to poor frequency response of the coaxial cable used to transmit it. As a result, the data eye captured by the TiSER oscilloscope had poor opening, as seen in Fig. 47(a). Fortunately, since the real-time segments of the signal were available, post processing could be applied to the data. When a linear 4-tap feed forward equalizer was applied, the data eye opening could be significantly improved [109], as illustrated in Fig. 47(b).

10.2.3. Capture of rare events

Ultrafast transient signals appear in numerous contexts in optics and electronics. A particularly interesting variety of ultrafast waveforms are those that represent extreme outliers. These waveforms consist of extreme, rare events that have unusual statistics known as extreme value or heavy-tail distributions. These distributions are outside the realm of the normal distribution (Gaussian statistics) that is followed by most random signals as it is a result of large number of random processes adding together independently.

As an example, recent experiments using the photonic time-stretch technique to study evolution of single shot spectra during supercontinuum generation led to the discovery of optical rogue waves (ORW) - rare and random flashes of highly-coherent white light [110]. This previously unseen phenomenon emerges from the complex interplay of noise with nonlinearities such as self-phase modulation, modulation instability and Raman scattering. Its discovery was made possible by transforming the time scale of the ultra-short laser pulses to match those of the real-time electronic digitizer. By capturing a large data set of millions of single shot events, it became possible to identify very rare but dramatic rogue events with high statistical accuracy.

The TiSER oscilloscope can be useful in capturing rare electronic signal transients in high data rate communications. For example, Fig. 48 shows a hypothetical data stream with rare spikes. Because the data is captured in real time within a segment by TiSER, there is a substantial probability of capturing such rare events, which is not possible with sampling oscilloscopes because of their limited sam-

ple rates. Also, the fast dynamics of such events may not be captured by real-time digitizers because of their limited front-end bandwidths.

The use of a TiSER oscilloscope in capturing rogue waves created through stochastic nonlinear phenomena was demonstrated in [111]. As shown in the experimental setup [Fig. 49(a)], optical rogue waves [110] were generated and added to PRBS electronic data at 12 Gb/s, and the combination modulated onto chirped optical carrier pulses, which are then time-stretched in the dispersive fiber. At the receiver, these stretched waveforms are captured by a 5-GS/s, 4-GHz bandwidth ADC. Without time-stretch, this bandwidth would not have been sufficient to capture the 12 Gbps data. As shown in Fig. 49(b), the TiSER produces a clear eye diagram and also captures the rare transients. One such transient is connected by the bright colored line to highlight it. For comparison, Fig. 49(c) shows the waveform that would be collected by a conventional sampling oscilloscope. Not benefiting from the time-stretch pre-processor, the sampling oscilloscope has an insufficient number of samples to capture the rare event and display the eye diagram properly. The recording time was the same for both measurements (400 μ s).

10.2.4. TiSER oscilloscope prototype

The first prototype of TiSER oscilloscope was released in 2009 to demonstrate its mobility and ease of use for scientists in industry and academia. The TiSER prototype provides a stretch factor of 33 and employs a back-end off-the-shelf digitizer with analog bandwidth of 1.5 GHz, resulting in >40 GHz effective input bandwidth. It is also packaged in the form of a 19-inch rackmount chassis as shown in Fig. 50. The input and output of the TiSER prototype are a high-speed RF signal and a digitized time-stretched signal, respectively.

10.2.5. Other advantages of TiSER oscilloscope

In addition to real-time capability, there are several other advantages of using the TiSER oscilloscope. It is able to

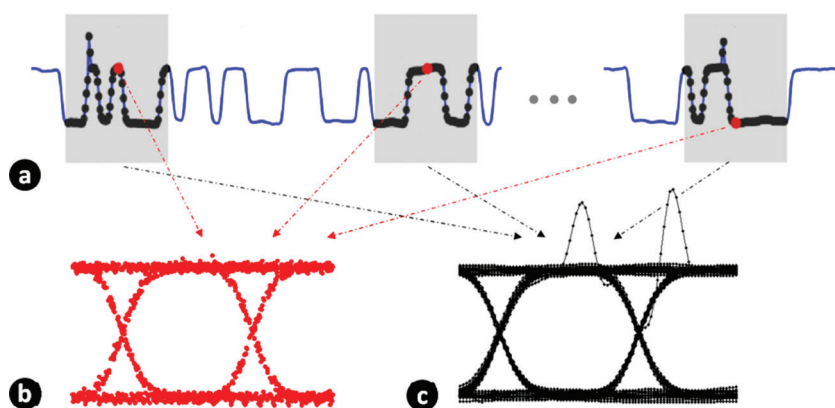


Figure 48 (online color at: www.lpr-journal.org) Comparison between different digitizing mechanisms: (a) Serial digital data waveform (in blue) can be captured by real-time digitizers only if data rates are low. (b) Eye diagram captured by a sampling oscilloscope (c) Eye diagram captured by TiSER oscilloscope, which can potentially capture the rare spikes as well.

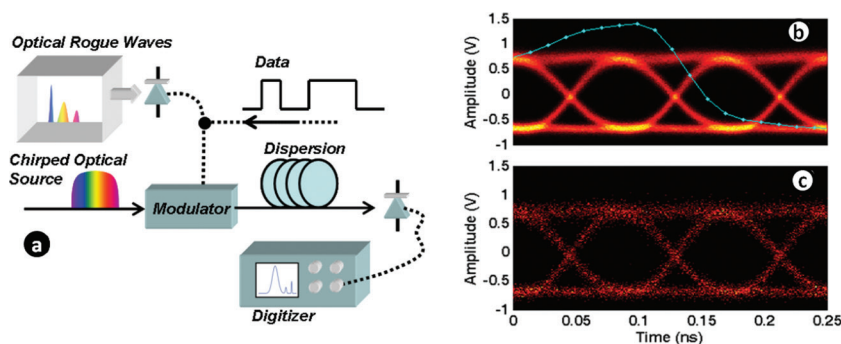


Figure 49 (online color at: www.lpr-journal.org) (a) Experimental setup. (b) PRBS data corrupted by a rogue event as captured by TiSER. The solid line highlights samples of the rogue event that are captured by the TiSER oscilloscope in 400 μ s. (c) Same waveform as captured by a sampling oscilloscope over the 400- μ s interval. © 2009 IEEE. Reprinted, with permission, from [111].

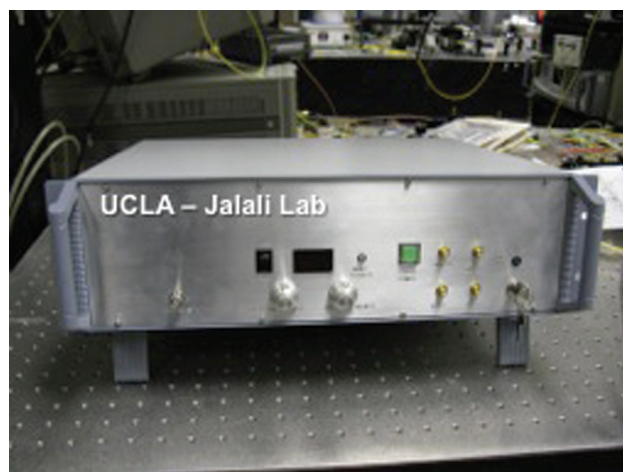


Figure 50 (online color at: www.lpr-journal.org) A prototype of the time-stretch enhanced recording oscilloscope. It is configured to achieve a stretch factor of 33 and an effective input bandwidth of >40 GHz.

achieve very high sensitivity for purely repetitive waveforms by averaging. For example, in automatic test equipment employing TDR, waveform averaging over multiple scans can improve sensitivity significantly, or effectively reduce the test time drastically for a given sensitivity value. When the required sensitivity is not high and reflected pulses have short time apertures, even single-shot TDR measurements can be performed (with proper synchronization), making these measurements extremely fast. From a

device reliability perspective, high voltage spikes can damage the front-ends of conventional sampling oscilloscopes. On the other hand, since the front-end is a Lithium-Niobate modulator in the TiSER oscilloscope, high incident RF power can be tolerated without damaging the front-end.

In conventional digitizers, the noise added due to aperture jitter [6] can become the dominant component of the measured noise or jitter. This noise increases rapidly with the signal frequency and the clock jitter. Fortunately, as described in Section 2, slowing down the signals in time can significantly reduce this effect, making TiSER very useful for jitter sensitive applications.

10.3. Time-stretch oscilloscope for capturing DQPSK signals

The TiSER oscilloscope has demonstrated its capability in the capture of amplitude-modulated signals; however, capture of phase- and amplitude-modulated signals requires simultaneous detection and digitization of in-phase (I) and quadratic-phase (Q) components of the signal in order to enable reconstruction of the original signal in the digital domain. A new architecture with the two-RF-channel and differential detection front-end for capturing optical 100-Gb/s RZ-DQPSK signals was demonstrated in [112]. This system holds promising capability of rapid performance evaluation in high-capacity optical networks employing phase- and amplitude- modulation formats.

This system uses an optical differential detection front-end to demodulate the DQPSK signal into two electrical

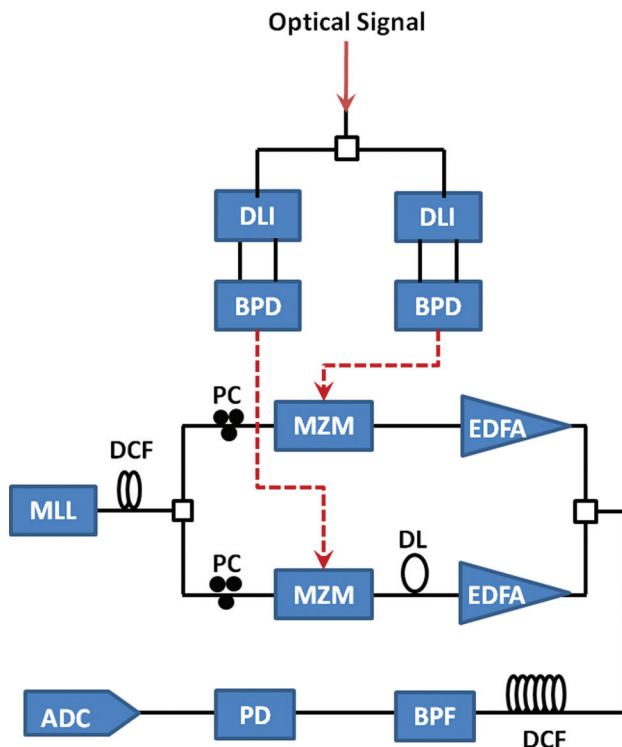


Figure 51 (online color at: www.lpr-journal.org) Detailed schematic of the two-RF-channel time-stretch enhanced recording (TiSER) oscilloscope with differential detection front-end. Solid (black) and dashed (red) lines represent optical fibers and electrical cables, respectively. DLI: Delay line interferometer, BRx: Balanced receiver, MZM: Mach-Zehnder modulator, EDFA: Erbium-doped fiber amplifier, MLL: Mode-locked laser, DL: Delay line, BPF: Bandpass filter, PD: Photo-detector, ADC: Analog-to-digital converter, PC: Polarization controller, DCF: Dispersion compensating fiber.

signals (i.e., denoted by Ch.I and Ch.Q) by means of a pair of one-bit delay-line interferometers and two balanced receivers. Consequently, it performs the RBS on two electrical channels simultaneously. The two-RF-channel TiSER oscilloscope uses only one wavelength-channel to capture both I- and Q- channels. As illustrated in Fig. 51, a train of pre-chirped broadband pulses is equally split into two paths (i.e., two channels) and guided through two high-speed intensity modulators. In order to phase-lock the I- and Q- channels, the signal paths from delay-line interferometers to the intensity modulators are tuned so that the corresponding bits of I- and Q- signals are captured at the same time. The modulated pulse trains are delayed with respect to each other and sent through the second dispersive medium for time-stretching. This configuration provides minimal mismatch between the captured I- and Q- signals [112].

The system used for this demonstration had a time aperture, $T_A = D_I \cdot \Delta\lambda = 400$ ps, where D_I (-20 ps/nm) is the dispersion value of the first dispersive fiber and $\Delta\lambda$ (20 nm) is optical bandwidth. As a result, all captured segments consist of 680 sample points that repeat every ~ 37 MHz (i.e., repetition rate of the mode-locked laser).

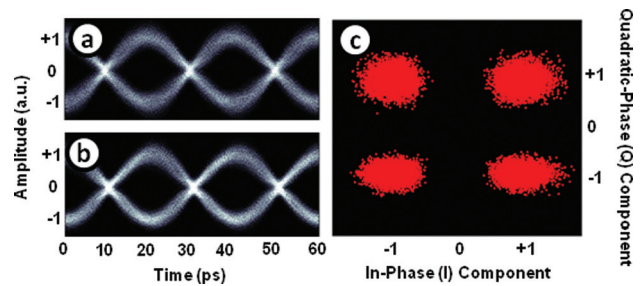


Figure 52 (online color at: www.lpr-journal.org) Eye and constellation diagrams for 100-Gb/s RZ-DQPSK data captured by the two-RF-channel TiSER oscilloscope.

Using these segments, the eye-diagrams of 100-Gb/s data are generated in equivalent time as shown in Fig. 52. Also, since the timings of the pre-chirped pulses and I/Q-data are aligned, the corresponding bits of I- and Q- signals are found to generate the constellation diagrams of the original data (Fig. 52). More importantly, the eye and constellation diagrams shown here are generated from a 400- μ sec time interval of data, which is three to four orders of magnitude shorter than conventional methods for capturing these diagrams.

10.4. Short-time Fourier transform enabled by RBS technique

Short-time Fourier transform (STFT) is a well-known method for time-frequency analysis of non-stationary signals. In an STFT, the signal is segmented by applying a window to it. The width of this window must be short enough such that the signal inside the window is assumed to be stationary. The window size determines the temporal resolution of the time-frequency analysis and establishes how well a non-stationary event can be localized in time. Naturally, a very short window is desired when analyzing highly chirped signals and signals, where a non-stationary event occurs over a short interval. The real-time burst sampling performed by the signal-channel version of time-stretch ADC has enabled a short-time Fourier transform of ultra-fast non-stationary signals [113]. It, hence, overcomes the conventional limitations to frequency-time analysis of signals. As a proof of concept, a time-frequency analysis of a high-speed RF signal (chirp rate of 350 GHz/ns) was demonstrated.

The tenet in the time-stretched short-time Fourier transform (TS-STFT) is that the STFT of a highly chirped ultra-fast signal is performed by reducing its bandwidth to match the ADC's input bandwidth and sampling rate. Figure 53 illustrates this concept using the Gabor sampling lattice of a conventional STFT and TS-STFT analysis. The window size, which is represented by the width of the cell along the time axis, is stretched by a factor S . It should be noted that the area of a single sampling cell is determined by the uncertainty principle and the detectable frequency bandwidth in the Gabor sampling lattice by a factor of S .

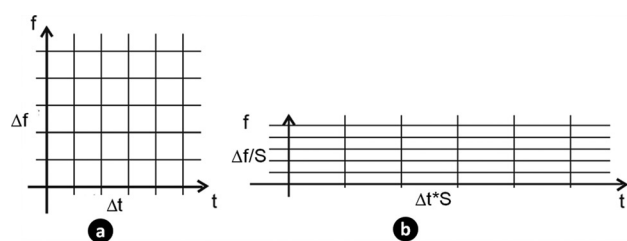


Figure 53 Gabor sampling lattice of (a) STFT and (b) time-stretched short-time Fourier transform (TS-STFT) systems. The area of a single sampling cell in each picture is the same, but the time-stretch increases the detectable frequency bandwidth of the STFT process. S is the stretch factor.

Signal windowing and time-stretching are performed in the optical domain. Sampling, quantization, and STFT are executed in the electrical domain as illustrated in Fig. 54. Sequentially, the non-stationary RF signal is encoded on linearly chirped short optical pulses. This step represents the windowing function in a conventional STFT.

10.5. Amplified Dispersive Fourier Transform for Obtaining Very Large Stretch Ratios

Due to the simplicity and ease of implementation of the photonic time-stretch system, it can easily be used for stretching high-speed electrical signals by large factors that can then be digitized easily by commercially available back-end digitizers. Exploiting this advantage, a record 10-Tera-sample-per-second single-shot real-time digitizer was demonstrated [26]. This system stretched a 95-GHz RF signal by an unprecedented stretch factor of 250 in time.

To achieve this feat, a chain of very long dispersive fibers, corresponding to a total dispersion value of 10-ns/nm, were used in double pass configuration as shown in Fig. 55(a). If standard single-mode fibers (SSMFs) are used to achieve this dispersion value, the amount of loss can exceed 120 dB. Fortunately, dispersion compensating fibers (DCFs) that have much higher dispersion-to-loss ratio are commercially available and can be used to reduce these losses to > 60 dB. Even with these values, the losses were too large for the system to work. To compensate for these losses, one option is to use multiple stages of Erbium

doped fiber amplifiers (EDFAs) to amplify the optical signal. However, the use of EDFAs causes large variations in power levels of the signal across the lengths of the dispersive fibers, as shown in Fig. 55(b). In the locations where power levels are high, optical nonlinearity adds distortion to the signal, and in the regions of low power levels, the SNR gets degraded. At the end of multiple stages, the cumulative effect of these stages can result in a very poor dynamic range.

To overcome this problem, a time-stretch system with distributed Raman amplification [26] is created. This module is used in place of the second dispersive fiber and performs a Fourier transform (frequency-to-time conversion), while boasting internal signal amplification. As a result, the signal power remains relatively stable along the lengths of the fibers, and above the thermal noise of the detector, ensuring a good signal quality at very high real-time sampling rates. In addition to low dispersion-to-loss ratio, the DCF is also favorable because it has a smaller mode area (compared to SSMF), which implies larger Raman gain for the same pump power.

The signal used for the demonstration was a 95-GHz tone generated by a klystron source. The only bandwidth limitation in the system was the bandwidth of the Mach-Zehnder modulator. A 40-GHz dual-output MZM was used which provides the option of phase diversity for overcoming dispersion penalty nulls. Since the MZM frequency response rolls off slowly, the 40-GHz modulator could be overdriven to modulate the chirped carrier with the signal and capture it after stretching. The stretch factor was 250 and the back-end digitizer was a 40-GSa/s oscilloscope, which gave an effective sample rate of 10-Tera-sample-per-second or the sampling resolution of 100 fs, as shown in Fig. 56. The pulse width of the chirped pulses over which the RF signal was modulated was more than 400 ps, giving a record-length-to-resolution ratio of >4000 , compared to a value of 450 demonstrated in [59] for an ultrafast optical “oscilloscope”.

Another demonstration of the front-end bandwidth of the TSADC system was reported by [27]. In this experiment, a 100-GHz Polymer electro-optic Mach-Zehnder modulator by GigOptix Inc [68] was used to capture a 108-GHz sinusoidal signal. This demonstration also shows the use of time-stretch technology as a platform for test and measurement of ultra-high speed optical components, such as optical modulators.

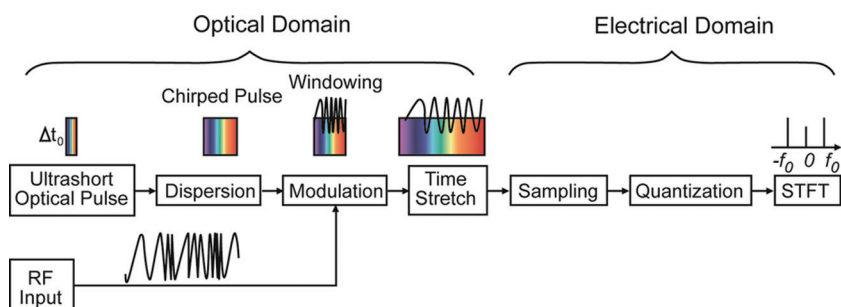


Figure 54 (online color at: www.lpr-journal.org) Block diagram for time-stretched short-time Fourier transform (TS-STFT).

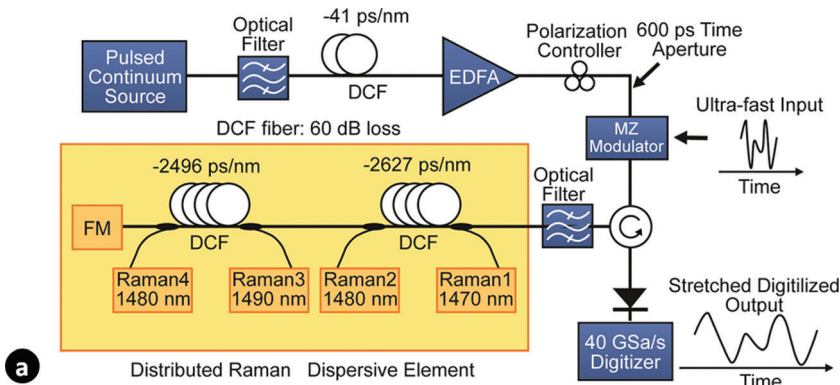


Figure 55 (online color at: www.lpr-journal.org) (a) The experimental setup for the 10-Tera-sample-per-second TSADC. The stretch factor of 250 is achieved using very long dispersive fibers in double-pass configuration and distributed Raman amplification, which turns them into virtually lossless dispersive media. (b) Raman amplification provides distributed gain to compensate optical loss in the fibers. If doped fiber amplifiers are used instead, optical nonlinearity and noise can severely degrade the TSADC dynamic range.

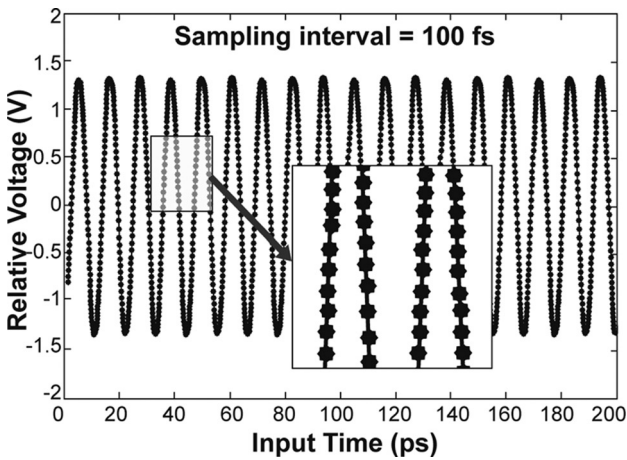
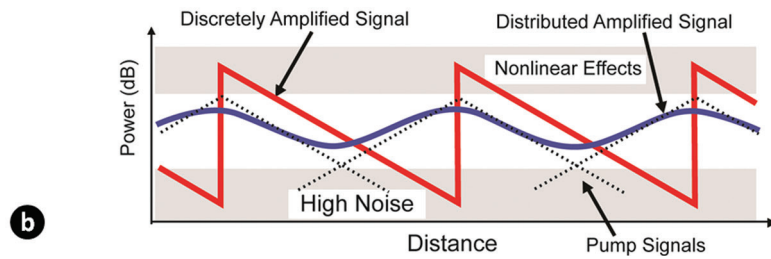


Figure 56 A 95-GHz tone stretched by a factor of 250 using the photonic time-stretch system and captured by a 40-GSa/s digitizer, resulting in the real-time single-shot measurement of the signal at a *record* 10-Tera-samples-per-second.

11. Continuous-time TSADC demonstration

The TSADC has been shown to be very useful when operating in the real-time burst sampling (RBS) mode (described in section 10) for different types of wideband high-resolution diagnostic applications. However, this mode of operation cannot be used when the information carried in the entire signal is required to be captured. For example, characterization of a 100-Gbit/s optical link can be performed using real-time burst sampling, but in order to decode the data without loss of any information, a continuous-time realization of the TSADC is needed. Implementation of a fully continuous TSADC involves the combination

of multiple segments of the signal from different channels without incurring any significant noise or distortion penalty. The following section describes different factors important for achieving continuous operation, and also discusses the experimental demonstrations.

11.1. Continuous time operation

To achieve continuous operation, the signal has to be continuously modulated over the chirped optical carrier before time-stretching. To ensure this, the ultra-short optical pulses from the broadband pulsed source must be stretched to a point that there is no temporal gap between adjacent pulses, as shown in Fig. 57(a)–(b). Further stretching results in overlap between signals from adjacent pulses [Fig. 57(c)]. To avoid this problem, in addition to stretching, the optical signal has to be segmented into multiple channels so that each stretched segment can be captured by a separate back-end digitizer, without any crosstalk between adjacent pulses. The obvious method for accomplishing this involves use of some form of time gating (see Fig. 58).

Fortuitously, this time gating can easily be accomplished in the TSADC without the use of any type of active switches. By virtue of wavelength-to-time mapping, the wavelength bands of the chirped pulses are mapped to time. As a result, when these pulses are filtered using WDM filters, they are effectively gated in time, as illustrated in Fig. 58. This operation is termed as virtual time gating [114], and was used for demonstrating the first continuous-time TSADC (albeit with a small stretch factor of 1.5).

In addition to time gating, a number of other considerations become important for achieving continuous-time operation in the TSADC. To ensure that the signal is captured

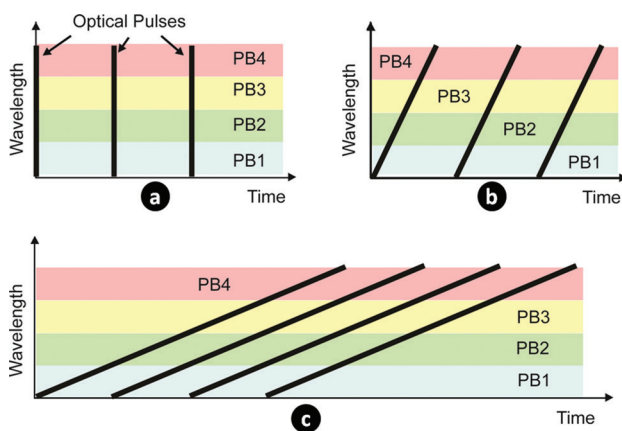


Figure 57 (online color at: www.lpr-journal.org) (a) Initial ultra-short pulses in the TSADC spanning the four wavelength passbands (PB). (b) First dispersion causes wavelength-to-time mapping in the pulses, such that adjacent pulses are temporally connected. (c) Further stretching after RF modulation causes them to overlap in time, unless time gating is applied to separate them. © 2005 IEEE. Reprinted, with permission, from [114].

continuously (without any gaps in time), adjacent channels must have a small overlap in the modulated optical spectrum. This can be guaranteed by the non-ideal nature of the filters, due to which a small portion of the spectrum in the chirped pulses is shared between adjacent channels, as shown in Fig. 59 (ref. [61]). Additionally, to ensure that the signal segments from successive pulses in a passband channel do not run into each other and cause crosstalk after stretching (because of slow roll-off and non-ideal nature of the optical filters), the stretch factor must be slightly smaller than the number of channels.

Mismatches among different channel segments become crucial and can drastically reduce the dynamic range in the continuous-time TSADC (compared to the single channel case). Different forms of mismatches include gain, DC offset, stretch factor non-uniformity, and timing mis-

matches (as illustrated in Fig. 60). These mismatches have similar effects as the mismatches in time-interleaved electronic ADCs, and lead to addition of spurious tones in the spectrum of the RF signal.

The effects of these mismatches can be removed using suitable correction and calibration techniques. DC offset and gain mismatch effects can be removed easily by adding different DC and gain components in different channel segments digitally. Timing offsets and stretch factor non-uniformities all act as temporal distortions. These temporal distortions can be removed by the technique described in Section 6. Furthermore, other effects such as nonlinear distortion caused by channel (or wavelength) dependent bias offset in the Mach-Zehnder modulator can also be removed jointly for all channels using the correction technique described in Section 6.

11.2. Continuous-time TSADC demonstrations

Using virtual time gating and applying temporal overlaps, recently a record 150-GSamples/s TSADC was demonstrated [61]. It achieved a stretch factor of 3 and used four 50-GS/s back-end digitizers available in the Tektronix DSA72004 oscilloscope to achieve this sampling rate.

To improve the resolution in such a system, the small temporal distortion for combined channel segments that can add severe spurious distortion tones in the captured signal, must be corrected. To further improve the resolution and bandwidth, differential or phase diverse operation will be required. With the differential operation and time warp correction, a 10-GHz bandwidth TSADC with 7.2-ENOB resolution was demonstrated [9]. Even though this demonstration did not show fully continuous operation, demonstration of channel-to-channel stitching for adjacent channels and the combination of 30 segments synchronously with high fidelity shows that this technique can lead to a continuous-time TSADC with high resolution and high bandwidth.

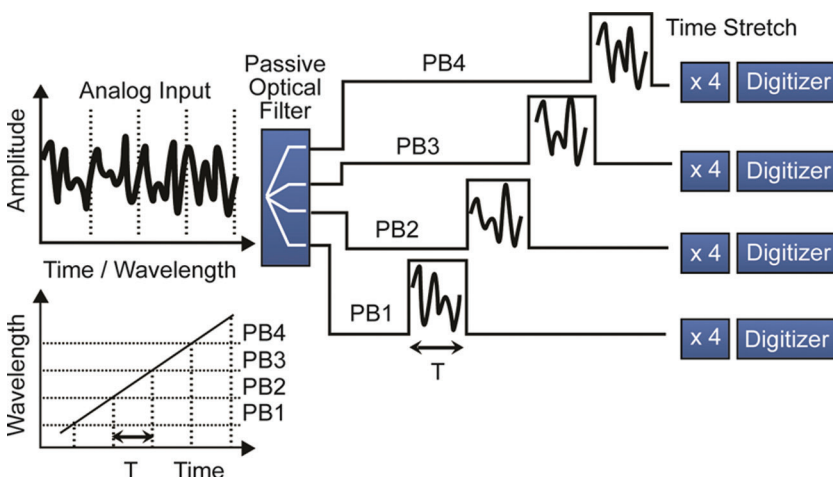


Figure 58 (online color at: www.lpr-journal.org) Virtual time gating principle for achieving continuous-time TSADC. In a real implementation, passive optical filtering is applied after dispersion, so that only one dispersive device is required for stretching all the channels.

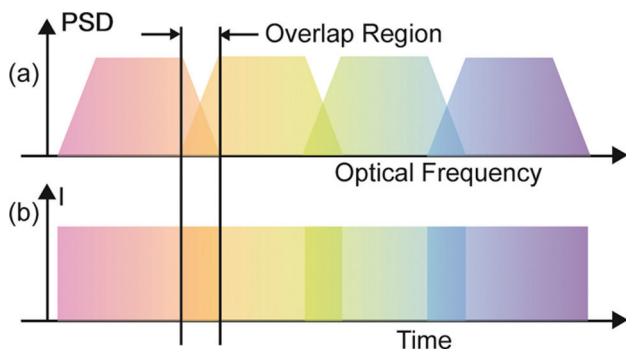


Figure 59 (online color at: www.lpr-journal.org) Optical channel alignment in frequency and time domains. (a) Adjacent channels slightly overlap in frequency to ensure continuous capture of the RF signal. (b) By virtue of wavelength-time mapping, the overlap is also maintained in the time domain [61]. PSD: Power spectral density; I: Intensity. © 2008 IEEE. Reprinted, with permission, from [61].

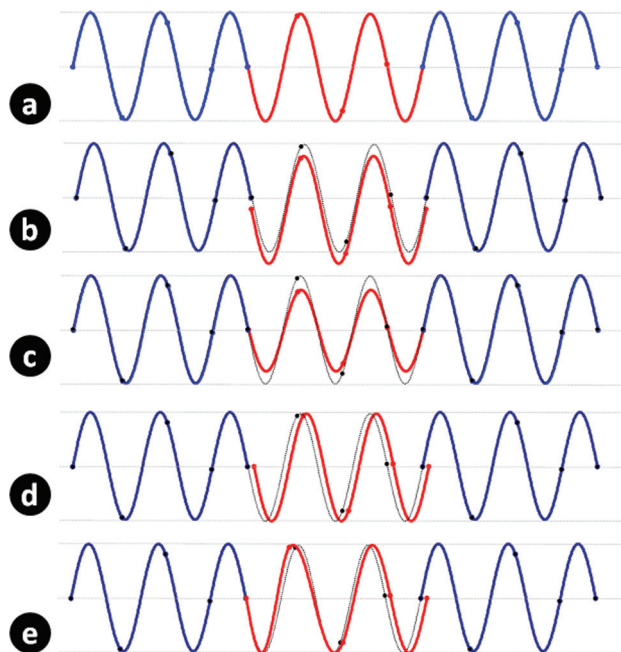


Figure 60 (online color at: www.lpr-journal.org) Non-idealities in stretched signal segments obtained from the time-stretch pre-processor. (a) Ideal waveforms; (b) Middle segment has an additional DC offset; (c) Middle segment has gain mismatch with respect to other segments; (d) Middle segment has a timing offset; (e) Middle segment has a stretch factor mismatch and non-uniformity (time warp distortion).

12. All-optical time-stretch pre-processor for real-time capture of optical signals

As it is described earlier in this manuscript, similar to conventional analog optical links, single-sideband modulation [62] or phase diversity technique [63] eliminates any fundamental bandwidth limitation in the TSADC. However, in practice the maximum bandwidth is limited to that of the

Mach-Zehnder modulator. While such a bandwidth is more than sufficient for digitizing electronic signals and having an electrical input to the system is ideal, it would be desirable to have an all-optical modulator when the input signal to be digitized is optical.

In this section, we describe an all-optical time-stretch digitizer [115], which directly captures optical signals eliminating the bandwidth limitation imposed by E/O and O/E conversions. This approach maps the signal under test onto a chirped optical carrier using four-wave mixing (FWM) process in a highly nonlinear fiber. Over the last decades, the FWM process has formed the basis for a class of versatile parametric devices enabling amplification and regeneration [30, 116–118], frequency conversion [118, 119], phase conjugation [120–122], and optical sampling [123]. Our all-optical time-stretch digitizer exploits ultrafast FWM process between a pulsed pump and a signal to encode wideband optical signals onto the spectrum of a pre-chirped broadband optical carrier. It then stretches the wideband optical signal in time before detection, so that the signal can be recorded using a low-bandwidth photo-detector and electronic analog-to-digital converter. Another technique that achieves real-time full-field measurement of ultrafast optical waveforms was demonstrated by Fontaine et al. [124]. This method is able to measure the amplitude and phase of an optical signal by performing parallel coherent detection on spectral slices.

12.1. Operation principle and demonstration

To replace the electro-optic modulation with all-optical modulation in the input stage of the TSADC, a broadband optical pulse source is employed as the “pump” for FWM in an optical fiber. The ultrafast optical data (signal to be digitized) then represents the “signal” in the FWM process. The pump is pre-chirped to map wavelengths into time (i.e., wavelength-to-time mapping). This can be realized by using a mode-locked laser followed by a dispersive medium such as dispersion compensating fiber. The all-optical time-stretch technique also employs a medium with a large nonlinear index such as highly nonlinear fiber (HNLF) to perform mixing. The HNLF is a particularly well-suited medium for this purpose, since it offers low-loss propagation and precise dispersion tailoring. From the spectral-domain point-of-view, the signal mixes with the pre-chirped broadband pump, generating a broadband chirped idler that contains information of the signal [Fig. 61(a)].

From the time-domain point-of-view, at each time instant, a wavelength of the pre-chirped broadband pump mixes with the signal, creating a modulated idler that is chirped [Fig. 61(b)]. The dispersion profile of the nonlinear medium is engineered such that the zero-dispersion wavelength (ZDW) lies near the pump wavelengths, and is fairly flat within the signal and pump bands. This ensures maximal phase matching, and nearly no walk-off, while mixing occurs. In other words, one-to-one mapping of the signal waveform onto the wavelength of the pre-chirped pump is

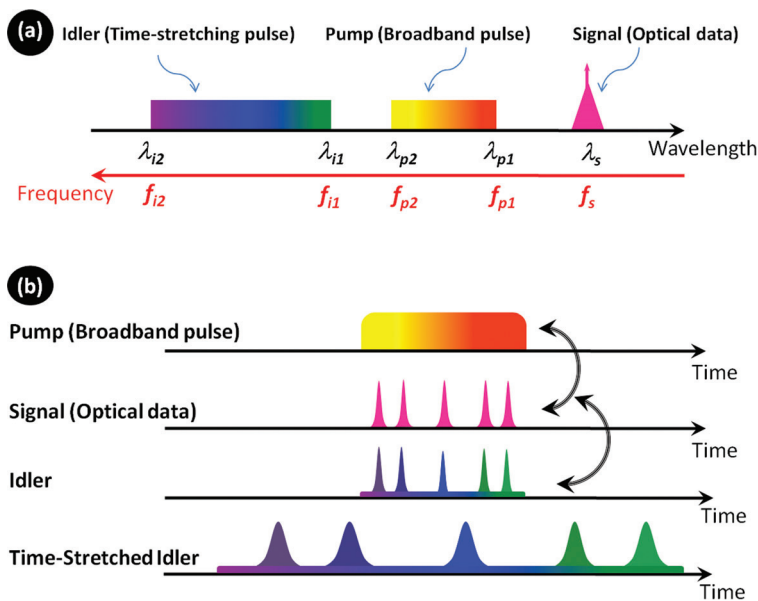


Figure 61 (online color at: www.lpr-journal.org) (a) Spectral-domain representation. The ultrafast optical data signal (f_s) mixes with the broadband pulsed pump ($\Delta f_p = f_{p1} - f_{p2}$) via the four-wave mixing (FWM) process. (b) Time-domain representation. At each time instant along the signal, a wavelength of the pre-chirped broadband pump mixes with the signal at that time instant; creating a chirped modulated idler. The idler is then time-stretched to reduce the analog bandwidth of the optical data signal. Reprinted with permission from [115]. Copyright 2012, American Institute of Physics.

achieved. The modulated chirped idler is then extracted and time-stretched using another dispersive medium, e.g., dispersion compensating fiber. A photo-detector converts this time-stretched optical signal to the electrical domain and the resultant signal is hence a stretched replica of the original optical data signal with much reduced analog bandwidth. An electronic analog-to-digital converter that would normally be too slow can now be used to digitize the electrical signal.

In case of the degenerate FWM process employed here, the idler frequency (f_i) can be expressed in terms of pump (f_p) and signal (f_s) wavelengths, $f_i = 2f_p - f_s$. Assuming that the signal's optical bandwidth is negligible compared with the pump and idler bandwidths, the idler bandwidth can be written as, $\Delta f_i = 2\Delta f_p$, where Δf_p is the pump bandwidth.

As evident from Fig. 61, the idler bandwidth (Δf_i) is at least twice as large as the pump bandwidth (Δf_p). The effect has been also reported by Inoue and Toba [119] that a frequency displacement of the mixing signals leads to twice the frequency shift of the mixing product. In a photonic time-stretch pre-processor, the time-stretch factor (the amount by which the signal is stretched) is determined by

$$S = 1 + \frac{D_2 \cdot \Delta \lambda_2}{D_1 \cdot \Delta \lambda_1}, \quad (12.1)$$

where D_1 and D_2 are the dispersion values of the first and second dispersive medium, while $\Delta \lambda_1$ and $\Delta \lambda_2$ are the optical bandwidths before and after modulation. In the case of conventional TSADC, equation (12.1) simplifies to $S = 1 + D_2/D_1$, since the optical bandwidths before and after modulation are constant. However, in the case of an all-optical time-stretch pre-processor, $\Delta \lambda_1$ and $\Delta \lambda_2$ are not the same, and are proportional to Δf_p and Δf_i , respectively. This implies that the stretch factor (S) is increased (by a fac-

tor of >2) compared with conventional TSADC. As will be discussed later in this section, the increase in optical bandwidth also appears to be useful in improving the bandwidth limitation due to the dispersion penalty.

To demonstrate the performance of the all-optical time-stretch digitizer, capture of 40-Gb/s optical data signal is performed. An experimental apparatus as described in Ref. [115] employing a mode-locked laser centered at 1565 nm with ~ 7 -nm bandwidth was used as the pump. The first and second dispersive fibers was chosen to be -41 ps/nm and -1105 ps/nm, providing an stretch factor of ~ 54 . Real-time segments of the optical data signal spanning 8–10 sequential bits are captured every ~ 27 ns (repetition rate of the mode-locked laser is ~ 37 MHz) at an effective sampling rate of 1.25 TS/s as shown in Fig. 62(a). Using these segments, the original signal was reconstructed in equivalent-time mode [Fig. 62(b)].

12.2. Dispersion penalty and its mitigation via single-sideband modulation conversion

As described earlier, in the conventional TSADC, when double-sideband modulation (DSB) is used to modulate RF signals onto the optical pre-chirped carrier, a frequency-fading phenomenon due to dispersion occurs. A similar phenomenon is observed in the all-optical time-stretch pre-processor as shown in Fig. 63(a). Since the optical data signal is a double-sideband modulated signal, the resultant idler is also double-sideband modulated. Therefore, the idler sidebands undergo different linear and nonlinear phase shifts, resulting in a power penalty at the photo-detector. Fortunately, the increase in optical bandwidth through the FWM process effectively manifests itself as a reduction in the initial dispersion (by a factor of >2). Therefore, the

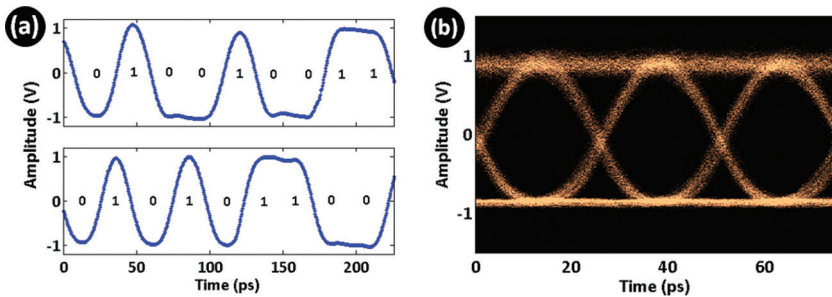


Figure 62 (online color at: www.lpr-journal.org) 40-Gb/s non-return-to-zero (NRZ) on-off-keying (OOK) data. (a) Two real-time segments of 40-Gb/s data captured at an effective sampling rate of 1.25 TS/s. (b) Eye-diagram of 40-Gb/s constructed from real-time segments in equivalent-time mode. Reprinted with permission from [115]. Copyright 2012, American Institute of Physics.

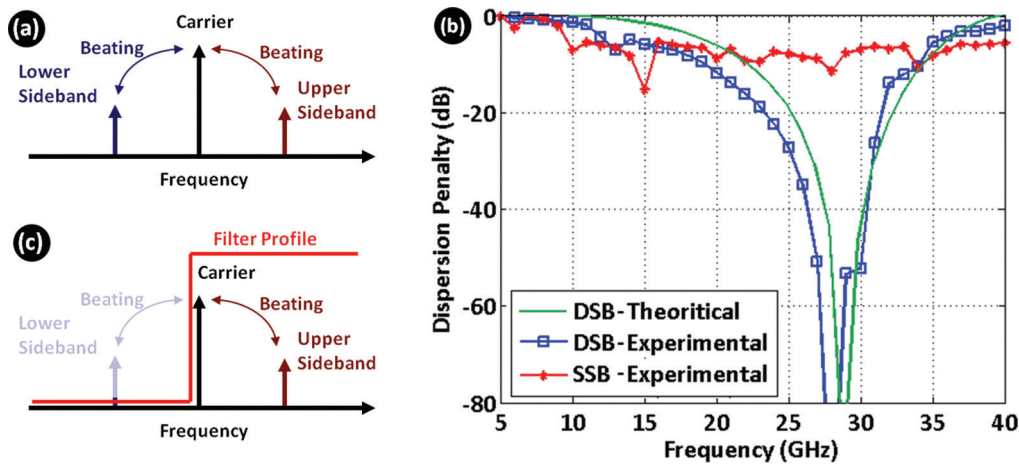


Figure 63 (online color at: www.lpr-journal.org) (a) If the optical data signal is double-sideband modulated, the sidebands beat with carrier and result in interference at the photo-detector. (b) Dispersion penalty in an all-optical time-stretch digitizer with an initial dispersion of -150 ps/nm. Note that the initial dispersion is intentionally increased to shift the bandwidth roll-off into the measurable range of our equipment. When double-sideband (DSB) modulation is used, the measured penalty (blue curve) is in good agreement with theoretical prediction (green solid curve). By employing the single-sideband technique, the dispersion penalty is completely mitigated (red curve). (c) Single-sideband modulation is implemented by suppressing one of the sidebands of the optical data signal. An optical bandpass filter can be used for this purpose. Reprinted with permission from [115]. Copyright 2012, American Institute of Physics.

3-dB bandwidth due to dispersion penalty is at least twice as large as the conventional TSADC.

In order to characterize the dispersion penalty, a modulated CW laser with an RF signal sweeping from 5 GHz to 45 GHz was used. Figure 63(b) shows the measured dispersion penalty (blue curve) and theoretical calculation (green solid curve) for an all-optical time-stretch pre-processor with initial dispersion of -150 ps/nm. This measurement is in good agreement with the theoretical calculation shown in the same plot (green curve). Note that the theoretical calculation does not consider nonlinear phase shift as explained in ref. [76]. The slight mismatch between the theoretical prediction and measurement comes from the fact that nonlinear phase shift in the fibers shifts the null frequency of the dispersion penalty curve toward lower frequencies as evident from Fig. 63(b).

In the context of TSADC, single-sideband modulation [62] has been successful in eliminating the bandwidth limitation due to dispersion penalty. Our all-optical time-stretch pre-processor behaves in the same way. Hence, this technique was adapted to the all-optical time-stretch system by converting the optical data modulation format from double-

sideband modulation (DSB) to single-sideband modulation (SSB) before the four-wave mixing process. This can be performed by using an optical bandpass filter to suppress one of the optical sidebands as illustrated in Fig. 63(c). In order to demonstrate mitigation of dispersion penalty using SSB modulation conversion, a programmable optical processor (Finisar, WaveShaper 1000) was used to implement a desired filter profile. An optical signal transmitter with an RF synthesizer sweeping from 5 GHz to 45 GHz was also used. Figure 63(b) shows the measured dispersion penalty curve (red curve) for an all-optical time-stretch pre-processor with initial dispersion of -150 ps/nm when SSB modulation was performed. The result shows the complete mitigation of the dispersion penalty null frequency by converting the optical data signal to SSB format.

13. Spin-off applications of photonic time-stretch

In addition to wideband analog-to-digital conversion, photonic time-stretch (PTS) is also an enabling technology for

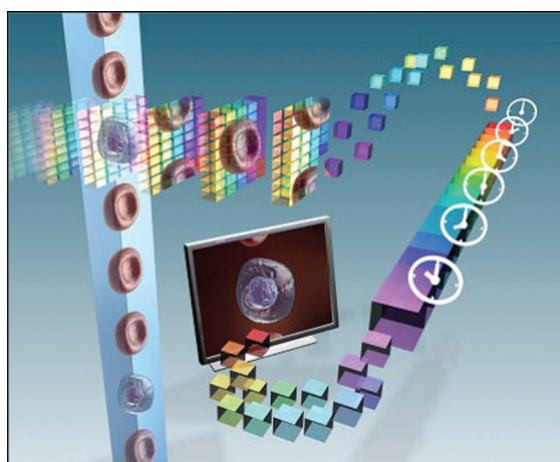


Figure 64 (online color at: www.lpr-journal.org) Schematic of serial time-encoded amplified microscopy (STEAM) also known as time-stretch imager.

high-throughput real-time instrumentation such as imaging and spectroscopy. Serial time-encoded amplified microscopy, or stretched time-encoded amplified microscopy (STEAM) [125], makes use of the amplified dispersive Fourier transform to acquire, simultaneously slow down and amplify (in the optical domain) images using a single-pixel photo-detector and a commercial digitizer. It also features real-time image processing currently operating at 37 million line scan frames-per-second [126, 127]. STEAM maps a multi-dimensional image into a 1D serial time-domain optical waveform that is stretched in time, optically amplified, and converted to an electronic waveform, and then captured with a real-time digitizer (Fig. 64). This is performed by first encoding the spatial coordinates of the object onto the spectrum of a broadband pulse with a 1D (line scan) or 2D rainbow created by a spatial disperser. A key feature of STEAM is optical image amplification, which allows its operation at shutter speeds of tens of picoseconds and frame rates of tens of millions of frames per second and with very low illumination power (only a few mW).

The time-stretch camera has been used to create a high-throughput flow-through imaging system for real-time detection of rare cells [126]. The so-called STEAM flow cytometer integrates (i) a high-speed bright-field imager based on a STEAM camera which features time stretching and image amplification and holds the world record in frame rate, shutter speed, and sensitivity, (ii) a microfluidic chip that employs a combination of hydrodynamic and inertial focusing for precise positioning of cells in high-speed flow, and (iii) a real-time digital image processor based on a high-speed field-programmable gate array (FPGA) that performs real-time screening of a large heterogeneous population of cells for detection of rare target cells. The system performs real-time image-based screening of a large volume of blood with a record high throughput of 100,000 cells/s. It has shown detection of breast cancer cells in blood with a false positive rate of 10^{-6} – 100x better than the state-of-the-art flow cytometers. This technology can significantly reduce

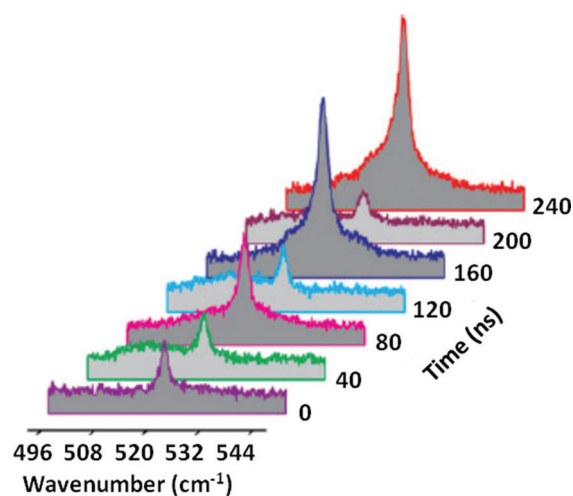


Figure 65 (online color at: www.lpr-journal.org) A time-varying stimulated Raman signal from a silicon sample, measured in a real-time continuous measurement. Every 40 ns, a new spectral snapshot was acquired (frame rate of 25 MHz) [52].

errors and costs in medical diagnosis. Proof-of-concept experiments were performed using blood spiked with MCF7 breast cancer cells derived from cell lines and involved acquisition and real-time processing of 100 million image frames at a line scan rate of 37 million frames per second. The next stage in this research is clinical testing to measure the efficacy of this new instrument in analyzing patient blood with unknown composition, and also the addition of fluorescent capability to the system.

Wavelength-time spectroscopy [52], which also relies on the photonic time-stretch technique, permits real-time single-shot measurements of rapidly evolving or fluctuating spectra. The technique, which is referred to as chirped wavelength encoding and electronic time-domain sampling (CWEETS), transforms the temporal envelope of a signal into its spectrum using group-velocity dispersion (GVD) to chirp the signal. Once the temporal profile is mapped into its spectral shape, the spectrum can be acquired directly in the time domain using a single detector and a real-time oscilloscope. Using this technique, the temporal evolution of a dynamic process (i.e., stimulated Raman spectra in Silicon) has been measured as shown in Fig. 65. In the demonstration, the dead time between Raman snapshots is about 40 ns. This capability could be used, for example, to monitor a biochemical process with a continuous single-shot measurement or to conduct high-speed Raman microscopy.

Spontaneous emergence of complex patterns is a hallmark of so-called nonlinear systems and appears in disparate systems from fingerprints to cloud formations and heart rhythms to optical waves. Randomly-driven complex dynamics underlie the counterintuitive development of these ordered arrangements. A quintessential form of such pattern formation is known as modulation instability: the spontaneous growth of temporal or spatial oscillations that are nearly absent initially. The high-throughput

single-shot time-stretch spectrometer has been used to discover spontaneously-evolved emergent behavior in modulation instability, a hallmark of nonlinear systems that leads to diverse phenomena such as the formation of wave-like patterns in sand, cloud formation, heart rhythms, and in optical rogue waves [128]. The real-time spectrometer captured spontaneous growth of spectral patterns in ultra-short laser pulses propagating through glass fiber. It was discovered that, in contrast to the standard notion of a modulation instability gain spectrum consisting of smooth “rabbit-ear” lobes extending on both sides of the pump wavelength, on a single shot time scale the spectrum consists of a random collection of narrow lines that compete for the pump energy. Millions of single-shot spectra were captured showing a ‘winner takes all’ behavior [128]. This phenomenon was unseen in previous studies of modulation instability because individual patterns cannot readily be discerned at these high speeds with conventional measurement techniques.

The applications of the time-stretch Fourier transform have been generally restricted to the telecommunication (1550nm wavelength) band due to the lack of low loss dispersive elements at other wavelengths, in particular the biologically important wavelength of 800nm (low water absorption). The chromo modal dispersion device (CMD) [31] is a dispersive device that exploits wavelength selective excitation of a multi-mode waveguide to convert the very large modal dispersion in multimode waveguides into much more valuable chromatic (group velocity) dispersion. It has a very flexible operating wavelength spectrum, thus it extends the application of time-stretch (dispersive) Fourier transform to wavelength outside the telecommunication band. Its utility in performing real-time single-shot spectroscopy in the 800nm band at the ultra-high frame (refresh) rate of 90.8 MHz is shown in Fig. 66.

Finally, the photonic time-stretch was used to enable high-throughput optical coherence tomography (OCT) that offers 1,000 times higher axial scan rate than conventional OCT in the 800 nm spectral range. A record axial scan rate of 90.8 MHz was demonstrated [129]. This is made possible by employing photonic time-stretch for chirping a pulse train and transforming it into a passive swept source.

14. Conclusions

The photonic time-stretch technique has been found to be very useful for overcoming the speed limitation of electronics and creating high-speed analog-to-digital converters. This technique uses amplified dispersive Fourier transform to slow down the analog signal in time and hence to compress its bandwidth. It was also shown that photonic time-stretch can be useful not only in improving the bandwidth and resolution of high-speed ADCs, but also in reducing power consumption in future high-speed ADCs significantly.

The present article discussed novel techniques and architectures employing this photonic-assisted technique that

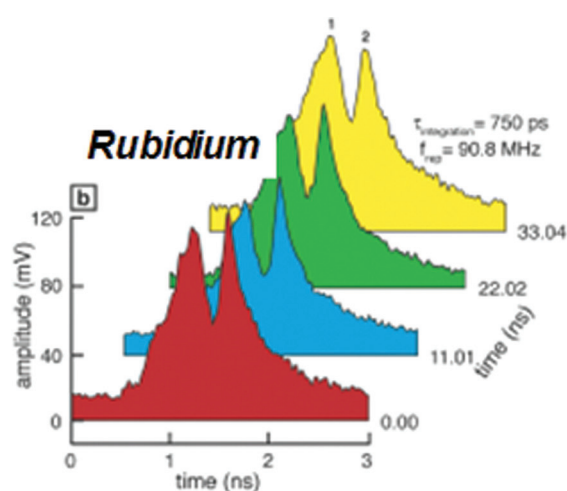


Figure 66 (online color at: www.lpr-journal.org) A single-shot atomic absorption spectroscopy of Rubidium vapor enabled by time-stretch (Dispersive) Fourier transform via chromo modal dispersion (CMD). Sequence of four consecutive single-shot time-domain traces captured by a photodiode and oscilloscope at a repetition rate of 90.8 MHz [31].

address the demands on resolution, bandwidth, and spectral efficiency. Important results and achievement in A/D conversion was also highlighted. Moreover, we presented a summary of time-stretch technology’s extension to high-throughput single-shot spectroscopy, a technique that led to the discovery of optical rogue waves. Finally its application in high-throughput imaging, which has recently led to identification of rogue cancer cells in blood with record sensitivity, was discussed.

Acknowledgements. The authors would like to acknowledge the support by US Defense Advanced Research Projects Agency (DARPA) and National Science Foundation (NSF) through CIAN-ERC.

Received: 31 March 2012, **Revised:** 15 October 2012,

Accepted: 16 October 2012

Published online: 11 January 2013

Key words: Photonic analog-to-digital conversion, time stretch, optical communications, optical links, real-time spectroscopy, optical sampling, optical kerr nonlinearity, high-throughput imaging.



Ali M. Fard is currently a research fellow at the Harvard Medical School and Massachusetts General Hospital. He received his MSc and PhD degrees in Electrical Engineering from University of California Los Angeles in 2009 and 2011, respectively. Dr. Fard is the recipient of several awards including 2011–2012 Electrical Engineering Outstanding PhD Award, 2011 SPIE Scholarship in Optics

and Photonics and 2011 L.M.K. Boelter award (From Dimitris N. Chorafas Foundation). He is a member of the Optical Society (OSA), The International Society for Optical Engineering (SPIE), and Institute of Electrical and Electronics Engineers (IEEE). He was also the founding president of UCLA OSA Student Chapter, and the founding vice-president of SPIE Student Chapter at UCLA.



Shalabh Gupta is an Assistant Professor of Electrical Engineering at Indian Institute of Technology Bombay, Mumbai, India, where he joined in September 2009. He received B.Tech degree from Indian Institute of Technology, Kanpur, India in 2001, and M.S. and Ph.D. degrees from University of California, Los Angeles in 2004 and 2009, respectively,

all in Electrical Engineering. Between years 2003 to 2006, Dr. Gupta worked at Chrontel Inc., San Jose, CA, and Skyworks Solutions Inc., Irvine, CA, where he primarily designed analog and RF integrated circuits for high-speed serial links and GSM/EDGE transceivers. He also spent summers of 2008 and 2009 at NEC Labs, Princeton, NJ, working on technologies for 100G coherent transmission systems. His current research interests include design of high-speed analog/RF integrated circuits, coherent optical transmission systems, photonic analog-to-digital conversion and linearization techniques for power amplifiers & RF photonic links.



Bahram Jalali is the Northrop-Grumman Optoelectronics Chair Professor of Electrical Engineering at UCLA with joint appointments in the California NanoSystems Institute (CNSI) and the UCLA School of Medicine. He received his Ph.D. in Applied Physics at Columbia University in 1989 and was with Bell Laboratories in Murray Hill, New Jersey until 2002

before coming to UCLA. Dr. Jalali is a Fellow of the Optical Society of America (OSA), Institute of Electrical and Electronics Engineers (IEEE), and the American Physical Society (APS). He is the recipient of the R.W. Wood Prize from Optical Society of America for the invention and demonstration of the first Silicon Laser. In 2005 he was elected into the Scientific American Top 50, and received the BrideGate 20 Award in 2001 for his entrepreneurial accomplishments.

References

- [1] J. Sinsky and P. Winzer, *IEEE Microw. Mag.* **10**(2), 44 (2009).
- [2] P. J. Winzer and R. J. Essiambre, *P. IEEE* **94**(5), 952 (2006).
- [3] J. Wang, S. Nuccio, H. Huang, X. Wang, J.-Y. Yang, and A. Willner, *Opt. Express* **18**, 23740 (2010).
- [4] J. Murphy, 19th Annual Gallium Arsenide Integrated Circuit (GaAs IC) Symposium, (Technical Digest, 1997), pp. 83–86.
- [5] A. Yen, *Flow Cytometry: Advanced research and clinical applications*, (CRC press, 1989).
- [6] R. H. Walden, *IEEE J. Sel. Area. Comm.* **17**(4), 539 (1999).
- [7] R. H. Walden, *IEEE Compound Semiconductor Integrated Circuits Symposium*, pp. 1–2 (2008).
- [8] I. Dedic, *Conference on Optical Fiber Communication (OFC)*, pp. 1–3 (2010).
- [9] S. Gupta and B. Jalali, *Opt. Lett.* **33**(22), 2674 (2008).
- [10] J. Kim, M. J. Park, M. H. Perrott, and F. X. Kärtner, *Opt. Express* **16**(21), 16509 (2008).
- [11] W. W. Ng, L. Luh, D. L. Persechini, D. Le, Y. M. So, M. Mokhtari, C. H. Fields, D. Yap, J. E. Jensen, *Proc. SPIE* **5435**, 171 (2004).
- [12] G. C. Valley, *Opt. Express* **15**(5), 1955 (2007).
- [13] B. Shoop, *Photonic analog-to-digital conversion*, (Springer Verlag, 2001).
- [14] L. Y. Nathawad, R. Urata, B. A. Wooley, and D. A. B. Miller, *IEEE J. Solid-St. Circ.* **38**(12), 2021 (2003).
- [15] P. W. Juodawlkis, J. C. Twichell, G. E. Betts, J. J. Hargreaves, R. D. Younger, J. L. Wasserman, F. J. O'Donnell, K. G. Ray, R. C. Williamson, *IEEE T. Microw. Theory* **49**(10), 1840 (2001).
- [16] F. Coppinger, A. S. Bhushan, and B. Jalali, *Electron. Lett.* **36**(4), 316 (2000).
- [17] A. S. Bhushan, F. Coppinger, S. Yegnanarayanan, and B. Jalali, *Opt. Lett.* **24**(11), 738 (1999).
- [18] J. U. Kang, and R. D. Esman, *Electron. Lett.* **35**(1), 60 (1999).
- [19] L. Pierno, M. Dispenza, G. Tonelli, A. Bogoni, P. Ghelfi, and L. Poti, *International Topical Meeting on Microwave Photonics*, p. 236 (2008).
- [20] O. Boyraz, J. Kim, M. N. Islam, E. Coppinger, and B. Jalali, *J. Lightwave Technol.* **18**(12), 2167 (2000).
- [21] J. M. Dudley, G. Genty, and S. Coen, *Rev. Mod. Phys.* **78**(4), 1135 (2006).
- [22] A. S. Bhushan, F. Coppinger, and B. Jalali, *Electron. Lett.* **34**(11), 1081 (1998).
- [23] F. Coppinger, A. S. Bhushan, and B. Jalali, *IEEE T. Microw. Theory* **47**(7), 1309 (1999).
- [24] B. Jalali, and F. M. A. Coppinger, *US Patent no. 6, 288, 659* (2001).
- [25] Y. Han and B. Jalali, *J. Lightwave Technol.* **21**(12), 3085 (2003).
- [26] J. Chou, O. Boyraz, D. Solli, and B. Jalali, *Appl. Phys. Lett.* **91**(16), 161105 (2007).
- [27] J. Mallari, C. Wei, D. Jin, G. Yu, A. Barklund, E. Miller, P. O'Mathuna, R. Dinu, A. Motafakker-Fard, and B. Jalali, *Optical Fiber Communication Conference (OFC)*, p. OThU2 (2010).
- [28] A. S. Bhushan, F. Coppinger, and B. Jalali, *Electron. Lett.* **34**(9), 839 (2002).
- [29] J. Capmany, and D. Novak, *Nat. Photonics* **1**(6), 319 (2007).
- [30] G. P. Agrawal, *Nonlinear Fiber Optics*. (Burlington, MA, Academic Press, 2007).

- [31] E. D. Diebold, N. K. Hon, Z. Tan, J. Chou, T. Sienicki, C. Wang, and B. Jalali, *Opt. Express* **19**(24), 23809 (2012).
- [32] W. J. Caputi, *IEEE T. Aero. Elec. Sys.* **2**, 269 (1971).
- [33] G. P. Agrawal, *Fiber-optic communication systems* (New York: John Wiley & Sons, Inc., 1992).
- [34] H. Friis, *Proc. IRE* **32**, 419 (1944).
- [35] Y. Han, and B. Jalali, *Proc. Conference on Lasers and Electro-Optics*, p. 2 (2003).
- [36] S. Gupta, G. C. Valley, and B. Jalali, *J. Lightwave Technol.* **25**(12), 3716 (2007).
- [37] A. Joshi, D. Becker, C. Wree, and D. Mohr, *Proc. SPIE* **6243**(1), 62430E (2006).
- [38] K. Poulton, R. Neff, B. Setterberg, B. Wuppermann, T. Kopley, R. Jewett, J. Pernillo, C. Tan, and A. Montijo, *IEEE International Solid-State Circuits Conference* **1**, 318 (2003).
- [39] E. Bartolome, V. Mishra, G. Dutta, and D. Smith, *TI Analog Applications Journal*.
- [40] J. Chen, J. W. Sickler, E. P. Ippen, and F. X. Kärtner, *Opt. Lett.* **32**(11), 1566 (2007).
- [41] J. Kim, J. Chen, J. Cox, and F. X. Kärtner, *Opt. Lett.* **32**(24), 3519 (2007).
- [42] J. C. Candy, *An Overview and Basic Concepts in Delta-Sigma Data Converters, Theory, Design, and Simulation*, S. Norsworthy, R. Schreier, and G. Temes, Eds. (IEEE Press, 1992).
- [43] F. Coppinger, V. Magoon, A. S. Bhushan, and B. Jalali, *SPIE Conference Series* **3795**, 18 (1999).
- [44] J. Stigwall, and S. Galt, *J. Lightwave Technol.* **25**(10), 3017 (2007).
- [45] A. Fard, S. Gupta, and B. Jalali, *Opt. Lett.* **36**(7), 1077 (2011).
- [46] S. Dubovitsky, W. H. Steier, S. Yegnanarayanan, and B. Jalali, *J. Lightwave Technol.* **20**(5), 886 (2002).
- [47] J. Basak, and B. Jalali, *Optical Fiber Communication Conference (OFC)*, 2005.
- [48] R. Sadhwani, and B. Jalali, *J. Lightwave Technol.* **21** (12), 3180 (2003).
- [49] O. V. Sinkin, R. Holzlohner, J. Zweck, and C. R. Menyuk, *J. Lightwave Technol.* **21**(1), 61 (2003).
- [50] A. Fard, B. Buckley, and B. Jalali, *IEEE Photonics Technol. Lett.* **23**(14), 947 (2011).
- [51] P. V. Kelkar, F. Coppinger, A. S. Bhushan, and B. Jalali, *Electron. Lett.* **35**(19), 1661 (1999).
- [52] D. R. Solli, J. Chou, and B. Jalali, *Nat. Photonics* **2**(1), 48 (2008).
- [53] K. Goda, and B. Jalali, *Physical Review A*, **82**(3), 33827 (2010).
- [54] K. Goda, D. R. Solli, K. K. Tsia, and B. Jalali, *Phys. Rev. A* **80**(4), 43821 (2009).
- [55] D. H. Chang, H. Erlig, M. C. Oh, C. Zhang, W. H. Steier, L. R. Dalton, and H. R. Fetterman, *IEEE Photonic. Tech. L.* **12**(5), 537 (2000).
- [56] D. Chen, H. R. Fetterman, A. Chen, W. H. Steier, L. R. Dalton, W. Wang, and Y. Shi, *Appl. Phys. Lett.* **70**(25), 3335 (1997).
- [57] B. H. Kolner, and M. Nazarathy, *Opt. Lett.* **14**(12), 630 (1989).
- [58] C. V. Bennett, and B. H. Kolner, *Opt. Lett.* **24**(11), 783 (1999).
- [59] M. A. Foster, R. Salem, D. F. Geraghty, A. C. Turner-Foster, M. Lipson, and A. L. Gaeta, *Nature* **456**(7218), 81 (2008).
- [60] J. W. Goodman, *Introduction to Fourier optics*, (Roberts & Company Publishers, 2005).
- [61] J. Chou, J. Conway, G. Seffler, G. Valley, and B. Jalali, *International Topical Meeting on Microwave Photonics*, pp. 35–38 (2008).
- [62] J. M. Fuster, D. Novak, A. Nirmalathas, and J. Marti, *Electron. Lett.* **37**(1), 67 (2001).
- [63] Y. Han, O. Boyraz, and B. Jalali, *IEEE T. Microw. Theory* **53**(4), 1404 (2005).
- [64] A. Tarighat, S. Gupta, A. H. Sayed, and B. Jalali, *J. Lightwave Technol.* **25**(6), 1580 (2007).
- [65] S. Gupta, B. Jalali, J. Stigwall, and S. Gait, *IEEE International Topical Meeting on Microwave Photonics*, pp. 141–144 (2007).
- [66] J. Han, B. Seo, Y. Han, B. Jalali, and H. R. Fetterman, *J. Lightwave Technol.* **21**(6), 1504 (2003).
- [67] J. Chou, T. Rose, J. Conway, G. C. Valley, and B. Jalali, *Opt. Lett.* **34**(7), 869 (2009).
- [68] “GigOptix, Inc.,” www.gigoptix.com.
- [69] S. Gupta, and B. Jalali, *IEEE Avionics, Fiber-Optics and Photonics Technology Conference*, pp. 3–4 (2009).
- [70] W. E. Vander Velde, *Multiple-input describing functions and nonlinear system design*, (New York, McGraw-Hill, 1968).
- [71] J. J. Busgang, L. Ehrman, and J. W. Graham, *P. IEEE* **62**(8), 1088 (1974).
- [72] W. J. Rugh, *Nonlinear system theory*, (Citeseer, 1981).
- [73] W. I. Way, *Broadband hybrid fiber/coax access system technologies*, (Academic Press, 1999).
- [74] A. H. Gnauck, S. K. Korotky, J. J. Veselka, J. Nagel, C. T. Kemmerer, W. J. Minford, and D. T. Moser, *IEEE Photonic. Tech. L.* **3**(10), 916 (1991).
- [75] J. C. Twichell, and R. Helkey, *IEEE Photonic. Tech. L.* **12**(9), 1237 (2000).
- [76] A. M. Fard, P. T. S. DeVore, D. R. Solli, and B. Jalali, *J. Lightwave Technol.* **29**(13), 2025 (2011).
- [77] M. J. Potasek, G. P. Agrawal, and S. C. Pinault, *J. Opt. Soc. Am. B* **3**(2), 205 (1986).
- [78] D. Anderson, *Phys. Rev. A* **27**(6), 3135 (1983).
- [79] G. A. Seffler, J. Chou, J. A. Conway, and G. C. Valley, *J. Lightwave Technol.* **28**(10), 1468 (2010).
- [80] G. Lenz, B. J. Eggleton, C. R. Giles, C. K. Madsen, and R. E. Slusher, *IEEE J. Quantum Elect.* **34**(8), 1390 (1998).
- [81] S. Gupta, and B. Jalali, *IEEE Proceedings of Microwave Photonics*, 2008.
- [82] W. Ng, T. Rockwood, G. A. Seffler, and G. C. Valley, *IEEE Photonics Technol. Lett.* **24**(14), 1185 (2012).
- [83] C. M. Gee, G. A. Seffler, P. T. S. DeVore, and G. C. Valley, in *Signal Processing in Photonic Communications conference*, (2012).
- [84] D. A. Muller, *Nat. Materials* **4**(9), 645 (2005).
- [85] A. J. Annema, *IEEE T. Circuits-II* **46**(6), 711 (1999).
- [86] B. Murmann, *IEEE Custom Integrated Circuits Conference*, pp. 105–112, (2008).
- [87] P. B. Kenington, and L. Astier, *IEEE T. Veh. Technol.* **49**(2), 643 (2000).

- [88] T. B. Cho, D. W. Cline, C. S. G. Conroy, and P. R. Gray, *IEEE Symposium Low Power Electronics*, pp. 70–73 (1994).
- [89] K. Poulton, R. Neff, B. Setterberg, B. Wuppermann, and T. Kopley, *Analog circuit design: high-speed AD converters, automotive electronics, and ultra-low power wireless*, p. 17 (2006).
- [90] S. Kawahito, *IEEE Custom Integrated Circuits Conference*, pp. 505–512 (2006).
- [91] M. Horowitz, T. Indermaur, and R. Gonzalez, *IEEE Symposium Low Power Electronics*, pp. 8–11 (1994).
- [92] A. Allan, D. Edenfeld, W. Joyner, A. Kahng, M. Rodgers, and Y. Zorian, *Computer* **35**(1), 42 (2002).
- [93] K. C. Dyer, D. Fu, S. H. Lewis, and P. J. Hurst, *IEEE J. Solid-St. Circ.* **33**(12), 1912 (1998).
- [94] S. Gupta, M. Choi, M. Inerfield, and J. Wang, *Proc. IEEE ISSCC (Digest Technical Papers, 2006)*, p. 576.
- [95] “Tektronix product information,” http://www.tek.com/products/oscilloscopes/selection_chart.html. [Online]. Available: http://www.tek.com/products/oscilloscopes/selection_chart.html.
- [96] “LeCroy product information,” <http://www.lecroy.com/tm/products/default.asp>.
- [97] “Ofs dispersion compensation fiber product datasheet,” <http://www.specialtyphotonics.com/pdf/products/specialty/dispersion/hfdkc.pdf>
- [98] J. Lin, “Efficient high power ns pulsed fiber laser for lidar and laser communications,” *MRS Bulletin*, Vol. **5**, 2005.
- [99] S. Gupta, G. C. Valley, R. H. Walden, and B. Jalali, *IEEE Proceedings of Avionics, Fiber Optics, and Photonics*, 2009.
- [100] F. Ouellette, J. F. Cliche, and S. Gagnon, *J. Lightwave Technol.* **12**(10), 1728 (1994).
- [101] J. A. Conway, G. A. Seffler, J. T. Chou, and G. C. Valley, *Opt. Lett.* **33**(10), 1108 (2008).
- [102] G. C. Valley, and G. A. Seffler, *submitted*, 2012.
- [103] L. E. Nelson, and R. M. Jopson, *Journal of Optical and Fiber Communications Research* **1**(4), 312 (2004).
- [104] A. Mireshghi, *The PHOBIAC simulator: An operational manual*, (UCLA, 2009).
- [105] “Simulink software,” <http://www.mathworks.com/products/simulink/>
- [106] S. D. Corey, and A. T. Yang, *IEEE T. Microw. Theory* **43**(9), 2151 (1995).
- [107] S. Gupta, and B. Jalali, *Appl. Phys. Lett.* **94**(4), 41105 (2009).
- [108] J. Patrin, and M. Li, *Proc. DesignCon* (2002).
- [109] A. Motafakker-Fard, S. Gupta, and B. Jalali, *Optical Fiber Communication Conference (OFC)*, p. OTuN3 (2010).
- [110] D. R. Solli, C. Ropers, P. Koonath, and B. Jalali, *Nature* **450**(7172), 1054 (2007).
- [111] S. Gupta, D. R. Solli, A. Motafakker-Fard, and B. Jalali, *CLEO/Europe and EQEC (Conference Digest, 2009)*, p. CF6_1.
- [112] A. Fard, J.-Y. Yang, B. Buckley, J. Wang, M. R. Chitgarha, L. Zhang, A. E. Willner, and B. Jalali, *Opt. Lett.* **36**(19), 3804 (2011).
- [113] A. Nuruzzaman, O. Boyraz, and B. Jalali, *Proc. of the 21st IEEE Instrumentation and Measurement Technology Conference (IMTC)* **1**, pp. 31–34 (2004).
- [114] Y. Han and B. Jalali, *IEEE T. Circuits-I* **52**(8), 1502 (2005).
- [115] A. M. Fard, B. Buckley, S. Zlatanovic, C.-S. Brès, S. Radic, and B. Jalali, *Appl. Phys. Lett.* **101**(5), 051113 (2012).
- [116] C. J. McKinstrie, S. Radic, and A. R. Chraplyvy, *IEEE J. Sel. Top. Quant.* **8**(3), 538 (2002).
- [117] S. Radic, *Laser Photonics Rev.* **2**(6), 498 (2008).
- [118] R. Stolen and J. Bjorkholm, *IEEE J. Quantum Elect.* **18**(7), 1062 (1982).
- [119] K. Inoue, and H. Toba, *IEEE Photonics Technol. Lett.* **4**(1), 69 (1992).
- [120] C. J. McKinstrie, S. Radic, and A. H. Gnauck, *Optics and Photonics News* **18**(3), 34 (2007).
- [121] A. Yariv, and D. M. Pepper, *Opt. Lett.* **1**(1), 16 (1977).
- [122] M. E. Marhic, *Fiber optical parametric amplifiers, oscillators and related devices*, (Cambridge university press, 2007).
- [123] M. Sköld, M. Westlund, H. Sunnerud, and P. A. Andrekson, *J. Lightwave Technol.* **27**(16), 3662 (2009).
- [124] N. K. Fontaine, R. P. Scott, L. Zhou, F. M. Soares, J. P. Heritage, and S. J. B. Yoo, *Nat. Photonics* **4**(4), 248 (2010).
- [125] K. Goda, K. K. Tsia, and B. Jalali, *Nature* **458**(7242), 1145 (2009).
- [126] K. Goda, A. Ayazi, D. R. Gossett, J. Sadasivam, C. K. Lonappan, E. Sollier, A. M. Fard, S. C. Hur, J. Adam, C. Murray, C. Wang, N. Brackbill, D. Di Carlo, and B. Jalali, *Proc. Nat. Acad. Sci.* **109**, 11630 (2012).
- [127] A. Fard, A. Mahjoubfar, K. Goda, D.R. Gossett, D. Di Carlo, and B. Jalali, *Biomed. Opt. Express* **2**(12), 3387 (2011).
- [128] D. R. Solli, G. Herink, B. Jalali, and C. Ropers, *Nat. Photonics* **6**, 463 (2012).
- [129] K. Goda, A. Fard, O. Malik, G. Fu, A. Quach, and B. Jalali, *Opt. Express* **20**(18), 19612 (2012).